EINDHOVEN UNIVERSITY OF TECHNOLOGY

Department of Applied Physics and Science Education

Creating a laboratory setup for analogue gravity experiments using surface gravity waves in flowing water

by

J. Fransen

MSC THESIS

Assessment committee

Member 1 (chair):	prof.dr. F. Toschi
Member 2:	dr. A. Fuster
Member 3:	dr. M. Duran-Matute

Graduation

Program:	Applied Physics
Capacity group:	Fluids and Flows
Supervisor:	prof.dr. F. Toschi
Date of defence:	July 4, 2024
Student ID:	1224963
Study load (ECTS):	60
Track:	Fluids, Bio and Soft Matter

Abstract

Analogue gravity is a recent field of research that seeks to replicate and study general relativistic phenomena in laboratory experiments. Analogue gravity leverages the mathematical similarities between the equations governing different physical systems and those describing spacetime and gravity. In the case of surface gravity waves in water, the evolution of the water waves can be written in the form of a curved spacetime Klein-Gordon equation, from which an effective metric tensor for the water waves can be obtained. The physical analogy allows for experiments on physics in the proximity of black holes.

In this project, a laboratory setup is created in which water surface gravity waves can be generated that propagate through a channel with space-varying flow speed and water height, while multiple cameras record the air-water interface. The laboratory setup and measurement methods are validated using theoretical predictions from the Saint-Venant equations and the dispersion relation for water waves, which is additionally found in the random fluctuations present in the setup.

Lastly, the focus is shifted to the study of analogue white hole horizons, created by a region of increased flow speed, which forms an impenetrable barrier for waves that propagate against the flow direction. More specifically, the measurement of analogue Hawking radiation generated by sending waves towards this white hole horizon.

Contents

1 Introduction

In Einstein's geometric theory of gravity, also known as general relativity, gravity is understood not to be a force, but rather the result of the shape of space and time, which together form spacetime. Masses present bend this spacetime, causing otherwise straight paths to become curves, which we perceive as gravity. General relativity not only explains the movement of planets and stars, but also leads to bizarre phenomena like black holes and the expanding universe. Black holes are regions of space with intense curvature from which nothing can escape, bounded by an event horizon.

In modern physics, two collections of theories describe part of nature very well, namely, general relativity, which describes the large (astronomical) scales, and quantum mechanics, which describes the small scales (elementary particles, subatomic physics). If both theories were universally true, they should be compatible. A situation where both theories (the one of the small and the one of the large) meet is in the proximity of black holes. In 1974, Hawking [1] suggested that black holes actually emit radiation, in a process which contains elements of general relativity and quantum physics. Black holes can therefore serve as a testbed for understanding and testing the compatibility between both theories.

Numerous theories can be devised about the physics surrounding black holes, but ultimately, measurements are the definitive test. Even with enormous progress in observational methods, measuring the physics near a black hole is extremely challenging. The anticipated Hawking radiation from black holes is very faint, and producing a black hole in a laboratory is well beyond our capabilities. Thus, we turn to analogies.

Physical analogies, using another (sometimes better understood or more easily accesible) system with comparable behaviour, can be enormously helpful research tools. Not only can it help with understanding and gaining intuition of the unknown system, it could also offer the possibility to use already developed tools and methods on new problems. In some cases, the usage of a physical analogy allows for experiments where they otherwise would not be possible. However, one must keep in mind that an analogy, however helpful, will never be a perfect equivalent to the original system under study. Different analogies will capture different features more or less accurately.

In 1981, Unruh [2] established a relation between the mathematical description of the propagation of scalar fields in curved spacetimes and the propagation of sound waves in flowing water. This work was later extended to an analogy with surface gravity waves in water, propagating in an open-channel flow with a variable depth. [3] It is this analogy, of surface gravity waves in flowing water, for which a laboratory setup is created in this project. The waves' behaviour is influenced by the flow speed and depth of the water, analogous to how spacetime curvature affects light and matter in general relativity.

The water surface wave analogy is particularly effective in the laboratory, where the speed of the waves can be adjusted by varying the depth of the water, and the analogue curvature of spacetime follows from the background flow, making it possible to simulate different gravitational scenarios, including event horizons.

In practice, creating an analogue event horizon using water waves involves setting up a background water flow that mimics the conditions near such a horizon. For example, a submerged obstacle in a water channel can create a gradient in the flow speed, generating a horizon where the flow speed matches the propagation speed of the waves. In such a setup, water waves cannot pass through this horizon, similar to how light cannot escape from a black hole. Both black and white hole horizons can be created, and both the interior and exterior regions around the horizons can be studied.

The goal of this work is to construct a laboratory setup in which surface gravity waves propagating in an open channel form a physical analogy to scalar field propagation in curved spacetime. The objective is to analyse the relevant fluid dynamics and experimental methods used to create the physical analogy

in order to comprehend, in detail, the processes and the reasons for its success or failure. A trial application for the setup is the reproduction of time-reverse analogue Hawking radiation, which has been reported by Weinfurtner et al. [4] in a wave flume experiment.

The report is organised as follows. In Section 2, the theory behind the water wave analogy is discussed, together with fluid mechanics of open channel flows and waves, with a special focus on wave propagation in a background flow. In Section 3, the constructed experimental setup is presented, together with the data processing steps used. In Section 4, various measurements are showcased to validate the experimental setup, verify theoretical predictions, characterise wave generation behaviour, and attempt to detect analogue Hawking radiation. In Section 5, the findings are summarised, followed by a future outlook of the project in Section 6.

2 Theoretical background

The subsequent sections treat the theoretical aspects of the project. Beginning with a brief description of Hawking radiation, followed by the theory behind analogue gravity with surface gravity waves in water. After that, the fluid mechanics in wave flume flow are discussed, and finally, the physics of surface gravity waves is treated, with a focus on waves propagating in flowing water, the conversion of small wavenumber waves into large wavenumber waves, and the connection to Hawking radiation.

2.1 Hawking radiation

Hawking radiation is a theoretical prediction by Stephen Hawking that black holes can emit radiation due to quantum effects near the event horizon. [1, 5] In quantum field theory, the vacuum is not empty but is filled with virtual particle-antiparticle pairs that constantly form and annihilate. Near the event horizon, one of these virtual particles can fall into the black hole while the other escapes into space.

The derivation of the radiation from the horizon presented by Hawking depends on arbitrarily high frequencies of the field, depending on unknown physics. [6, 7] This is referred to as the trans-Planckian problem. The physical analogy of surface waves offers a natural high-frequency cut-off since very high-frequency waves in water are dissipated. If the Hawking process can be observed in the analogy, it indicates that the dependence on these high frequencies is not necessary.

In Rousseaux et al. [8], Hawking radiation is described as arising from the mixing of positive and negative frequency waves near the event horizon; see Fig. 1. A wave packet escaping from the horizon can be traced backwards in time, revealing that it originates from two distinct waves: one with positive frequency and the other with negative frequency. The time reverse of this process is an incoming wave to a white hole horizon, which is converted into this pre-cursor wave-pair. It is the latter process which is aimed to be simulated in the water wave analogy.

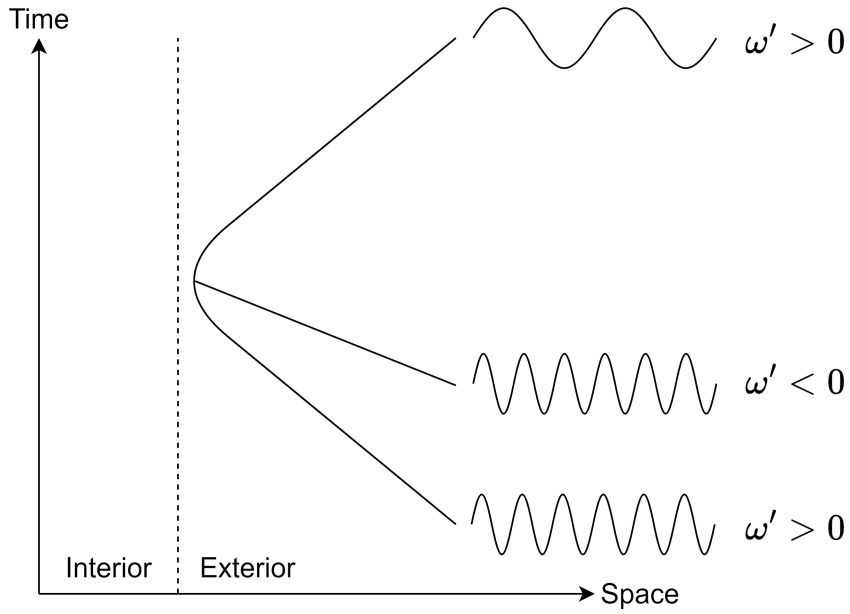

Figure 1: Schematic representation of Hawking radiation as described in Ref. [8]. A wave escaping into space (top) originates from two very large frequency waves with opposite signs. The exact trajectories of these waves depend on the properties of the spacetime medium.

2.2 Surface gravity wave analogy

In the Introduction, the possibility of connecting light propagation in curved spacetime and surface gravity waves in a water flow is stated, and in this section, the connection is made quantitative. In essence, curved spacetime is represented by a space-varying flow on which the propagating scalar fields are represented by propagating surface gravity waves.

Fig. 2 shows a diagram of such an analogue model. The figure shows a water channel where a raised bottom causes an increase in flow speed. A wave created in a region where the water speed is lower than the wave propagation speed may travel in both directions, but a wave created in a region where the water speed is larger than the wave propagation speed (over the raised bottom), the waves may only travel in the downstream direction. At points where the speed of the flowing water equals the propagation speed of the waves, we can speak of an analogue (event) horizon. The diagram, therefore, contains two analogue horizons, indicated by vertical dotted lines.

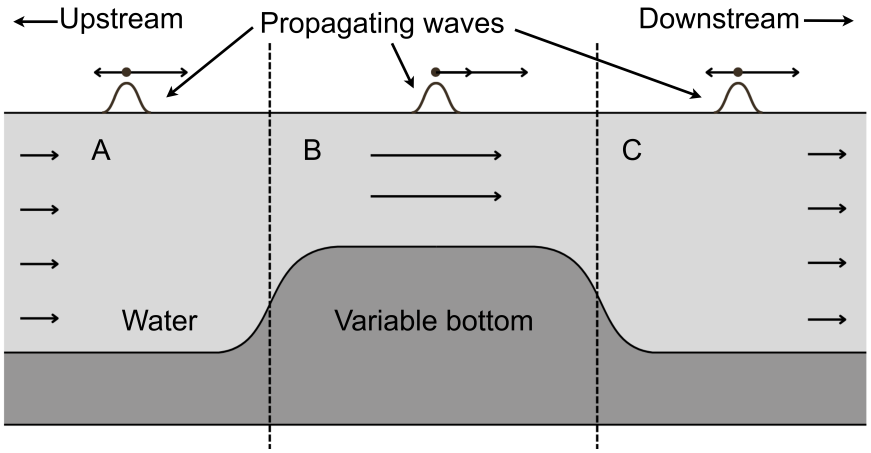

Figure 2: Schematic representation of black hole and white hole horizons in an open channel. The raised bottom leads to a region of increased flow speed (region B), where the flow speed of the water exceeds the propagation speed of the waves, resulting in a region where the waves can only propagate downstream. Encountered from region A, the obstacle forms an analogue black hole spacetime since there is a point-of-no-return, which is the analogue event horizon. Encountered from region C, the waves encounter an impassable flow region, which is the analogue white hole spacetime.

The left horizon, as approached from the left, is a black hole horizon, since waves created at this horizon can only travel to the right, into the effective black hole interior. The right horizon, as approached from the right, models a white hole horizon since it forms an uncrossable boundary. The region in between the horizons forms a white or black hole interior, depending on the direction of approach.

In addition to this intuitive model, there is a mathematical framework for the physical analogy, derived by Ralf Schützhold and William G. Unruh [3]. The propagation of a scalar wave in a general spacetime is given by the generalised scalar wave equation (massless Klein-Gordon),

$$\Box f = \frac{1}{\sqrt{-g}} \partial_\mu \left(\sqrt{-g} g^{\mu\nu} \partial_\nu f \right) = 0 \,, \tag{1}$$

where $g_{\mu\nu}$ is the metric tensor, which is the object that defines the geometry of the spacetime (and thus the gravity and its effects) and $g = \det(g_{\mu\nu})$ is the determinant of the metric tensor.

The evolution of surface gravity waves in an open channel can be written as a similar wave equation,

from which an effective metric can be deduced. The interpretation of the effective metric goes as follows: the water waves propagate through the channel as if they are a scalar field propagating through curved spacetime with this metric tensor.

The derivation of the effective metric for a general bottom in the context of gravity wave analogues of black holes involves several steps; the most important of which are reported here. The starting point, as in most fluid dynamics research, are the Navier-Stokes equations, a set of equations that contain mass and momentum conservation. For an incompressible, inviscid medium of constant density, the governing equations are

$$\boldsymbol{\nabla} \cdot \mathbf{v} = 0\,, \tag{2}$$

$$\frac{D\mathbf{v}}{Dt} = \frac{\partial \mathbf{v}}{\partial t} + (\mathbf{v} \cdot \boldsymbol{\nabla})\mathbf{v} = -\frac{1}{\rho}\boldsymbol{\nabla} p + \mathbf{g} + \frac{1}{\rho}\mathbf{f}\,, \tag{3}$$

where $\mathbf{v}$ is the velocity field, ρ the density, p the pressure, the gravity is $\mathbf{g} = -g\mathbf{e}_z$ (pointing vertically downwards) and an external force $\mathbf{f} = -\rho\boldsymbol{\nabla}_\parallel V^\parallel$ that establishes a steady horizontal flow $V^\parallel$, $\boldsymbol{\nabla}_\parallel$ denotes the gradient in horizontal directions. If the flow is also irrotational ($\boldsymbol{\nabla} \times \mathbf{v} = 0$), the velocity field may be described using a velocity potential: $\mathbf{v} = \boldsymbol{\nabla}\phi$, with which Eqs. (2) and (3) can be rewritten into

$$\frac{\partial \phi}{\partial t} + \frac{1}{2}(\boldsymbol{\nabla}\phi)^2 = -\frac{p}{\rho} - gz - V^\parallel\,. \tag{4}$$

The surface waves are modelled as perturbations $\delta\phi$ to a steady, background flow $\mathbf{v}_B$ with height h_B. The potential perturbations correspond to surface height perturbations δh. Under the assumption that the height perturbations are small compared to the water height ($\delta h \ll h_B$) and that the wavelength of the waves is larger than the water height ($h_B \ll \lambda$), and retaining only first-order perturbations, the waves on a moving background medium v_B on top of a flat bottom are given by the wave equation

$$\left(\frac{\partial}{\partial t} + \mathbf{v}_B^\parallel \cdot \nabla_\parallel\right)^2 \delta\phi - g h_B \nabla_\parallel^2 \delta\phi = 0\,, \tag{5}$$

which, compared to the generalized wave equation for curved spacetime Eq. (1), gives an effective metric

$$g_{\text{eff}}^{\mu\nu} = \begin{pmatrix} 1 & \mathbf{v}_B^\parallel \\ \mathbf{v}_B^\parallel & \mathbf{v}_B^\parallel \otimes \mathbf{v}_B^\parallel - g h_B I \end{pmatrix}. \tag{6}$$

As mentioned before, this effective metric describes the effective spacetime geometry that the propagating waves experience. Note that the effective metric contains only background flow properties; the propagating waves do not influence the effective metric. For this reason, the physical analogy is a kinematic model of gravity: it models dynamic processes that take place in a stationary (but curved) spacetime.

For the case of a constant, one-dimensional background flow $\mathbf{v}_B^\parallel = v_B \mathbf{e}_x$, the effective metric becomes

$$g_{\text{eff}}^{\mu\nu} = \begin{pmatrix} 1 & v_B & 0 \\ v_B & v_B^2 - g h_B & 0 \\ 0 & 0 & -g h_B \end{pmatrix}, \tag{7}$$

with an inverse

$$g_{\mu\nu}^{\text{eff}} = \frac{1}{g h_B} \begin{pmatrix} g h_B - v_B^2 & v_B & 0 \\ v_B & -1 & 0 \\ 0 & 0 & -1 \end{pmatrix}. \tag{8}$$

The distance between two points in this effective spacetime is

$$ds^2 = \frac{1}{g h_B}\left[(g h_B - v_B^2)dt^2 + 2 v_B dt dx - dx^2 - dy^2\right]. \tag{9}$$

The motion of an analogue light particle, described by null-geodesics, is

$$(gh_B - v_B^2)dt^2 + 2v_B dt dx - dx^2 = 0\,, \tag{10}$$

which can be written as

$$((v_B + \sqrt{gh_B})dt - dx)((-v_B + \sqrt{gh_B})dt + dx) = 0\,. \tag{11}$$

For the case of a uniform background velocity, we can obtain the trajectories

$$x(t) = x_0 + (v_B \pm \sqrt{gh_B})t\,, \tag{12}$$

displayed in Fig. 3. The speed of propagation $(v_B \pm \sqrt{gh_B})$ is the velocity of the background flow plus (or minus) the propagation speed of surface gravity waves in the shallow water limit, see Section 2.4.1.

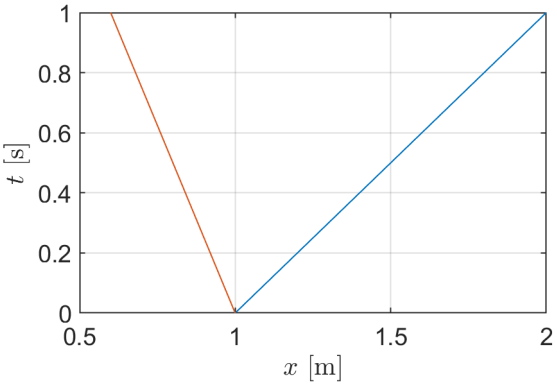

Figure 3: Null geodesics in the flat bottom effective metric, given by Eq. (12). The uniform background flow in the positive x-direction changes the propagation speeds of the waves. Parameters for this plot: $g = 9.81\,\mathrm{m\,s^{-2}}$, $x_0 = 1\,\mathrm{m}$, $h_B = 50\,\mathrm{mm}$ and $v_B = 0.3\,\mathrm{m\,s^{-1}}$.

2.2.1 General bottom profile

The flat bottom restriction can be loosened to derive an effective metric for a general bottom shape. The bottom is assumed to vary slowly; more specifically, the wavelength is assumed to be much smaller than the typical length associated to height changes, expressed as

$$\lambda \ll \frac{h_B(x)}{\frac{\mathrm{d}h_B}{\mathrm{d}x}}\,, \tag{13}$$

such that the individual waves perceive the bottom as flat and the flow as stationary. A new coordinate system is defined in which the vertical coordinate (z) is orthogonal to the bottom and geodesic. A spatial metric can be constructed for this bottom, in the form of

$$dr^2 = dz^2 + \eta_{ij} dx^i dx^j\,, \tag{14}$$

where i and j represent the coordinates inside the bottom. η_{ij} thus encodes the curvature of the bottom. The continuity and momentum equations in the new coordinate system are written as

$$\partial_i(\sqrt{\eta}v^i) + \partial_z(\sqrt{\eta}v^z) = 0\,, \tag{15}$$

$$\partial_t\Phi + \eta^{ij}(\partial_i\Phi)(\partial_j\Phi) + (\partial_z\Phi)^2 = -\frac{p}{\rho} - V\,, \tag{16}$$

where $\eta = \det(\eta_{ij})$, Φ is the velocity potential and V is a potential that includes gravity and external forces. The expressions are expanded in powers of z above $z = 0$,

$$\Phi(x^i, z) = \Phi_{(0)}(x^i) + z\Phi_{(1)}(x^i) + \frac{z^2}{2}\Phi_{(2)}(x^i) + \dots , \tag{17}$$

and similarly for the bottom metric η_{ij} and the background potential V. The expansions, together with the assumptions that all horizontal lengthscales are larger than the water height, lead to the wave-like equation from which the effective metric can be found for waves on a steady flowing background with a general bottom. The effective metric is

$$g^{\mu\nu}_{\text{eff}} = \frac{1}{h_B^2}\begin{pmatrix} 1 & v_B^i \\ v_B^j & v_B^i v_B^j - \tilde{g} h_B \eta^{ij}_{(0)} \end{pmatrix} , \tag{18}$$

with an effective gravity

$$\tilde{g} = g_z + \frac{1}{2}\eta^{ij}_{(1)}(\partial_i \phi_{(0)})(\partial_j \phi_{(0)}) . \tag{19}$$

The extra terms represent vertical centrifugal forces in the background flow and are negligible for slowly varying bottoms. It can be seen that experimental parameters such as the background flow velocities and the water height are present in the metric, which means that by choosing a particular flow setup, one may mimic any effective spacetime metric (as long as the desired flow setting is physically realisable and falls within the assumptions).

In the case where the background flow and the waves only move in the x-direction, the system reduces in dimensionality to one spatial and one temporal dimension, written in shorthand as (1+1)D. The effective spacetime metric in this case reduces to

$$g^{\mu\nu}_{\text{eff}} = \frac{1}{h_B^2}\begin{pmatrix} 1 & v_B \\ v_B & v_B^2 - g h_B \eta \end{pmatrix} , \tag{20}$$

with the indices $(\mu, \nu) = (t, x)$. The inverse is

$$g^{\text{eff}}_{\mu\nu} = \frac{h_B}{g\eta}\begin{pmatrix} h_B g\eta - v_B^2 & v_B \\ v_B & -1 \end{pmatrix} . \tag{21}$$

The null geodesics are given by

$$(g h_B \eta - v_B^2)dt^2 + 2 v_B dt dx - dx^2 = 0 , \tag{22}$$

which can be written as

$$((v_B + \sqrt{g h_B \eta})dt - dx)((-v_B + \sqrt{g h_B \eta})dt + dx) = 0 . \tag{23}$$

Note that the background velocity, water height, and curvature all depend on the x-coordinate. The effect of an accelerating background flow is illustrated using the following flow situation: a steady flow with a flat surface level which flows over a flat ($\eta = 1$), but sloped bottom profile (see Fig. 4 for a sketch of the flow configuration). The background water height is

$$h_B = \frac{h_{B0}}{L} x , \tag{24}$$

where L is the length of the slope, the background velocity will be

$$v_B = \frac{qL}{h_{B0} x} , \tag{25}$$

where q is the 2D flow rate. Using this flow setting, with parameters $h_{B0} = 0.1\,\text{m}$, $q = 0.01\,\text{m}^2\,\text{s}^{-1}$, $L = 1\,\text{m}$, Eq. (22) can be (numerically) integrated to obtain the null geodesics for the effective metric on a sloped bottom, which are plotted in Fig. 5. The background medium is flowing in the positive spatial direction and the effect on the trajectories is visible, as the incoming waves are slowed down. At some point, the ingoing trajectories become infinitely steep, which is the effective white hole horizon.

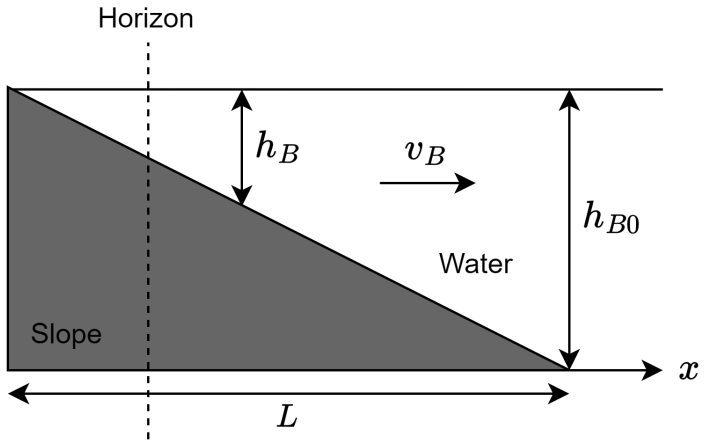

Figure 4: Example bottom profile to illustrate the behaviour of wave trajectories in inhomogeneous background flow. The trajectories of waves in this flow setting are shown in Fig. 5.

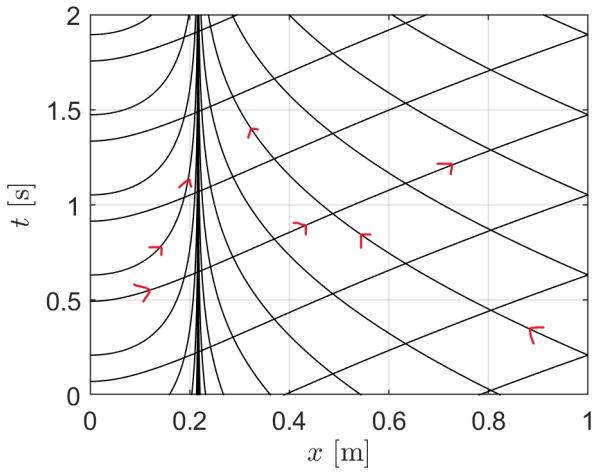

Figure 5: Null geodesics for an effective metric of water flowing over the linear slope shown in Fig. 4. The red arrows indicate the direction of propagation. The background flow generates a white hole horizon at $x \approx 0.2$; no waves propagating upstream can cross the white horizon. In the white hole interior ($x < 0.2$), wave propagation is only possible in the downstream direction. With parameters: $h_{B0} = 0.1\,\mathrm{m}$, $q = 0.01\,\mathrm{m}^2\,\mathrm{s}^{-1}$, $L = 1\,\mathrm{m}$.

In summary, there is a rigorous mathematical connection between the propagation of scalar fields through curved spacetime and the propagation of surface gravity waves in flowing water over a general bottom, under the condition that several approximations are valid:

- The water is assumed to have a constant density, which holds in the absence of salinity or temperature gradients. The incompressibility of water holds for speeds well below the speed of sound in water ($\approx 1500\,\mathrm{m\,s^{-1}}$).
- The water is assumed to have zero viscosity or negligible viscous effects on the lengths and timescales involved.
- The hydrostatic condition, which relates the pressure to the water height, is valid when no shear forces are acting in the flow.
- The flow is assumed to be irrotational, allowing the flow to be described by a velocity potential.
- The background flow is assumed to be time-independent.
- The wavelength of the perturbations is assumed to be much longer than the depth of the fluid ($h_B/\lambda \ll 1$), allowing higher-order terms in the Taylor expansion to be neglected, this is also referred to as the shallow water limit.
- For the case of a variable bottom profile, the local variation of the fluid height and the slope of the bottom are assumed to be sufficiently small.
- The effects of surface tension are neglected in the long-wave limit.
- The effective gravitational acceleration, which contains gravity and centrifugal forces on the fluid due to curvature, is assumed to be equal to just gravity.

2.3 Background flow

These sections examine the fluid mechanics within the setup, in particular, the expected water profiles for open-channel flow without or with obstacles.

2.3.1 Steady channel flow

In this section, the water height of the background flow, in the case of a flat bottom, is discussed. This open-channel, free-surface flow is similar to river flows commonly studied in the field of environmental fluid mechanics. [9] The system can be described in 1D by the Saint-Venant equations, which consist of a mass and a momentum conservation equation. The mass conservation is

$$\frac{\partial}{\partial t}A + \frac{\partial}{\partial x}(Av) = 0\,, \tag{26}$$

where A is the area of the water cross-section, and v the flow velocity. For a channel of constant width, mass conservation can be written in terms of the water height

$$\frac{\partial}{\partial t}h + \frac{\partial}{\partial x}(hv) = 0\,. \tag{27}$$

The momentum conservation for this system is

$$\frac{\partial}{\partial t}(\rho A v) + \frac{\partial}{\partial x}\left(\rho A v^2\right) = -\frac{\partial F_P}{\partial x} + \rho g A S - C_D \rho P v^2\,, \tag{28}$$

where ρ is the water density, F_P the pressure, $S = \sin\alpha$ the slope, C_D a friction coefficient and P the wetted perimeter. For a channel with a rectangular cross-section (like our setup), the wetted perimeter is $P = 2h + W$ and the area is $A = hW$, where W is the width of the channel. Furthermore, in our setup, the bottom is not angled, so $S = 0$. The momentum balance becomes

$$\frac{\partial}{\partial t}(hWv) + \frac{\partial}{\partial x}\left(hWv^2\right) = -\frac{1}{\rho}\frac{\partial F_P}{\partial x} - C_D(2h + W)v^2\,. \tag{29}$$

The pressure is obtained from the hydrostatic balance,

$$F_P = \int_0^h \rho g(h - z)W\,\mathrm{d}z = \frac{1}{2}W\rho g h^2\,. \tag{30}$$

The momentum balance becomes

$$\frac{\partial}{\partial t}(hWv) + \frac{\partial}{\partial x}\left(hWv^2\right) = -Wgh\frac{\partial h}{\partial x} - C_D(2h + W)v^2\,. \tag{31}$$

Extending the partial derivatives on the l.h.s. gives

$$W\left(h\frac{\partial v}{\partial t} + v\frac{\partial h}{\partial t} + 2hv\frac{\partial v}{\partial x} + v^2\frac{\partial h}{\partial x}\right) = -Wgh\frac{\partial h}{\partial x} - C_D(2h + W)v^2\,, \tag{32}$$

and by subtracting the mass conservation, Eq. (27), the momentum balance can be reduced to

$$\frac{\partial v}{\partial t} + v\frac{\partial v}{\partial x} = -g\frac{\partial h}{\partial x} - C_D\left(\frac{2}{W} + \frac{1}{h}\right)v^2\,. \tag{33}$$

The background flow is assumed to be steady, so time derivatives are neglected, yielding

$$v\frac{\mathrm{d}v}{\mathrm{d}x} = -g\frac{\mathrm{d}h}{\mathrm{d}x} - C_D\left(\frac{2}{W} + \frac{1}{h}\right)v^2\,. \tag{34}$$

It is useful to rewrite the equation in terms of the flow rate $Q = vhW$, which measures the volume of water that passes through a cross-section of the channel per unit of time,

$$-\frac{Q^3}{W^2h^3}\frac{\mathrm{d}h}{\mathrm{d}x} = -g\frac{\mathrm{d}h}{\mathrm{d}x} - C_D\left(\frac{2}{W} + \frac{1}{h}\right)\frac{Q^2}{W^2h^2}\,. \tag{35}$$

Rearranging terms gives

$$\left(1 - \frac{Q^2}{gW^2h^3}\right)\frac{\mathrm{d}h}{\mathrm{d}x} = -C_D\left(\frac{2h}{W} + 1\right)\frac{Q^2}{gW^2h^3}\,, \tag{36}$$

from which we can identify the dimensionless Froude number

$$\mathrm{Fr}^2 = \frac{v^2}{gh} = \frac{Q^2}{gW^2h^3}\,. \tag{37}$$

The Froude number is the ratio between the flow inertia and gravity. With the Froude number, the equation for the water level can be written as

$$\left(1 - \mathrm{Fr}^2\right)\frac{\mathrm{d}h}{\mathrm{d}x} = -C_D\left(\frac{2h}{W} + 1\right)\mathrm{Fr}^2\,. \tag{38}$$

The change in height is smaller than the height itself ($\Delta h \ll h_0$), so the Froude number is approximately constant over the domain: $\mathrm{Fr}_0^2 = \frac{Q^2}{gW^2h_0^3}$. We get

$$\left(1 - \mathrm{Fr}_0^2\right) \frac{\mathrm{d}h}{\mathrm{d}x} = -C_D \left(\frac{2h}{W} + 1\right) \mathrm{Fr}_0^2 , \tag{39}$$

which has solution

$$h(x) = -\frac{W}{2} + C_0 \exp\left(-\frac{2C_D \mathrm{Fr}_0^2}{(1 - \mathrm{Fr}_0^2)W} x\right) . \tag{40}$$

The integration constant C_0 can be determined by the boundary condition $h(L) = h_0$, which is the water height at the end of the channel, which gives

$$C_0 = \left(h_0 + \frac{W}{2}\right) \exp\left(\frac{2C_D \mathrm{Fr}_0^2}{(1 - \mathrm{Fr}_0^2)W} L\right) , \tag{41}$$

resulting in a water level profile

$$h(x) = -\frac{W}{2} + \left(h_0 + \frac{W}{2}\right) \exp\left(\frac{2C_D \mathrm{Fr}_0^2}{(1 - \mathrm{Fr}_0^2)W} (L - x)\right) . \tag{42}$$

Fig. 6 visualises the water levels predicted by Eq. (42). In Fig. 6a, the height profiles are plotted for different friction coefficient values (C_D), with a constant outflow height (h_0). All other parameter values are takenso to be representative of the experimental setup used in this work. A channel with a higher friction leads to a steeper slope in the water surface level. In Fig. 6b, the height profiles are plotted for different outflow heights, while keeping the friction coefficient constant. Larger water heights show milder water level slopes.

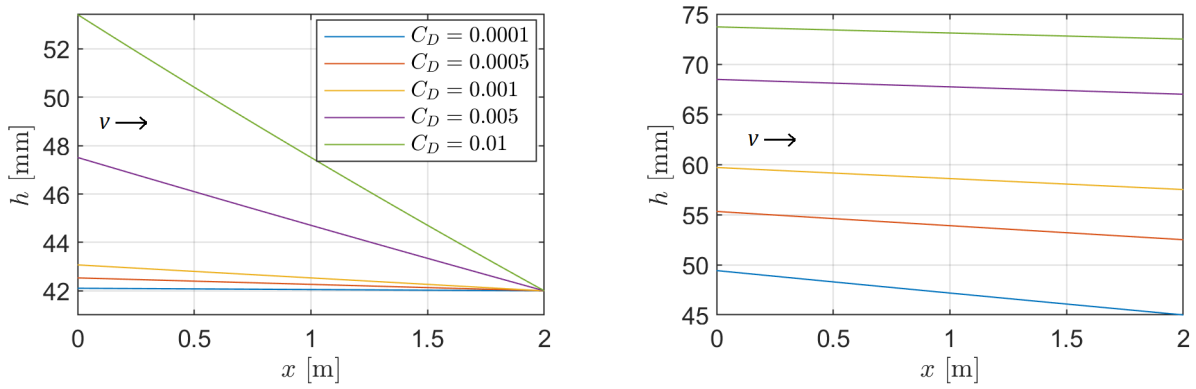

(a) **(b)**

Figure 6: Visualisations of the predicted steady water level, in the presence of a flow, by Eq. (42). With parameters: $W = 70\,\mathrm{mm}$, $Q = 8.33 \times 10^{-4}\,\mathrm{m^3\,s^{-1}}$ **(a)**: Height profiles for different friction coefficients C_D, with a constant outflow height, $h_0 = 42\,\mathrm{mm}$. Larger friction coefficients lead to a steeper slope. **(b)**: Steady water levels for varying outflow heights, for a constant friction coefficient $C_D = 0.005$, showing that the effect of friction on the water slope is larger for lower water levels.

The exponential nature of the water level drop is hardly visible, because, the exponent being small, it can be approximated as $\exp(x) \approx x + 1$, which gives a predicted water level slope:

$$\frac{\mathrm{d}h}{\mathrm{d}x} = -\left(h_0 + \frac{W}{2}\right) \frac{2C_D \mathrm{Fr}_0^2}{(1 - \mathrm{Fr}_0^2)W} . \tag{43}$$

Fig. 7 illustrates the influence of the friction coefficient and the outflow height on the slope of the water level. These theoretical predictions are compared with the experimental results in Section 4.1, see Fig. 45.

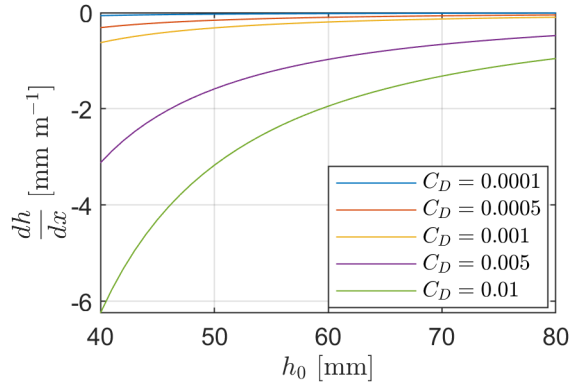

Figure 7: Predicted water level slope for a steady flow, given by Eq. (43), as a function of the outflow height, h_0, for various values of the friction coefficient, C_D. The flow rate is kept constant. With parameters: $W = 70\,\mathrm{mm}$, $Q = 8.33 \times 10^{-4}\,\mathrm{m^3\,s^{-1}}$. This figure shows the effects of Figs. 6a and 6b combined: larger friction coefficients and lower water levels lead to larger slopes.

2.3.2 Shallow water equations

To describe the effect of a variable bottom on the background flow, the equations that govern the flow, Eqs. (2) and (3), can be integrated over the height of the fluid, under the assumption that the horizontal velocity scales are much larger than the vertical velocity scales. What results are the shallow water equations:

$$\frac{\partial \eta}{\partial t} + \frac{\partial}{\partial x}(v_x \eta) + \frac{\partial}{\partial y}(v_y \eta) = 0\,, \tag{44}$$

$$\frac{\partial v_x}{\partial t} + v_x \frac{\partial v_x}{\partial x} + v_y \frac{\partial v_x}{\partial y} = -g \frac{\partial h}{\partial x}\,, \tag{45}$$

$$\frac{\partial v_y}{\partial t} + v_x \frac{\partial v_y}{\partial x} + v_y \frac{\partial v_y}{\partial y} = -g \frac{\partial h}{\partial y}\,, \tag{46}$$

where $\eta = h - h_{bot}$ is the actual height of the water column. These equations differ from those derived in the previous section, as the effect of friction is ignored here. In a steady state, $\frac{\partial}{\partial t} = 0$, and in a 1D setup, one of the horizontal dimensions can be removed: $v_y = 0$ and $\frac{\partial}{\partial y} = 0$. The system of equations is reduced to

$$v_x \left(\frac{\mathrm{d}h}{\mathrm{d}x} - \frac{\mathrm{d}h_{bot}}{\mathrm{d}x} \right) + (h - h_{bot}) \frac{\mathrm{d}v_x}{\mathrm{d}x} = 0\,, \tag{47}$$

$$v_x \frac{\mathrm{d}v_x}{\mathrm{d}x} = -g \frac{\mathrm{d}h}{\mathrm{d}x}\,. \tag{48}$$

This set of equations can be solved numerically for a given flow rate q and a bottom height profile h_{bot}. In Fig. 8, the height profiles obtained numerically for flow over a smooth bottom bump are illustrated. It is evident from the plot that the presence of the bump leads to a reduction in water height above it.

An advantage of the water wave analogy is that the effective metric can be experimentally chosen by setting up a certain background flow. Experimentally, this consists of accurately choosing the shape of the bottom, the flow rate, and the water height at the outflow. The shallow water equations demonstrate

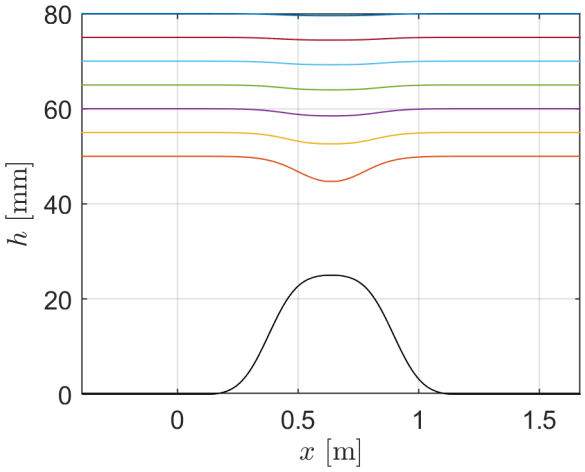

Figure 8: Numerically solved shallow water equations, Eqs. (47) and (48), for a flow over a smooth bump. The flow profiles show a dip in the water level right above the obstacle. Plotted for a flow rate $q = 0.0069\,\mathrm{m}^2\,\mathrm{s}^{-1}$.

that the surface of the water does not necessarily remain flat when obstacles are placed in the flow, which must be taken into account when the aim is to model a specific spacetime geometry.

2.4 Water waves

Since the analogue gravity model employs water waves, it will be helpful to discuss the theory behind wave propagation in water, and specifically the propagation of waves in a background flow.

Waves are characterised by a wavelength, λ, and a frequency, ω. The wavelength describes the size of the waves and the frequency measures how many waves cross a point in space per time period, $\omega = \frac{2\pi}{T}$. It is more convenient to work with a wavenumber, defined as $k = \frac{2\pi}{\lambda}$, such that the dimensionality of the wave characteristics is 1/length and 1/time. Waves cannot have any combination of wavelength and frequency; instead, the wavenumber and frequency of the waves are related via the so-called dispersion relation, which will be an integral part of the following discussion.

In the following sections, linear wave theory in still water is discussed, leading to the dispersion relation of surface gravity waves. Following this, the wave behaviour within a flow is analysed, including the introduction of two measurement frames, that of a stationary and co-moving observer. It will be demonstrated that, due to these measurement frames, multiple wavenumbers can exist for certain wave frequencies. Further discussions include wave blocking by counterflow, as well as the impact of surface tension and viscosity.

2.4.1 Linear wave theory

Linear wave theory, or Airy wave theory, describes propagating surface waves with a small wave amplitude to water depth ratio. The theory discussed here can be found in more detail in James Lighthill's book "Waves in Fluids". [10] Wave properties can be derived using the potential flow framework, introduced in Section 2.2, starting from Eq. (4), which describes an incompressible, inviscid, irrotational fluid of uniform density in terms of a velocity potential $\mathbf{v} = \boldsymbol{\nabla}\phi$, and together with the assumption that the bottom is flat and assuming small wave amplitudes, the velocity potential

$$\phi = \frac{a\omega}{k}\frac{\cosh k(z+H)}{\sinh kH}\sin(kx - \omega t) \tag{49}$$

is found. From this, fluid parcel trajectories can be derived, which are displayed in Fig. 9, and nicely visualise the wave as a complete structure, not only a surface perturbation. At the wave peaks, the fluid velocity is in the direction of wave propagation, and at the troughs it is in the opposite direction. Near the bottom, the tracers show a nearly horizontal motion.

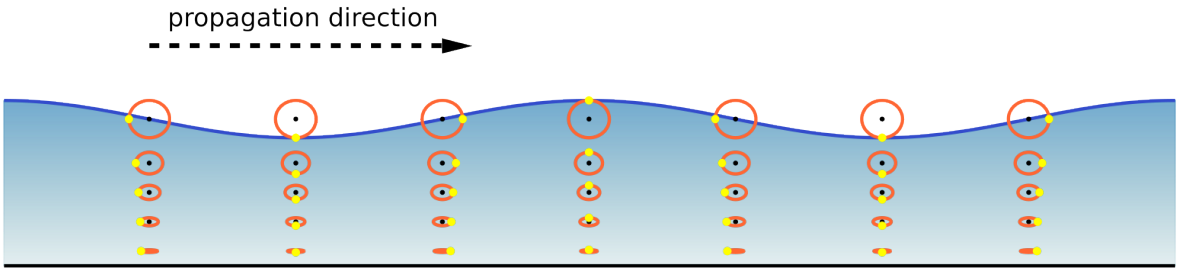

Figure 9: Structure of linear waves. The orange circles show the orbits of fluid parcels as the wave passes through the system. Image credit: Ref. [11].

The variable of interest is the perturbed height of the water interface, δh, which can also be derived from the velocity potential:

$$\delta h = a\cos(kx - \omega t)\,, \tag{50}$$

which describes, as expected, a travelling wave. Furthermore, the dispersion relation mentioned at the start of this section can be derived from the velocity potential, giving

$$\omega^2 = gk\tanh(kh)\,, \tag{51}$$

which relates the wavenumber and the frequency of the waves. The dispersion relation (Eq. (51)) is plotted in Fig. 10. There are two branches since it is quadratic in ω, one corresponding to waves travelling in a positive direction and one corresponding to waves travelling in a negative direction. Of course, in stationary water, the properties of the waves are independent of the propagation direction, which is visible from the symmetry in the plot. For now, we focus on waves with a positive wavenumber

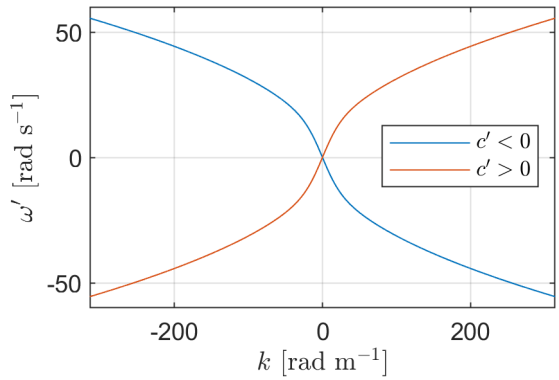

Figure 10: Dispersion relation for gravity waves, Eq. (51), which relates the wavenumber and frequency of surface gravity waves. The two curves correspond to waves in opposite directions. Plotted for $h = 50\,\mathrm{mm}$.

and frequency. The propagation velocity of a point of constant phase along the wave is given by

$$c_\phi = \pm\frac{\omega}{k} = \sqrt{\frac{g}{k}\tanh(kh)}\,, \tag{52}$$

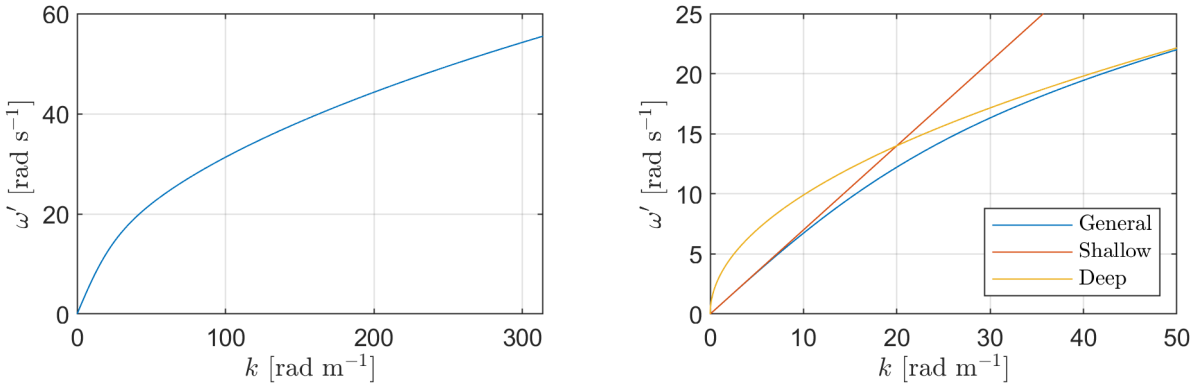

(a) **(b)**

Figure 11: (a): Positive branch of the dispersion relation, $\omega = \sqrt{gk\tanh(kh)}$. **(b)**: Close-up of (a) at lower wavenumbers, including shallow and deep water approximations, $\omega_{shallow} = k\sqrt{gh}$ and $\omega_{deep} = \sqrt{gk}$. Plotted for $h = 50\,\text{mm}$.

and it is plotted in Fig. 12a, as a function of the wavenumber, k.

The phase velocity of waves with a larger wavenumber (thus a shorter wavelength) is smaller compared to waves with a smaller wavenumber. Unfortunately, this is not the case for the system which we aim to simulate, as the propagation speed of light (in vacuum) is universally constant and independent of frequency. However, as light propagates through materials, a frequency-dependent refractive index can lead to dispersion, but that is not the system under consideration.

In the limit of shallow water, $kh \ll 1$, the hyperbolic tangent can be approximated as $\tanh(kh) \approx kh$ and the phase velocity of the waves becomes $c_\phi = \sqrt{gh}$, which is independent of the wavenumber and therefore behaves more closely to the light propagation in vacuum. On the other hand, in the limit of deep water, $kh \gg 1$, the hyperbolic tangent can be approximated as $\tanh(kh) \approx 1$, and $c_\phi = \sqrt{\frac{g}{k}}$. The dispersion relations in these different limits are plotted in Figs. 11b and 12b for the frequency and phase velocity, respectively.

In addition to the phase velocity, there exists a group velocity, which comes into play when considering wave packets. The group velocity

$$c_g = \frac{\mathrm{d}\omega}{\mathrm{d}k} = c_\phi \left(\frac{1}{2} + \frac{kh}{\sinh(2kh)} \right) \tag{53}$$

describes the propagation speed at which the overall shape of a wave packet propagates through the medium, and this may be different from the phase velocity of the waves inside the group. The group velocity is plotted in Fig. 13, together with the phase velocity, for different wavenumbers. In the shallow water limit, the two velocities coincide, and in the deep water limit, the group velocity is half the phase velocity.

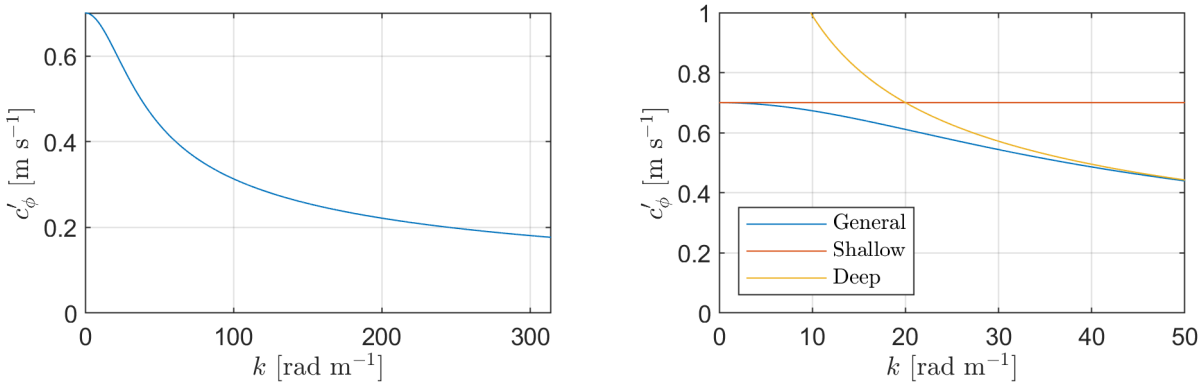

Figure 12: **(a)**: phase velocity of positive branch of the dispersion relation, $c_\phi = \sqrt{\frac{g}{k}\tanh(kh)}$. Waves with a larger wavenumber have a lower phase velocity. **(b)**: Close-up of (a) at lower wavenumbers, including shallow and deep water approximations, $c_{shallow} = \sqrt{gh}$ and $c_{deep} = \sqrt{\frac{g}{k}}$. In the shallow water limit, all wavenumbers have equal phase velocity, like like light waves in a vacuum. Plotted for $h = 50\,\text{mm}$.

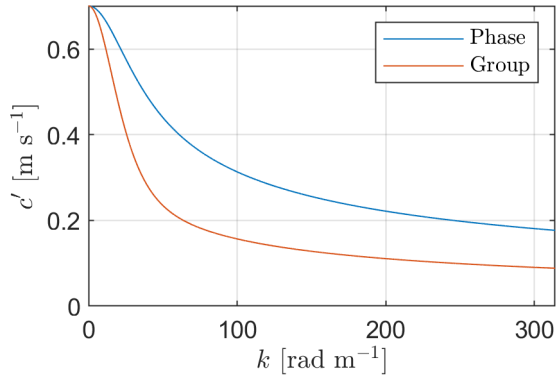

Figure 13: phase and group velocity dependence on wavenumber. Plotted for $h = 50\,\text{mm}$.

2.4.2 Waves in a flow

In the previous section, surface waves propagating in stationary water were considered; the discussion is extended by introducing a background flow for the waves to propagate in. This background flow breaks the symmetry in the dispersion relation: for a stationary observer (for example, someone standing on a river bank), the waves travelling up or downstream are no longer equivalent. The stationary observer is referred to as the laboratory frame, and an observer moving along with the background flow is referred to as the co-moving frame. In this co-moving frame, the water is perceived to be stationary.

Consider waves that are travelling upstream a flow v. The background flow is defined to move in the positive x direction; therefore, waves that travel downstream have positive velocities and waves that travel upstream have negative velocities in the laboratory frame.

As mentioned, the system can be described in two coordinate systems: the stationary, or laboratory, coordinates, denoted with unprimed quantities, and the co-moving coordinate frame, denoted with primed quantities. Fig. 14 shows a sketch of these coordinate systems. The relation between the coor-

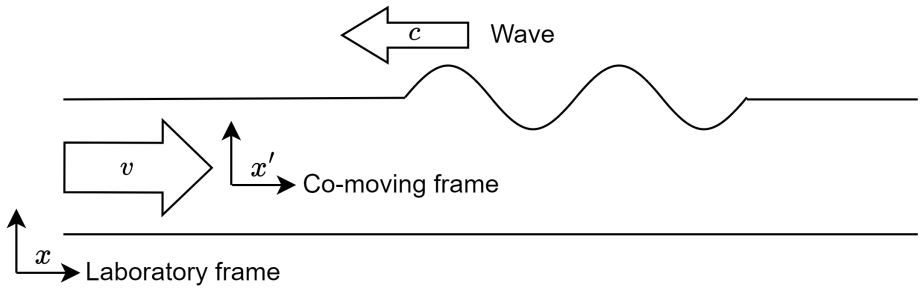

Figure 14: Laboratory frame x and co-moving frame x'. The co-moving frame is moving along with the background flow. The relation between the coordinates systems is $\mathrm{d}x = \mathrm{d}x' + v\,\mathrm{d}t'$, $\mathrm{d}t = \mathrm{d}t'$.

dinates systems is

$$\mathrm{d}x = \mathrm{d}x' + v\,\mathrm{d}t' \tag{54}$$

$$\mathrm{d}t = \mathrm{d}t' \ . \tag{55}$$

Lengths are invariant under this coordinate change, so the wavelengths and the wavenumbers of waves are equal in both coordinate frames, $k' = k$. The evolution of the waves can be described by the phase ϕ:

$$\phi = \int (k\,\mathrm{d}x - \omega\,\mathrm{d}t)\,, \tag{56}$$

which is a constant along, for instance, a wave peak. Using Eqs. (54) to (56), a relation can be found for wave frequencies in the laboratory and co-moving frame,

$$\omega' = \omega - vk\,. \tag{57}$$

This relation can be understood by considering waves travelling downstream with some co-moving frame frequency. The stationary observer will record more waves passing per time, which amounts to a larger frequency, as Eq. (57) states. The effect of the coordinate transformation on the dispersion relation is visualised in Fig. 15, where the dispersion relation in the co-moving frame and in the laboratory frame are plotted side-by-side. In the co-moving frame, where the water is at rest, ω' can only depend on k (and the intrinsic properties of the medium), while the dispersion relation as perceived in the laboratory frame

$$(\omega - vk)^2 = gk\tanh(kh)\,, \tag{58}$$

also depends on the velocity of the flow.

In this work, we focus on waves that originate from a wave generator. The generated waves are initially travelling upstream in the co-moving frame (in the negative x'-direction), see Fig. 14. Therefore, we can neglect the branch where $c' > 0$. The waves that can exist in the system are intersections of the dispersion relation and the wave generator frequency, these are plotted in Fig. 16. The two plots are equivalent; they only differ in observer.

For specific flow parameters, there are three intersections between the dispersion relation and the wave generator frequency. The intersection point with a wavenumber closest to zero is the wave which is created by the wave generator, denoted by k_{in}. Two extra intersections exist, k_{out} and k_{out}^-, with much larger absolute wavenumbers, corresponding to shorter wavelengths. k_{out} has the same frequency sign as the incident wave, and k_{out}^- has the opposite frequency sign as the incident wave, which is considered the 'negative frequency' wave. Waves corresponding to the two extra intersections are labelled as the

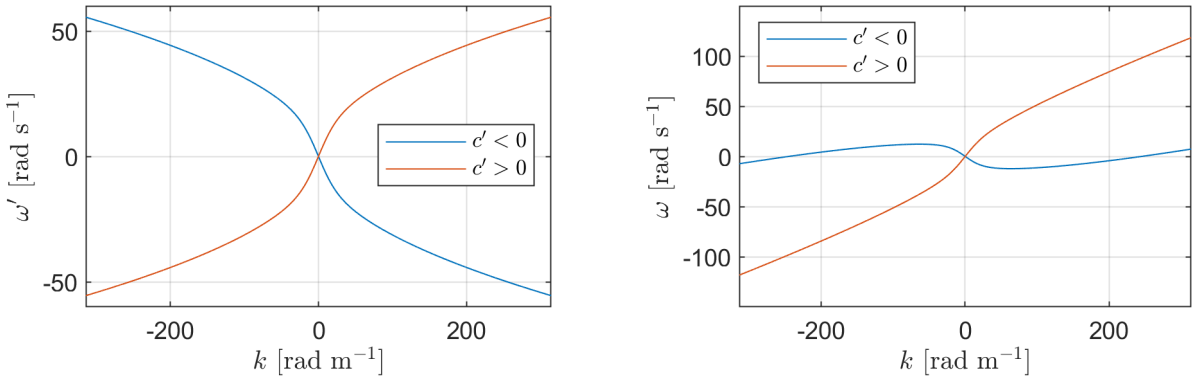

(a) Co-moving frame **(b)** Laboratory frame

Figure 15: The effect of the coordinates transformation on the dispersion relation, given by Eqs. (51) and (57). The coordinate transformation from the co-moving frame to the laboratory frame breaks the symmetry of the dispersion relation: waves which are propagating with equal and opposite frequencies in the co-moving frame (where the water is stationary) no longer do so in the laboratory frame. Plot parameters: $v = 0.2\,\mathrm{m\,s^{-1}}$ and $h = 50\,\mathrm{mm}$.

'converted waves' since they are not created by the wave generator. In the laboratory frame, Fig. 16b, these three intersections all have the same frequency, namely the wave generator frequency, but differ in wavenumber, phase velocity, and group velocity. As stated in Refs. [8, 12, 7], the conversion of the k_{in} wave to the k_{out} and k_{out}^{-} waves is in analogy to the inverse Hawking process, where a wave incident on a white hole horizon is transformed into two high-frequency waves of opposite sign, see Section 2.1.

The mathematical framework behind the analogy was derived in the shallow water limit. In this limit, however, the dispersion relation is linear in the wavenumber: $\omega' = k\sqrt{gh}$, which would give a straight line in Fig. 16a and would never give rise to the two extra intersection points. Therefore, in the study of the converted waves, the shallow water approximation is automatically invalidated, making the analogy to general relativity less exact.

When the waves propagate against a counterflow, the velocity of the waves is reduced in the eyes of a stationary observer (the laboratory frame), as described by

$$c = \frac{\omega}{k} = v \pm \sqrt{\frac{g}{k}\tanh(kh)} = v \pm c'\,, \tag{59}$$

where $c' = \frac{\omega'}{k'}$ is the propagation velocity of the waves in the co-moving frame. In Fig. 17a, the phase velocity of the waves in the co-moving frame is plotted. The wavenumbers corresponding to the allowed waves are indicated. From the plot, it is clear that the converted waves propagate much slower than the generated waves, with speeds close to the speed of the background flow. Therefore, in experiments, we must look for slowly propagating waves.

The group velocities of the converted waves, plotted in Fig. 17b, are lower than the speed of the background flow, which means that the wavepackets of converted waves will always be washed downstream in the laboratory frame.

Of course, the specific wavenumbers of the intersection points (or even the existence thereof) depend on the parameters of the flow situation (v, h, ω_{wg}). In Fig. 18, the dispersion relation in the laboratory frame is plotted for different water heights, representing different parts of the setup. The flow rate ($q = vh$) is constant, so the background flow speed and water height change simultaneously.

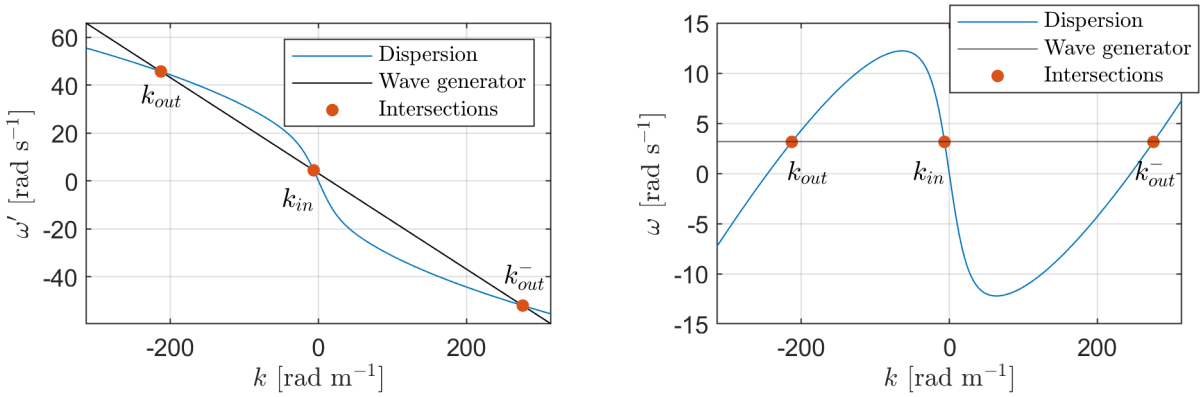

(a) Co-moving frame **(b)** Laboratory frame

Figure 16: Upstream branch of gravity wave dispersion relation (Eq. (51) in co-moving frame and Eq. (58) in laboratory frame) and wave generator frequency ($\omega'_{wg} = \omega_{wg} - vk$ in co-moving frame and ω_{wg} in laboratory frame). The two curves show three intersections: k_{in}, the wave created by the wave generator which is incident on the white hole horizon and the extra intersections k_{out} and k_{out}^- which appear as a result of the background flow. Note that k_{in} is not at the origin. Plot parameters: $v = 0.2\,\mathrm{m\,s^{-1}}$, $h = 50\,\mathrm{mm}$ and $\omega_{wg} = 3.14\,\mathrm{rad\,s^{-1}}$.

Fig. 19 shows an effective phase diagram, which displays the number of intersections between the dispersion relation and the wave generator frequency, for different values of the background flow and wave generator frequency. This plot therefore shows the window of opportunity in parameter space where the converted waves may be present.

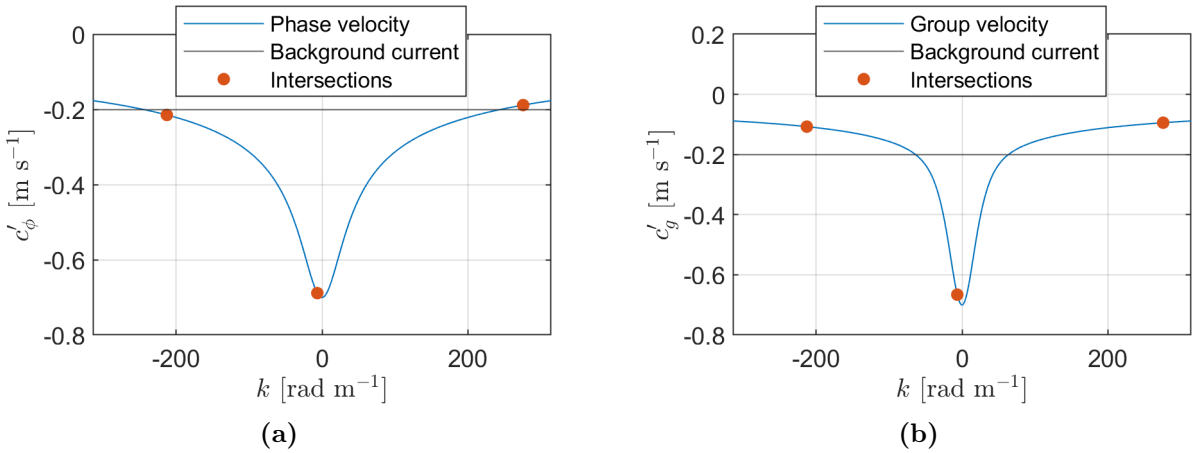

(a) **(b)**

Figure 17: The intersection points of the dispersion relation with the wave generator frequency are indicated by red dots, along with a horizontal line denoting the background flow speed. The low wavenumber intersection, which is the wave that is created at the wave generator, moves upstream with moderate speed. The large wavenumber solution with equal sign frequency is moving upstream with a speed just above the background flow. Lastly, the large wavenumber solution with opposite sign velocity is moving upstream at a speed slightly slower than the background flow, and will therefore be moving downstream in the laboratory frame. Plot parameters: $v = 0.2\,\mathrm{m\,s^{-1}}$, $h = 50\,\mathrm{mm}$ and $\omega_{wg} = 3.14\,\mathrm{rad\,s^{-1}}$.

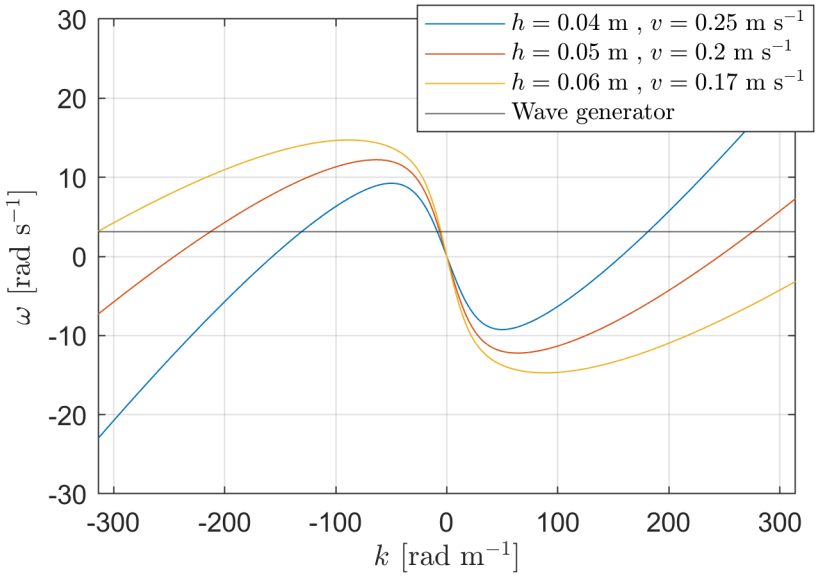

Figure 18: Dispersion relation in the laboratory frame for different water heights, for a constant flow rate, showing how the wavenumbers of the intersection points are influenced by changing the water height. In general, a larger water height, and thus lower speed, will increase the magnitude of the wavenumber of the converted waves, potentially making it more challenging to observe. Plotted with $\omega_{wg} = 3.14\,\mathrm{rad\,s^{-1}}$.

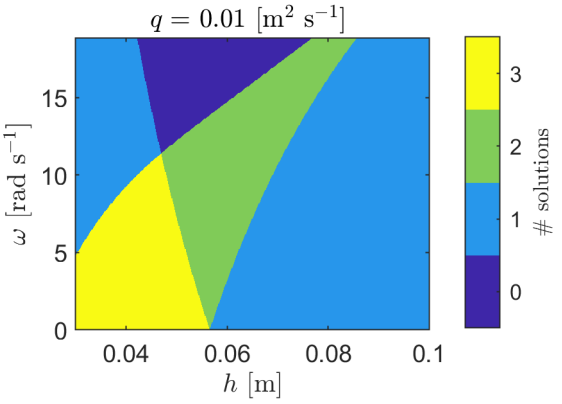

Figure 19: Diagram showing the number of intersection points between the dispersion relation and the wave generator frequency for a fixed flow rate. The yellow area (corresponding to three intersections) indicates for which combination of water height and wave generator frequency the converted waves may exist.

2.4.3 Capillarity

In the discussions before, the influence of surface tension on the waves has not been considered. In this section, the effect of surface tension on the waves is introduced and discussed.

Surface tension arises because molecules on the surface of a liquid experience different forces compared to those in the bulk. Molecules inside the liquid are surrounded by other molecules, and thus they experience balanced attractive forces from all directions. However, molecules on the surface lack neighbouring molecules on one side, resulting in an unbalanced force that pulls them inward. This inward pull causes the surface to contract and behave as an elastic sheet under tension. This tension minimises the surface area, giving rise to the characteristic behaviour of droplets and bubbles. The magnitude of this surface tension is quantified by the energy required to increase the surface area of the liquid. [13]

The dispersion relation for water waves, including surface tension, is [10]

$$\omega'^2 = \left(gk + \frac{\sigma}{\rho}k^3\right)\tanh(kh)\,, \tag{60}$$

where $\sigma = 0.072\,\mathrm{N\,m^{-1}}$ is the surface tension for tap water and $\rho = 1000\,\mathrm{kg\,m^{-3}}$ the density. The additional term ($\mathcal{O}(k^3)$), due to surface tension, acts as an extra restoring force, effectively speeding up the waves. This additional term becomes relevant at large wavenumbers (short wavelengths). In the laboratory frame, the dispersion relation with surface tension becomes

$$(\omega - vk)^2 = \left(gk + \frac{\sigma}{\rho}k^3\right)\tanh(kh)\,. \tag{61}$$

In Figs. 20 to 23, the earlier displayed figures are repeated, but with the inclusion of surface tension.

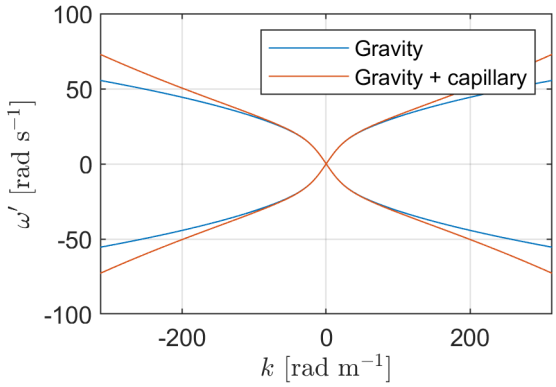

Figure 20: Dispersion relation for gravity waves in stationary water plus the effect of surface tension. The surface tension increases the frequency, and therefore the propagation speed of the waves. Plot parameters: $\rho = 1000\,\mathrm{kg\,m^{-3}}$, $h = 50\,\mathrm{mm}$ and $\sigma = 0.072\,\mathrm{N\,m^{-1}}$.

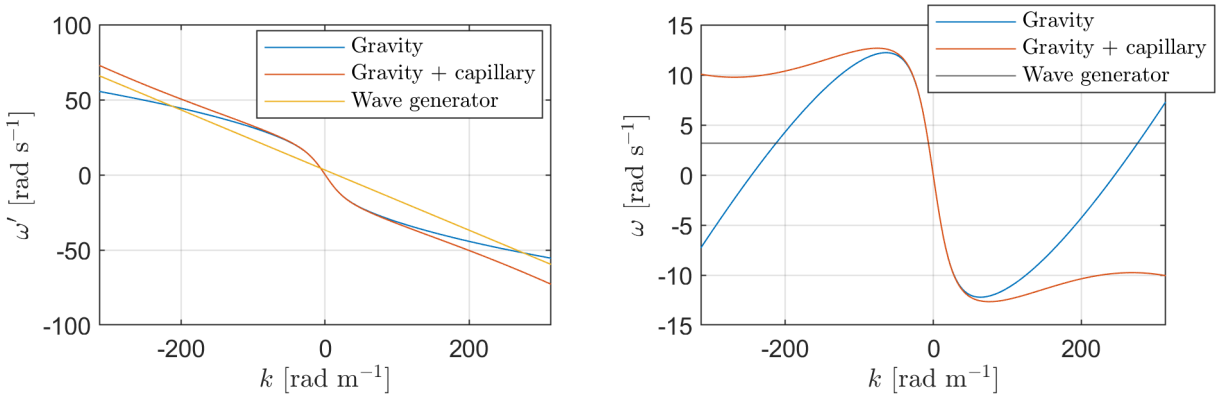

(a) Co-moving frame **(b)** Laboratory frame

Figure 21: Replot of Fig. 16b, with the addition of the dispersion curves for waves including the effect of surface tension (given by Eqs. (60) and (61) for the co-moving and the laboratory frame, respectively). It can be seen that, due to surface tension, the extra two intersections between the dispersion relation and the wave generator frequency disappear. Plot parameters: $\rho = 1000\,\mathrm{kg\,m^{-3}}$, $v = 0.2\,\mathrm{m\,s^{-1}}$, $h = 50\,\mathrm{mm}$, $\sigma = 0.072\,\mathrm{N\,m^{-1}}$ and $\omega_{wg} = 3.14\,\mathrm{rad\,s^{-1}}$.

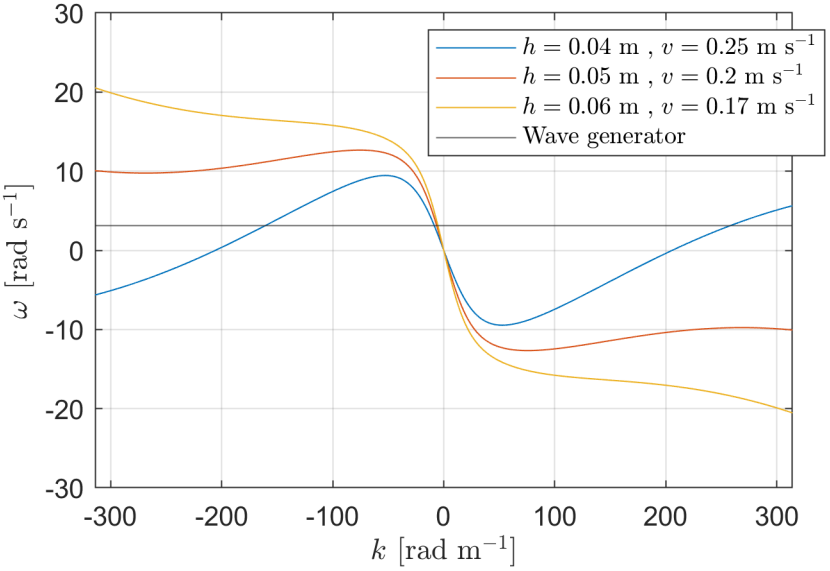

Figure 22: Dispersion relation including the effect of surface tension, given by Eq. (61) in the laboratory frame plotted for different water heights. The surface tension, which increases the frequency of the waves, makes the two intersection points corresponding to the converted waves, which are visible in Fig. 18, disappear for larger water heights. Plot parameters: $\rho = 1000\,\mathrm{kg\,m^{-3}}$, $\sigma = 0.072\,\mathrm{N\,m^{-1}}$ and $\omega_{wg} = 3.14\,\mathrm{rad\,s^{-1}}$.

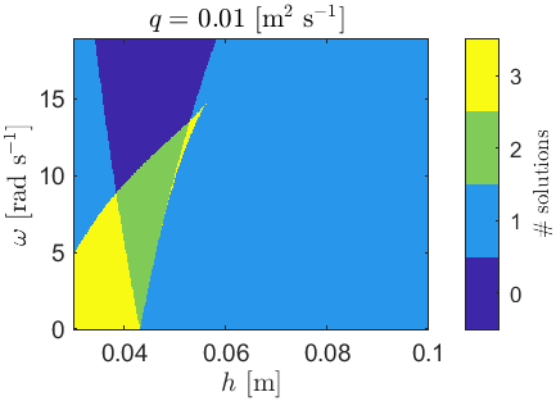

Figure 23: Diagram showing the number of intersection points between the dispersion relation and the wave generator frequency for a fixed flow rate, including the effects of surface tension. The yellow area (corresponding to three intersections) indicates for which combination of water height and wave generator frequency the converted waves may exist, and due to the effects of surface tension, this region becomes much smaller compared to Fig. 19.

From Figs. 20 to 23, it can be concluded that the effect of surface tension makes it more difficult to observe the converted waves. Increasing the scale of the setup will decrease the relative effect of surface tension, as the capillary length scale is an intrinsic property. However, as noted in Section 2.2, the mathematical basis of the analogy requires the wavelength of the waves to be much larger than the water height. Scaling up also means that the background flow speed must increase to match the increasing propagation speed of the waves. Both the increasing length scales and velocities might lead to complications due to the generation of turbulence.

2.4.4 Wave blocking

In the simplest sense, wave blocking will occur when the propagation speed of the wave is equal to the counterflow speed against which it propagates. For shallow water waves, the fastest waves that exist in the system, wave blocking occurs at a flow speed of $v = \sqrt{gh}$, or equivalently at $\mathrm{Fr} = \frac{v}{\sqrt{gh}} = 1$. However, from the dispersion relation, it follows that the propagation velocity of the waves decreases with increasing wavenumber; therefore, wave blocking for waves with larger wavenumbers will occur already at lower background flow speeds. Additionally, as the waves approach the obstacle, the blocking is caused both by an increase in counterflow and by a reduced water height, both aspects leading to a reduction in (laboratory frame) propagation speed.

To illustrate this process, Fig. 24a shows the laboratory frame dispersion relation for a fixed flow rate but varying water height and background flow speed ($q = hv = \text{constant}$), corresponding to different parts close to the blocking point, indicated in Fig. 24b.

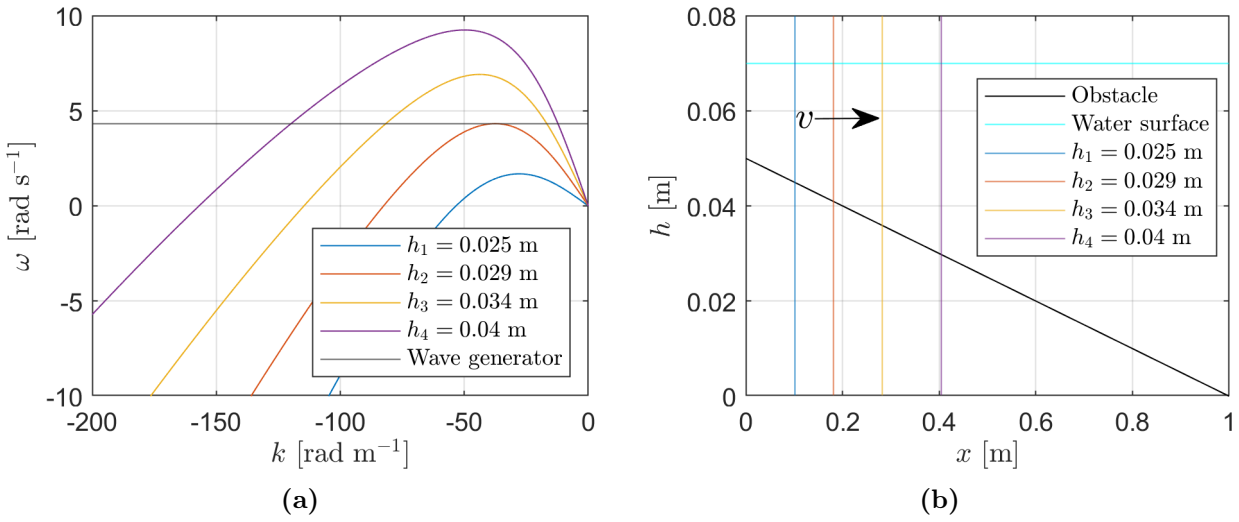

Figure 24: (a): Laboratory frame dispersion relation for a fixed flow rate but varying water height and background flow speed ($q = hv = 0.010\,\mathrm{m^2\,s^{-1}}$), corresponding to different parts close to the blocking point, indicated in (b). The intersection (with the lowest absolute wavenumber) between the dispersion relation and the wave generator frequency (horizontal black line) gives the wavenumber of the propagating wave. As the wave propagates towards the obstacle, its absolute wavenumber increases until the blocking point (h_2). **(b)**: Sketch of the flow situation, indicating the locations for which the dispersion curves in (a) are plotted.

The intersection (with the lowest absolute wavenumber) of the dispersion relation and with the wave generator frequency (horizontal line) gives the properties of the generated waves. The intersection wavenumber increases in magnitude as the wave approaches the obstacle. The dispersion curve for which the peak and the wave generator frequency coincide is the blocking point (h_2). The wavenumber at the blocking point stays finite.

For a point in the setup further upstream of the blocking point (h_1), no (upstream propagating) intersections with the wave generator frequency exist, meaning that the region is forbidden, this is the white hole interior.

To find the blocking point, the equation

$$\frac{\mathrm{d}\omega}{\mathrm{d}k} = \frac{\mathrm{d}}{\mathrm{d}k}\left[vk - \sqrt{gk\tanh\left(k\frac{q}{v}\right)}\right] = 0 \tag{62}$$

is numerically solved. Fig. 25 shows the Froude number at which each wave frequency is expected to be blocked. As expected, the lowest wave generator frequency, generating the longest wave, will be blocked at Fr = 1. Waves of increasing wavenumber will be blocked at decreasing Froude numbers. The Froude number at which waves of different frequencies are blocked is measured in Section 4.9.1.

For a given Froude number at the obstacle, wave frequencies below the blocking frequency are transmitted, and frequencies above the blocking frequency are blocked, effectively behaving like a physical low-pass filter.

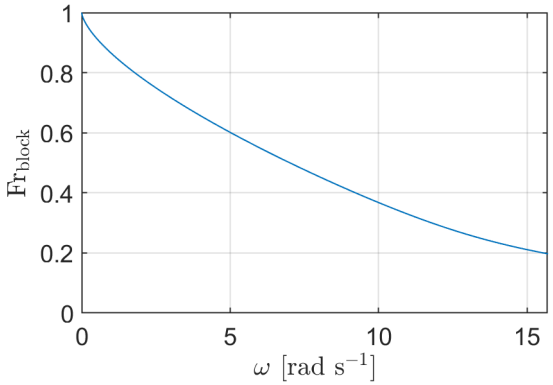

Figure 25: Froude number ($\mathrm{Fr}_{\mathrm{block}}$) at which different laboratory frame wave frequencies are blocked, calculated using Eq. (62) with $q = 0.010\,\mathrm{m}^2\,\mathrm{s}^{-1}$.

2.4.5 Viscosity

In the discussions so far, the water is assumed to have zero viscosity. In reality, water has a small viscosity of $\nu = 1\times10^{-6}\,\mathrm{m}^2\,\mathrm{s}^{-1}$. The effect of this small viscosity is the damping of the wave amplitudes. Consider a wave in an inviscid medium, given by

$$\delta h(x,t) = a\sin(kx - \omega t)\,. \tag{63}$$

Then, the same wave in a (slightly) viscous medium will be given by [14]

$$\delta h(x,t) = a_0 \exp\left(-2\nu k^2 t\right)\sin(kx - \omega t)\,. \tag{64}$$

The extra term acts as a damping of the wave amplitude over time. A characteristic timescale of wave decay can be defined as

$$\tau = \frac{1}{2\nu k^2}\,. \tag{65}$$

The characteristic decay time is plotted in Fig. 26. For waves typically created by the wave generator, the timescales are in the order of 10^4 s, which is well outside the lifetimes of waves in our setup. For the converted waves, however, if the wavenumbers are too large, the viscous decay of the wave amplitude might make it more challenging to record these waves.

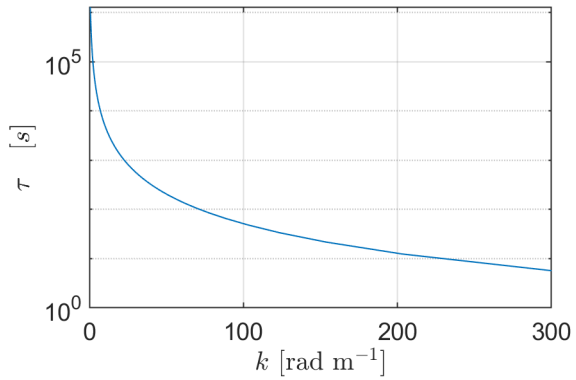

Figure 26: Characteristic decay timescale of wave amplitude dampening by viscosity, given by Eq. (65), showing that the characteristic timescale of amplitude decay by viscosity is shorter for larger wavenumbers.

3 Experimental setup and data processing

In these sections, the experimental setup that has been constructed in this work is presented and discussed. Versatility was taken into account in many design choices such that the resulting setup will be a general testbed for many possible analogue gravity experiments. An overview of the experimental setup is given in Fig. 27.

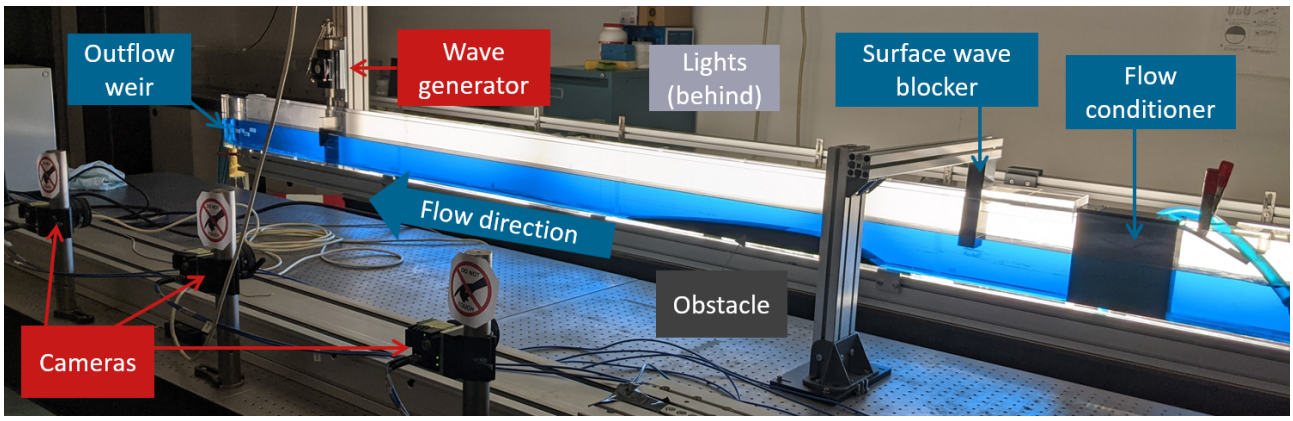

Figure 27: Overview of the experimental setup. A pump (not visible) generates an open channel water flow in a long and narrow tank, referred to as the wave flume. The flow is laminarised by the flow conditioner and any remaining surface fluctuations are blocked by the surface wave blocker. The height of the flow is controlled by the outflow weir. Waves are created by the wave generator: a vertically oscillating plunger, and propagate against the flow through the wave flume, where an obstacle can be placed that modulates the water height. Lights are placed behind the setup to illuminate the water and multiple cameras, placed off to the side of the flume, record videos of the propagating waves.

3.1 Wave flume

The main structure of the experimental setup is the wave flume, which is a 4 m long perspex tank with rectangular cross section, forming an open channel with 70 mm width. Subtracting the inlet, flow conditioner, and wavemaker, leaves a total measurable range of about 2.5 m. The shape of the wave flume was inspired by experiments in Refs. [4, 8].

A weir, shown in Fig. 28, controls the water level at the outflow, up to 20 cm (the height of the sidewalls). However, to avoid water spilling over the sides of the flume, the water level (plus any wave amplitude) is kept well below the maximum height.

The water flows over the weir and falls into a reservoir from which it is recirculated using a variable flow rate pump, which pumps the water into a hose towards the inlet side of the wave flume. The pump (AquaForte DM Vario S 20000) can be varied in power from 30% to 100%. With the addition of an overflow valve, the flow towards the wave flume can be reduced, giving full 0% to 100% flow control. The maximum volume flux that can be generated in the setup is 50 L min^{-1}. The flow rate is measured with an inline flow meter to 1 % relative accuracy.

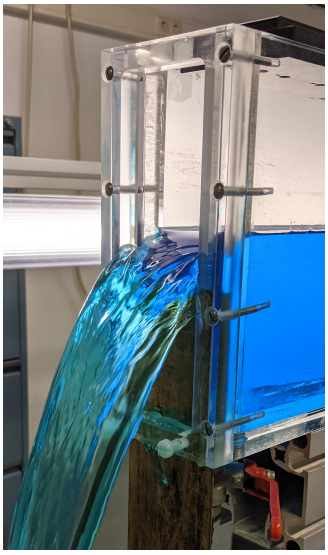

Figure 28: The outflow weir, consisting of a copper plate which can slide vertically to modulate the water level in the wave flume.

3.2 Flow conditioning

At the inlet side of the wave flume, where the water exits the hose originating from the pump, turbulence is generated, which will interfere with the measurements, and should therefore be reduced. At the end of the hose, an expanding nozzle is attached to spread out the jet. To further reduce turbulent fluctuations, the water is passed through a flow conditioner consisting of vertical plates. Fig. 29 shows a schematic of the flow conditioner. As water passes through the conditioner, the confinement between the plates causes the characteristic length scale to decrease drastically, reducing turbulence and eliminating larger eddies. Additionally, the conditioner straightens the flow over the flume width, as a faster-flowing channel in the conditioner is naturally slowed down due to the increased pressure difference over that specific channel.

There are some considerations in designing such a conditioner: if the spaces between the plates are too large, the turbulence reduction is insufficient. If the spaces are too small, the pressure difference over the conditioner will lead to a large water height difference, which might cause the water to spill over the flume walls. The length of the flow conditioner should allow for the full development of the flow profile between the plates. The length of flow development, known as the entrance length, is commonly given by a rule of thumb length of 20 to 30 times the distance between the plates. [15]

The walls between the channels should be thin, but not deform. If the walls are too thick, the water speed in the flow conditioner increases, decreasing the effectiveness of turbulence reduction. The water height difference over the flow conditioner can be predicted by assuming a plane Poisseuille flow profile between the plates, as plotted in Fig. 30. For the flow profile between the plates holds [16]

$$Q = \frac{d_{\text{channel}}^3 \Delta P}{12 \mu L} \,. \tag{66}$$

Given a pump flow rate, the pressure difference ΔP over the conditioner can be predicted as

$$\Delta P = -\frac{12 \mu L (d_{\text{wall}} + d_{\text{channel}}) Q}{W h d_{\text{channel}}^3} \,, \tag{67}$$

where μ is the dynamical viscosity, L the streamwise length, d_{wall} the wall (or plate) thickness, d_{channel} the width of the channels between plates, Q the flow rate, W the flume width and h the mean water

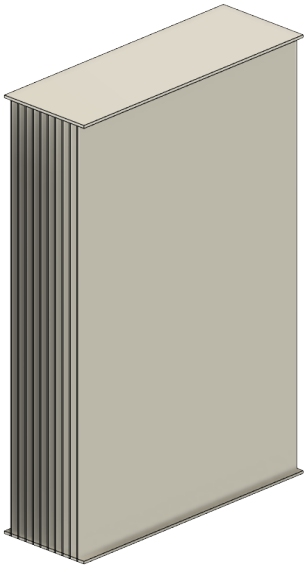

Figure 29: Model of the flow conditioner used to limit inflow turbulence. The flow conditioner consists of many plates which reduce the characteristic length scale of the flow, reducing turbulence.

height, see Fig. 30 for a diagram showing the geometric parameters. The pressure drop can be related to the water level drop using the hydrostatic condition

$$\Delta H = \frac{\Delta P}{\rho g} \,. \tag{68}$$

The flow conditioner used in the setup has length 20 cm, and height 30 cm. There are 10 walls with 1 mm thickness, that form 11 channels, 5.5 mm wide. These parameters lead to a typical expected height difference of 1 mm, which is much lower than necessary to prevent overflow. A typical height difference of 2 mm is measured in the laboratory. In the future, more plates could be used, since this will decrease the distance between the plates even further, making the flow conditioner more effective.

The effectiveness of such a flow conditioner can be increased by also including horizontal plates. However, because of the water level drop over the conditioner, the outflow of the higher channels can be above the water level and cause a small waterfall, which generates new fluctuations.

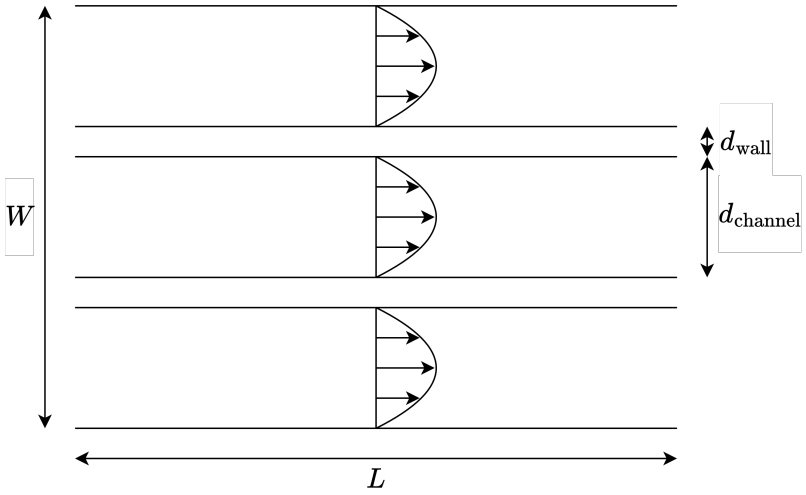

Figure 30: Top view schematic of the flow conditioner. Note that the actual flow conditioner has many more channels.

3.3 Wave generation

Waves are generated by vertically oscillating a plunger into the water; see Fig. 31. The wave generator consists of a linear motor plus control hardware, driving a metal rod with a plunger attached to its end. Usually, in wave flume experiments, the waves are generated by a horizontally oscillating plate. This technique indeed generates more accurately sinusoidally shaped waves, but this technique is difficult to combine with the background flow present in our experiments. Furthermore, the plunger method allows waves to be generated anywhere along the wave flume, in any direction, so the experimental focus can be shifted to upstream or downstream propagating waves.

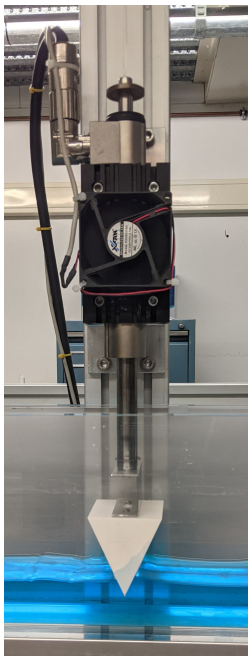

Figure 31: Wave generator consisting of a 3D printed plunger connected to a linear motor which oscillates the plunger vertically.

The linear motor (LinMot PS01-37x120F-HP-C driven by LinMot C1100-GP-XC-0S-000) that drives the plunger is supplied with a list of commands consisting of setpoints. The motor has a built-in PID controller that allows the motor to track the setpoint list provided very closely. The tracking is monitored using a digital oscilloscope, where the setpoints and measured position from an encoder are plotted; see Fig. 32. The oscillation amplitude, frequency, and profile of the plunger oscillation can be freely varied. If an experiment calls for it, a second wave generator can be easily added to the setup.

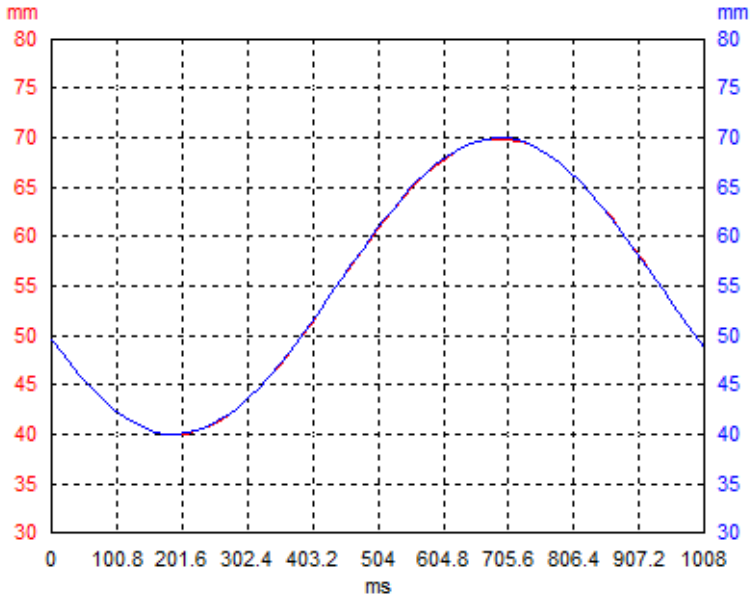

Figure 32: Wave generator oscilloscope snapshot showing the demanded position of the linear motor in red and the actual position in blue. The linear motor driving the wave generator tracks the demanded position very closely.

The dynamics of plunger wave generation in a background flow are not straightforward, and the theory on plunger wave generation including flow is limited. [17, 18] While the plunger moves into the water, the plunger displaces water but also forms a flow restriction that leads to a water level difference over the wave generator. The two mechanisms, displacement and constriction, both play a role in the wave generation. The combination of both mechanisms makes it challenging to create perfect sinusoidal water waves. For example, at higher oscillating frequencies, the velocity of the plunger with respect to the background flow is higher, and the displacement effects will be larger. When the speed of oscillation is too high, immediate wave breaking occurs: water is pushed upstream and upward, and the surface is breached; see Fig. 33 for a picture of this behaviour.

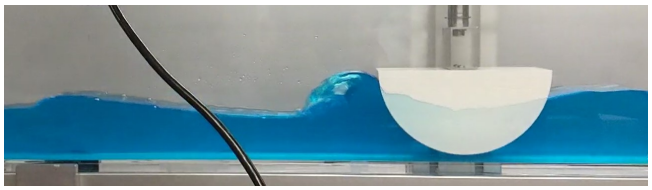

Figure 33: Wave breaking at the wave generator. The downward-moving plunger displaces too much water in a short period, forcing some water to break the surface. This wave breaking leads to extra fluctuations and must be avoided.

The simplest possible plunger shape is a plate, which only creates waves by blocking and unblocking the water. This shape, however, is ineffective at low flow rates or at larger oscillation frequencies, as

very little water would have accumulated during an oscillation cycle. A rectangular plunger, one more dimension than a plate, will displace some water. However, the water displacement is too abrupt when the plunger breaches the surface, but relatively minor when the plunger stays submerged. Therefore, a triangular shape was chosen (see Fig. 34) as it blocks the water and also displaces the water sideways, making it a versatile plunger. The asymmetry was chosen because we only want to create waves in a single direction. The angle of the diagonal slope of the plunger can not be too steep, or the displaced water is forced upward too fast and breaches the surface. The plunger fits in the width of the wave flume such that the generated waves are uniform in the channel width.

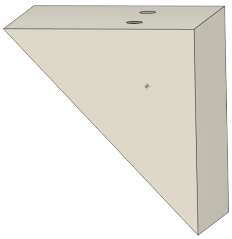

Figure 34: Model of the plunger used in wave generation. The plunger is 70 mm wide, which is the same width as the wave flume, 75 mm high and the angled side makes a 43° angle with respect to the vertical side.

After the waves are created, the waves might reflect off the wave flume ends and other obstacles. On the inflow side of the wave flume, a sponge slope is placed, which acts as a rudimentary wave absorber. In addition, the turbulence that the water inflow tube generates helps with wave absorption. Wave reflections are not observed on the outflow side, where the water flows over the weir into the reservoir. In the context of measuring converted waves near a white hole horizon, wave reflections may not be an issue, as the reflected waves are easily recognisable and can be filtered out.

Outside of the generated waves, there is a time-average flow constriction by the plunger: the average water level upstream of the wave generator is higher than a reference case without waves.

3.4 Cameras

To record the surface waves, 3 cameras (JAI SP-5000M-CXP2) are placed side-by-side, 65 cm apart, facing perpendicular to one of the sidewalls of the wave flume, at 130 cm distance to the wave flume. The cameras are equipped with Nikon AF Nikkor 20mm f/2.8D lenses that give an approximate field of view of 80 cm wide at the wave flume, or 35°. The resulting camera views contain a small overlap, which aids in the stitching of the recorded frames. After stitching, the total width of the camera view is 2.1 m.

The cameras have a sensor resolution of 2560 x 2048 pixels, which is vertically cropped to reduce unnecessary data transfer. The cameras record 8-bit monochrome images at up to 500 frames per second, but it was found that a sampling rate of 60 frames per second is sufficient to temporally resolve the wave dynamics in the setup (see Section 4.5). The exposure time is set to 1000 µs, which is long enough for proper exposure and short enough to prevent motion blur. Sensor gain is kept at the lowest setting to minimise sensor noise. Any automatic capabilities, such as autofocus and auto-exposure, are disabled. A computer containing storage drives with sufficiently high writing speed is necessary for recording (≈ 0.6 GB/s). The cameras are triggered centrally, so the frames are recorded synchronously.

3.5 Lighting

For useful images of the propagating waves, a good lighting system is necessary. The lighting should be bright (allowing for short exposures) and reasonably homogeneous, that is, there should only be a small difference between bright and dark spots. Fig. 35 shows the lighting setup used in this experiment.

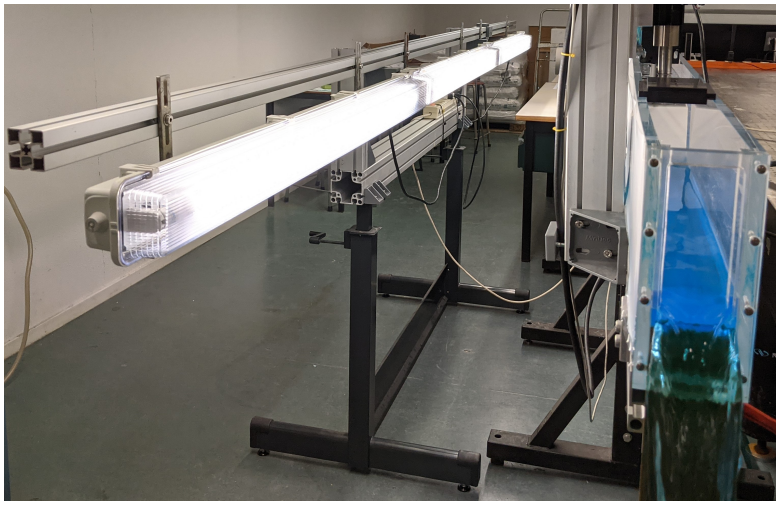

Figure 35: Lighting setup which provides a homogeneous illumination on the back of the flume.

The flume is backlit for high contrast between water and air, and the water is dyed with blue dye. Because of high-speed imaging and relatively short exposure times, bright and non-flickering lights are necessary. In this setup, 3 Philips Master LEDtube 1200mm HO 12.5-36W 840 T8 LEDs are used, which emit 2100 lm each. The tube-shaped LEDs are enclosed with diffusive covers and mounted to a structure placed 50 cm behind the flume (from the cameras' perspective). The distance between the flume and the lights (50 cm) allows for more homogeneous illumination. Additionally, a layer of semi-transparent plastic is placed on one of the sidewalls of the flume, on the side of the lighting, to further homogenise the illumination. This lighting setup, together with the dye, gives a strong contrast between air (bright) and water (dark) in the recorded movie frames.

3.6 Camera calibration

The images recorded by the cameras represent a projection of the real world onto the camera sensor. This projection contains effects such as perspective, lens distortion, and the 3D locations of the cameras and the wave flume in the lab. In order to relate locations within the measured images (in pixel coordinates) to a more meaningful, real-world location, a transformation is necessary. If the projection transformation from points in the real world to the sensor is understood, this can be inverted, to obtain the camera sensor to real-world location mapping.

The camera system is modelled with the ideal pinhole model. [19] The pinhole camera model is valid for lenses with a moderate field of view. For large-angle or fisheye lenses, a more sophisticated model is necessary. The field of view of the camera-lens combinations used in this work is 35°.

A point in 3D space, denoted by the coordinates $\mathbf{X} = (X, Y, Z)$ is projected on the sensor with coordinates $\mathbf{x} = (x, y)$. This projection can be considered in 2 steps, a 3D rigid transformation from arbitrary world coordinates to a coordinate system with the camera at the origin: $\mathbf{X_c} = (X_c, Y_c, Z_c)$, and secondly, a 3D to 2D projection of the image point onto the camera sensor. A chart of this process is shown in Fig. 36.

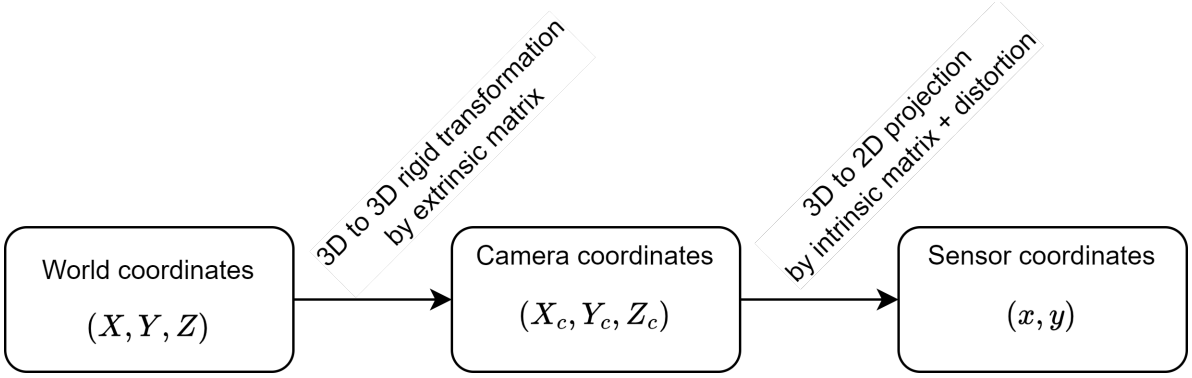

Figure 36: Camera transformation flowchart showing an outline of the camera transformation process.

The complete transformation from $\mathbf{X}$ to $\mathbf{x}$ is described by

$$\begin{pmatrix} x \\ y \\ 1 \end{pmatrix} = k \begin{pmatrix} R & t \end{pmatrix} \begin{pmatrix} X \\ Y \\ Z \\ 1 \end{pmatrix}, \tag{69}$$

where R is a 3×3 rotation matrix and t a translation vector, which together form the so-called extrinsic matrix which describes the 3D to 3D transformation from arbitrary world coordinates to camera coordinates, and

$$k = \begin{pmatrix} f_x & s & c_x \\ 0 & f_y & c_y \\ 0 & 0 & 1 \end{pmatrix} \tag{70}$$

is the intrinsic matrix that describes the 3D to 2D projection from camera coordinates to sensor coordinates, displayed in Fig. 37. f_x and f_y are the focal lengths, which are normalised with the pixel size: $f_x = \frac{F}{P_x}$. c_x and c_y place the origin of the sensor coordinates and s models the skew of the camera pixels, which is zero in most cameras.

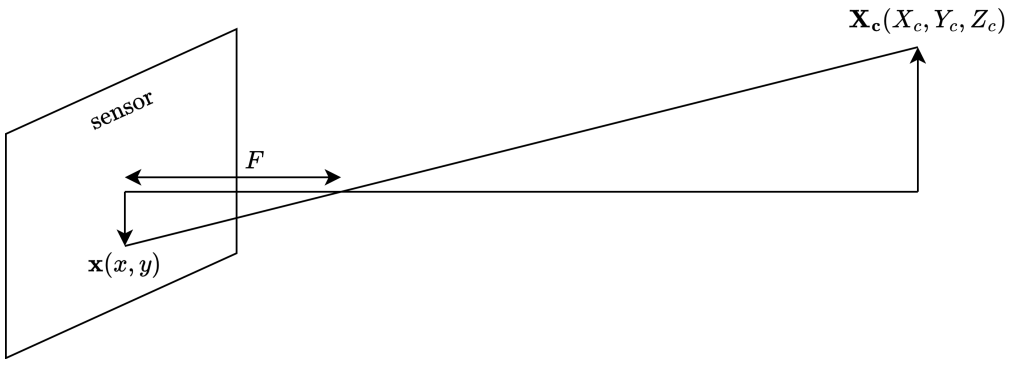

Figure 37: 3D to 2D projection of a point in the camera coordinate system ($\mathbf{X_c}$) to a point on the sensor ($\mathbf{x}$). F is the focal length, which determines the zoom of the camera system.

The extrinsic and intrinsic matrices together form a general transformation matrix $A = k \begin{pmatrix} R & t \end{pmatrix}$. The origin of the arbitrary world coordinate system can be placed anywhere, so we can choose $Z = 0$ to be

at the wave flume. With this choice, the transformation system for points at the wave flume becomes

$$\begin{pmatrix} x \\ y \\ 1 \end{pmatrix} = A \begin{pmatrix} X \\ Y \\ 0 \\ 1 \end{pmatrix} , \tag{71}$$

which can be reduced to

$$\begin{pmatrix} x \\ y \\ 1 \end{pmatrix} = A' \begin{pmatrix} X \\ Y \\ 1 \end{pmatrix} \tag{72}$$

by dropping the third column from A. Now, A' is a square matrix, and the system can be inverted to obtain a mapping from the sensor to the laboratory coordinates.

The distortion from the camera system is not included in the ideal pinhole camera model and is separately modelled as

$$x_{\text{dist}} = x(1 + k_1 r^2 + k_2 r^4) \tag{73}$$

$$y_{\text{dist}} = y(1 + k_1 r^2 + k_2 r^4) \tag{74}$$

$$r^2 = x^2 + y^2 \,, \tag{75}$$

where $(x_{\text{dist}},\ y_{\text{dist}})$ are the distorted coordinates of true, undistorted pixel coordinates (x, y). The effect of distortion is visualised in Fig. 38. In general, lens distortion is more severe on the outside of an image. The camera sensor used ($1''$ CMOS) is much smaller than the full-frame sensors that the lens can cover; therefore, the camera distortion is relatively minor, still the inverse of Eq. (73) can be used to correct for any distortion.

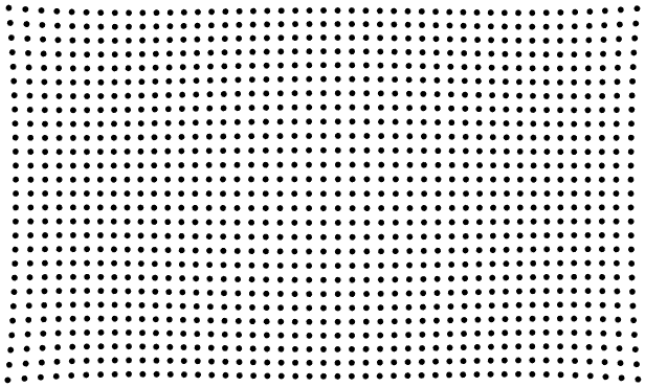

Figure 38: Visualisation of lens distortion. The illustration shows the (virtual) image of a grid of evenly spaced dots. The effects of distortion are the strongest around the image edges.

To obtain the intrinsic matrix and distortion parameters of the camera system used in the setup $(k,\ k_1,\ k_2)$, a chequerboard calibration target (shown in Fig. 39) is imaged at many different positions and orientations. It is vital that the chequerboard target is flat. From the images, the chequerboard corners are detected, and since the real-world dimensions of the chequerboard are accurately known, the orientation and distance of the chequerboard can be estimated. Then, a so-called reprojection error is calculated, which is the total mismatch between the observed chequerboard corners and the expected corner coordinates using the current estimate of the camera parameters. The total reprojection error across all recordings is minimised by iteratively updating the camera model parameters. [20, 21]

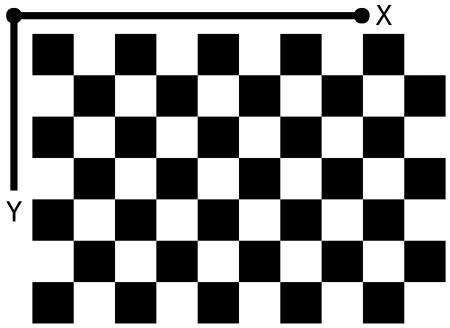

Figure 39: Chequerboard pattern used as calibration target in camera calibrations.

To obtain the extrinsic parameters $\begin{pmatrix} R & t \end{pmatrix}$, the chequerboard target is positioned at the wave flume, parallel to the sidewall and the bottom. Knowing the intrinsic parameters of the camera, the dimensions of the checkerboard, and that the checkerboard is located at $Z = 0$, a transformation can be calculated from the camera coordinate system ($\mathbf{X_c}$) to the world coordinate system ($\mathbf{X}$).

At this point, a transformation has been established from each camera's sensor to a 2D slice in world coordinates, which is placed exactly at the flume. However, the world coordinate systems of each camera still need to be unified into a unique world coordinate system. By adding an additional translation t_0 to the translation vectors t, one can choose where the laboratory coordinate system's origin is located. The correct t_0 for each camera can be determined by placing a chequerboard target in the overlap region of a camera pair and optimising t_0 such that the chequerboard overlap accuracy is maximised. The vertical origin is chosen at the bottom of the flume.

In the end, a mapping is established between any pixel coordinate of any camera sensor to a unique coordinate system at the wave flume, allowing the transformation of pixel coordinates in recorded images to real-world positions along the wave flume. After the coordinate transformation, each recorded pixel corresponds to a 0.311 mm x 0.311 mm square in laboratory coordinates.

3.7 Interface extraction

Movies of the water waves are recorded as a series of monochrome images, or frames. See Fig. 40 for a typical recording snapshot, in which the frames from the 3 cameras have been combined, using the method discussed in the previous section.

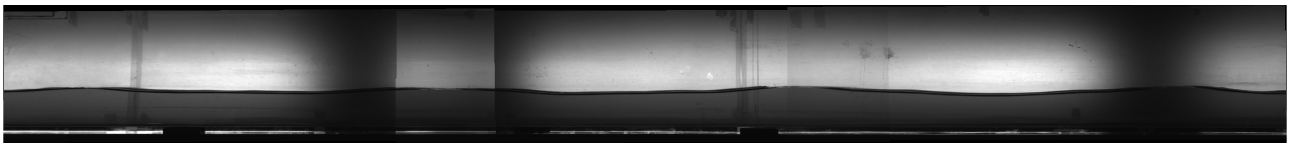

Figure 40: Stitched camera frames.

The pixel values in the recorded frames are divided by the pixel values of a reference image of the setup without water, see Fig. 41. This greatly reduces inhomogeneities in background lighting and imperfections on the wave flume walls (stains, scratches, etc.).

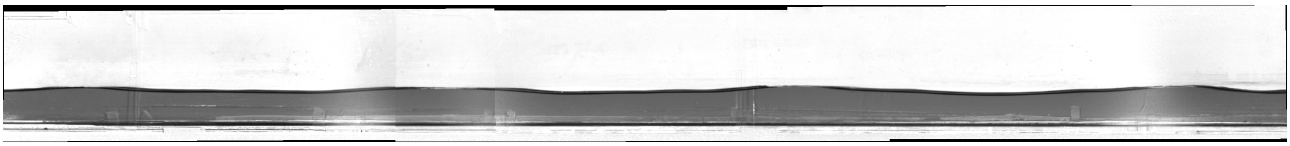

Figure 41: Normalised stitched camera frames obtained by dividing the recorded pixel value by a reference image of the setup without water. The image shows a great contrast between air and water.

The frame is binarised, that is, all pixel brightness values below a threshold are set to 0 and those above the threshold are set to 1. This is possible because of the excellent contrast between the air (bright) and water (dark). Any holes or islands (small, fully enclosed regions) in the binary maps are filled. The resulting binary map is displayed in Fig. 42. Adaptive binarisation schemes are available that recalculate the binarization threshold based on a neighbourhood. Still, in this case, the lighting of the whole composite image was uniform after normalisation, which makes single-threshold binarization possible.

Figure 42: Binarised stitched camera frames.

The binarization scheme leaves an image with two regions from which the water-air boundary is extracted. In Fig. 43, the extracted boundary is overlayed on the normalised frame, with a 10x zoom.

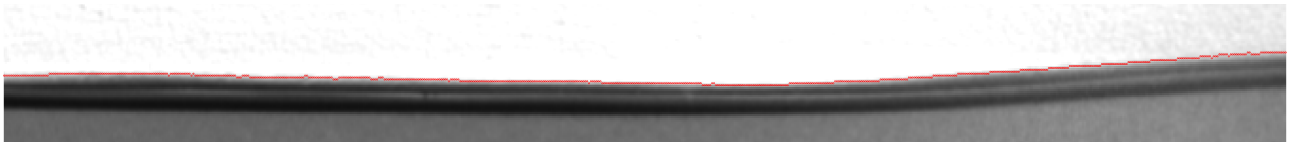

Figure 43: 10x zoom of the normalised frame, showing the extracted boundary (red line).

Since the waves are of small amplitude and breaking is not (supposed to) be present in the setup, each horizontal coordinate only contains one air-water boundary. Using the transformations from Section 3.6, the found pixel coordinates are related to the laboratory coordinates.

3.8 Spectral analysis

Since we are dealing with waves, which are periodic in space and time, it is natural to discuss the waves in terms of spectral properties. The Fourier transform

$$F(k) = \int_{-\infty}^{\infty} f(x) \exp(-2\pi i k x)\, \mathrm{d}x \ , \tag{76}$$

describes the spectrum of a function $f(x)$, i.e., the strength of different frequencies present in the signal. Numerically, the Fourier transform is carried out using the Fast Fourier Transform algorithm (FFT), which is an algorithm that calculates the discrete Fourier transform

$$F_{k+1} = \sum_{j=0}^{n-1} x_{j+1} \exp\left(-\frac{2\pi i k j}{n}\right), \tag{77}$$

where j and k run from 0 to $n-1$. For the temporal spectrum, the resolution and range of the spectrum depend on the sampling frequency f_s, which is set by the frame rate of the camera, and the recording length T. The highest frequency that can be resolved is $\frac{f_s}{2}$ and the resolution of the spectrum is $df = \frac{f_s}{T}$. For the spatial component, the sampling frequency is the number of pixels per unit of distance and the recording length is the pixel width of the recordings. This gives a highest resolvable wavenumber (the spatial counterpart to the frequency) of $\frac{k_s}{2}$, with a resolution of $dk = \frac{k_s}{L}$.

4 Results and discussion

4.1 Background flow

As a first verification of the newly constructed setup, standing water is recorded at different heights, which should result in flat water interfaces throughout the wave flume. In Fig. 44a, recorded stationary water levels are displayed. Note that the scaling of the horizontal axis is much larger than that of the vertical axis. The extracted water profiles are indeed flat along the entire domain, with deviations of the order of pixels, possibly caused by water-wall interactions that are discussed in Section 4.11.

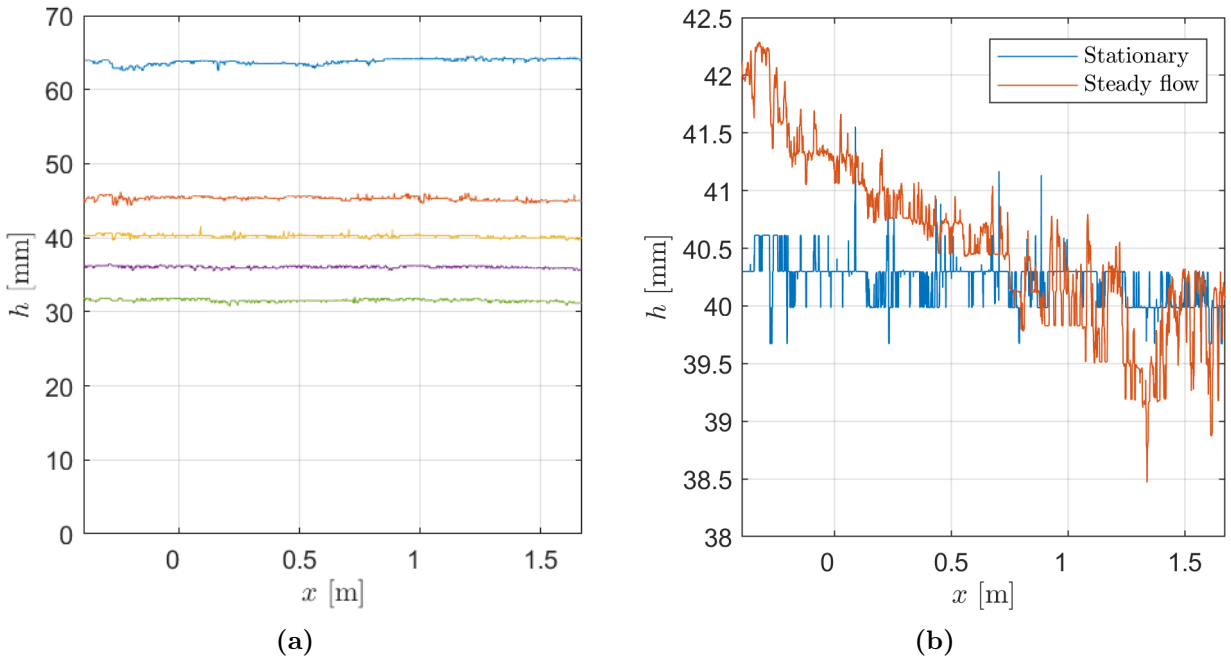

(a) **(b)**

Figure 44: (a): Still water levels at different heights. Note that the horizontal and vertical axis have a different scaling. **(b)**: Stationary water height compared to steady-flowing water profile, showing an approximate 2 mm water level drop. The water is flowing in the positive x-direction.

The next step is steady-flowing water. From the theory discussed in Section 2.3.1, the water level is expected to drop slightly as the water flows through the wave flume, following Eq. (42). A steady-flowing water level was recorded for a 10 s period, at 24 frames per second. Fig. 44b shows the time-averaged but space-dependent water height, compared to a stationary water profile of similar height. Indeed, the expected water level drop is observed.

The length of a pixel is 0.311 mm, which gives the lower bound on the measurement error of the extracted height profiles. Random errors, like fluctuations in the flow, can be minimised by taking measurements over longer periods and averaging them, as the background flows are (intentionally) time-independent. Additionally, because this work primarily examines waves and their spectral characteristics, the Fourier transform remains effective despite random errors. Random errors are also significantly reduced by fitting the data.

The steady-flowing measurement is extended: Fig. 45a shows various water profiles from a measurement series where the flow rate was kept constant at $q = 0.012\,\mathrm{m^2\,s^{-1}}$, but the water height at the outflow was varied. The slope of the water level is obtained using a linear fit and is displayed in Fig. 45b, together with the theoretical curve for a constant friction coefficient $C_D = 0.004$, given by Eq. (43),

and the flow parameters measured in the setup. The friction coefficient is a dimensionless quantity in the momentum conservation Eq. (28), which relates the loss of momentum to the squared velocity of the flow. The values of the drag coefficient in rivers range between 0.003 and 0.02 [9], indicating that our setup behaves as a very smooth river.

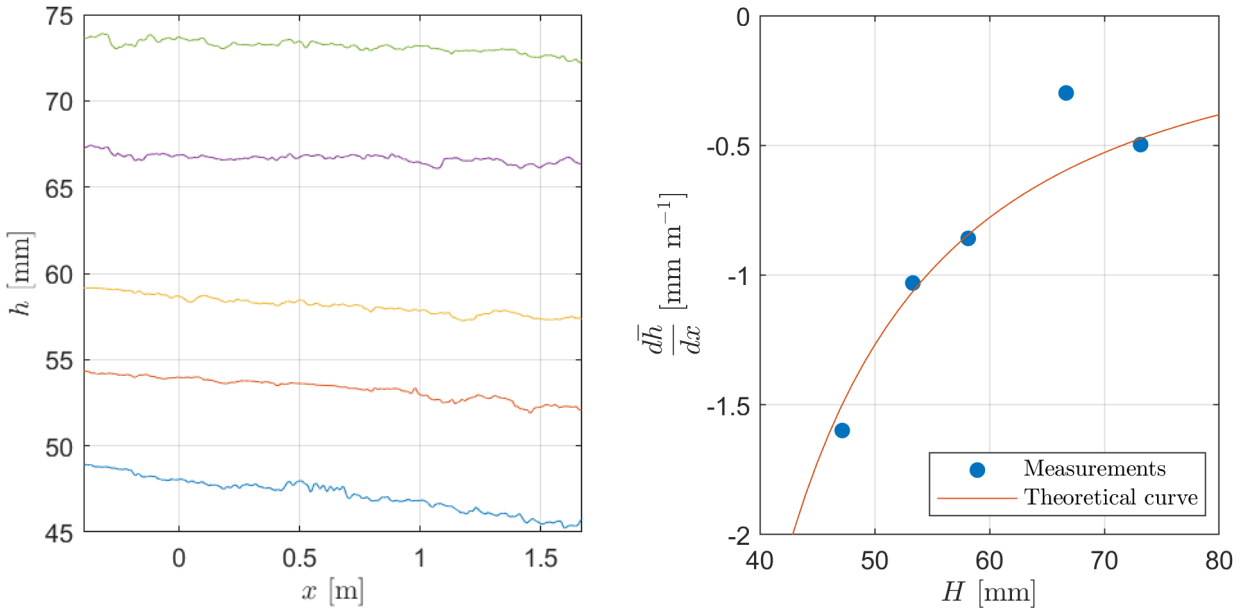

(a) **(b)**

Figure 45: (a): Time-averaged water profiles of a steady flow with flow rate $q = 0.012\,\mathrm{m}^2\,\mathrm{s}^{-1}$. The different profiles are obtained by varying the height of the outflow weir. Remark the similarity with the theoretical prediction by Eq. (42), shown in Fig. 6b, lower mean water levels indeed show a larger slope, at constant flow rates. **(b)**: Slope of the water profiles shown in (a) as a function of the space-averaged height H, together with the theoretical prediction, Eq. (43), for a friction coefficient $C_D = 0.004$. One slope value deviates from the curve of constant C_D, for an unknown reason.

Overall, the experimental setup successfully extracts the water interface and determines the water level drop in steady flows. The behaviour of steady-flowing water profiles aligns with the theoretical predictions presented in Section 2.3.1. The connection between the slope of steady-flowing water and the mean water height adheres to the theoretical curve where the friction coefficient remains constant. However, to determine the friction coefficient of the setup with greater precision, additional measurements are required.

4.2 Wave generation

In Section 3.3, the wave generation setup is presented and the behaviour of the oscillating plunger is discussed qualitatively. This section aims to measure some of the wave generation effects.

First, the effect of static flow constriction on the mean water height upstream of the wave generator is studied by holding the plunger at different heights, blocking part of the steady flow. A blocking height h_{block} is defined as the downward extension of the plunger into the water, with $h_{block} = 0$ when the tip of the plunger is at the water surface. The water level rise is compared with the reference height H_0, which corresponds to the water level without any blocking. The resulting water level rise is plotted in Fig. 46. Unsurprisingly, the static flow constriction increases the upstream water height, but the relation between blocking height and water level increase is not linear, as the water level change

increases drastically for blocking heights just over half the water height.

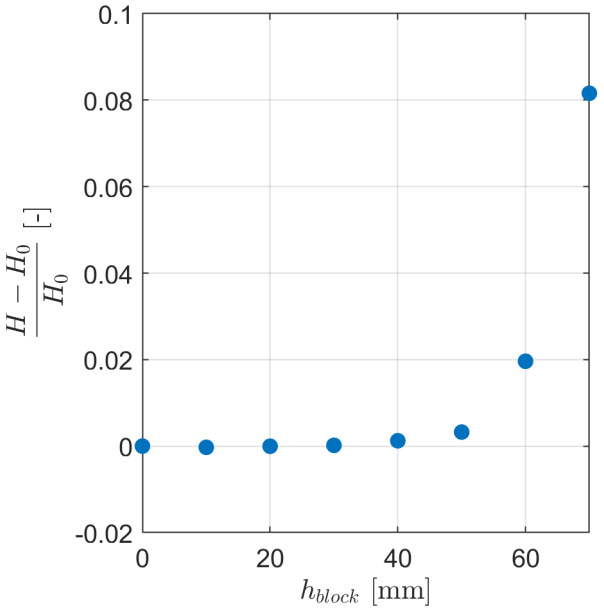

Figure 46: Effect of wave generator flow constriction on the space-averaged water level H for different static blocking heights h_{block}, defined as the downwards extension of the plunger into the flowing water. The flow rate was kept constant at $q = 0.010\,\mathrm{m^2\,s^{-1}}$, which gives reference (unblocked) flow with $H_0 = 87\,\mathrm{mm}$, $V = 0.11\,\mathrm{m\,s^{-1}}$. The water level rise as a result of wave blocking gets much stronger for static blocking height closer to the water height.

Moving on to wave generation. As discussed, the wavemaker oscillates up and down, blocking and unblocking the flow, which creates the waves. Fig. 47a shows how different wave generator frequencies generate waves with different amplitudes, for constant water height, speed and stroke length (defined as the distance between the highest and lowest point in the plunger oscillation). From the measurements, it is found that the generated waves have a larger amplitude for a larger frequency, which indicates that the sideways displacement is relevant in wave generation.

To investigate the influence of wave generation frequency on the effective blocking, the time-averaged water height increase upstream of the wave generator is measured for different oscillating frequencies and stroke lengths, the result is plotted in Fig. 47b. The time-averaged effect of the flow constriction by the oscillating wavemaker cannot be approximated by the constriction effect of a static wavemaker with a blocking height of half the stroke length, because the oscillation frequency influences the time-averaged flow constriction.

Lastly, it is investigated how long it takes for the system to regain equilibrium (i.e. for the system-average water height to settle) after the plunger is lowered into the water. We can find a simple estimate of the equilibration time as the time it takes for a shallow water wave to traverse the length of the wave flume, which should be

$$T = \frac{L}{\sqrt{gH_0} - V_0}\,, \tag{78}$$

where $L = 4\,\mathrm{m}$ is the length of the flume. For a reference flow with $H_0 = 87\,\mathrm{mm}$ and $V = 0.11\,\mathrm{m\,s^{-1}}$, the estimated equilibration time is $T = 4.9\,\mathrm{s}$. In Fig. 48, the increase in the system-average water height after quickly lowering the plunger is plotted. For an unknown reason, the final water level increase is higher compared to the static blocking measurement presented in Fig. 46.

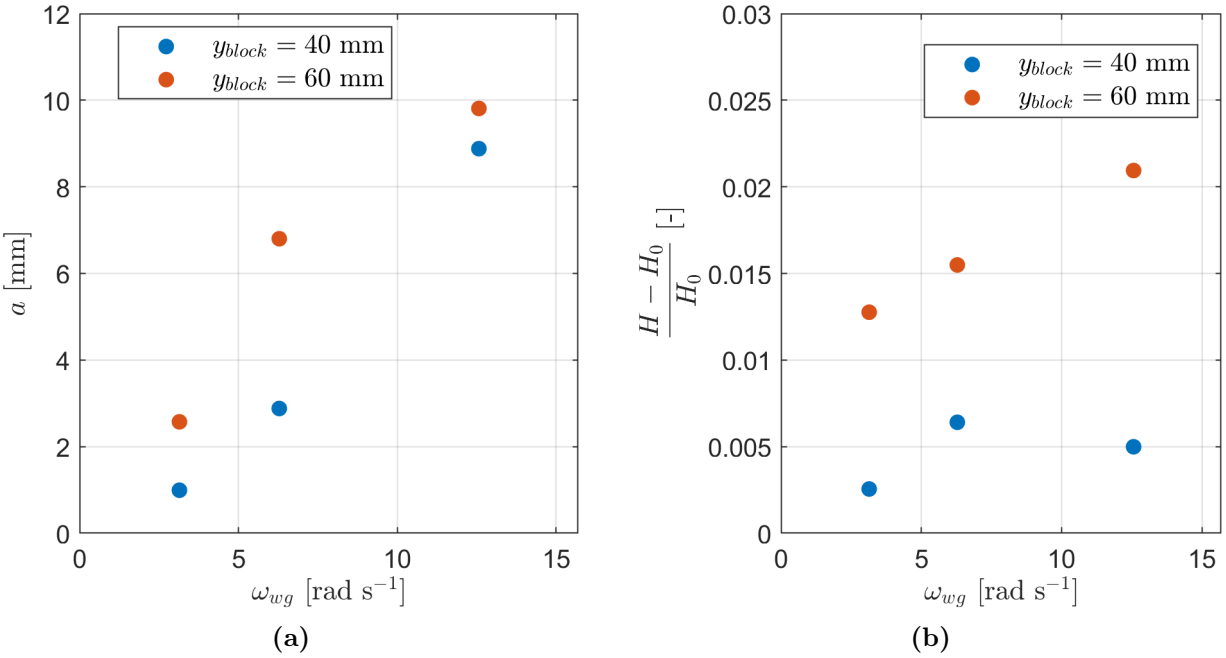

Figure 47: The background flow rate was $q = 0.010\,\mathrm{m^2\,s^{-1}}$, which gives a reference flow with $H_0 = 87\,\mathrm{mm}$, $V = 0.11\,\mathrm{m\,s^{-1}}$. Waves were generated by vertically oscillating the plunger between 0 to 40 mm or 60 mm blockage, at different oscillating frequencies ω_{wg}. **(a)**: Amplitude of the generated waves for different frequencies and blocking heights. **(b)**: Effect of wave generation on the time-averaged water height H.

Fig. 48 shows an initial rapid increase in water level, followed by a longer and slower increase in water level until the system settles. During the measurements, it was observed that, after the flow constriction was applied, a strong gravity wave travelled upstream, bounced back and the end of the flume, travelled downstream, bounced off the submerged plunger, and repeated this behaviour. The simple estimate for the equilibration time overestimates the initial water level rise timescale and severely underestimates the time it takes for the water level to settle. The slow rise in water height can be explained as follows: an increase in water height also increases the relative amount of flow constriction by the plunger, which leads to a further increase in water height, and so on.

In conclusion, depending on the type of experiment, different wave amplitudes and frequencies may be needed. For low-frequency, large-amplitude waves, a large blocking height is needed. In these cases, the effect of the wave generator on the mean flow properties should be taken into account. Furthermore, from these investigations, it is clear that many experimental parameters are co-dependent. This makes it challenging to perform a measurement series where only one parameter, say the wave generator frequency, is varied. The mean flow constriction of the wavemaker is found to depend on frequency (for relatively large stroke lengths), and therefore the weir heights must be adjusted during such a measurement series to keep the system-average water height constant. Furthermore, a change in the wavemaker frequency will lead to different amplitude waves, so the wavemaker stroke must be adapted as well. Lastly, every time any system parameters are changed, the system must be given ample time to re-equilibrate.

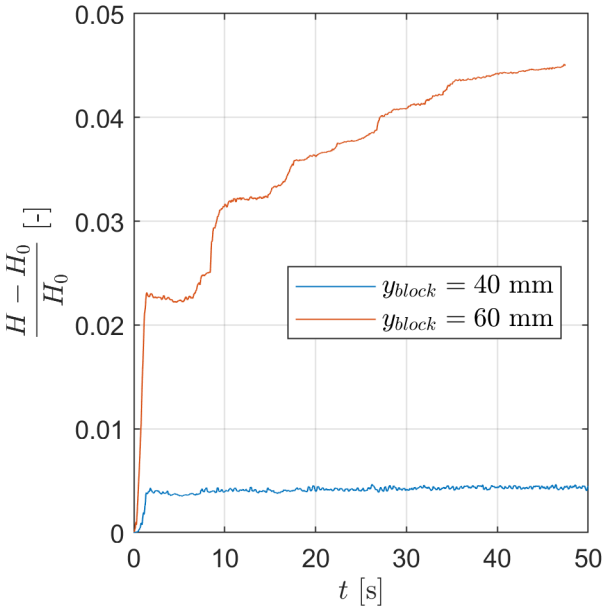

Figure 48: Water level rise over time after a flow constriction is applied to a steady flow. The flow rate was $q = 0.010\,\mathrm{m^2\,s^{-1}}$ with gives a reference (unblocked) flow with $H_0 = 87\,\mathrm{mm}$, $V = 0.11\,\mathrm{m\,s^{-1}}$. The plunger lowered to $y_{block} = 40\,\mathrm{mm}$ or $y_{block} = 60\,\mathrm{mm}$ while the water height in the setup was recorded. The blockage leads to an initially fast water level rise, followed by a long slow water level rise.

4.3 Wave dispersion relation

As discussed in Sections 2.4.1 and 2.4.2, the frequency and wavenumber of waves in the system are related via the so-called dispersion relation. In this section, the dispersion relation is measured from the generated waves in the setup, to further test the agreement between the constructed setup and the relevant theory.

The wave generator oscillates at a single frequency (ω_{wg}), creating waves that travel upstream (in the negative x direction) in the wave flume, in the absence of obstacles. The flow rate was $q = 0.0072\,\mathrm{m^2 s^{-1}}$, the water height $H = 60\,\mathrm{mm}$ and the velocity $V = 0.12\,\mathrm{m\,s^{-1}}$. The pump flow rate can be kept constant during the measurements, but it is difficult to control the mean water height and the mean background flow speed, since the interaction of the wave generator and the mean flow affects the steady state of the system, as discussed in Section 4.2. The total recorded time was five times the wave generator period, recorded at 24 frames per second.

Fig. 49a shows an instantaneous height profile of the generated waves. The generated waves are indeed periodic but deviate slightly from the shape of a perfect sinusoidal wave: the wave peaks are somewhat flattened and the wave troughs are too narrow. Fig. 49b shows the entire recording. This diagram is analogous to the spacetime diagrams often found in the context of general relativity. The colour represents the instantaneous water height change with respect to the time-average but space-dependent water height: $h - \overline{h}$. This representation corrects for the steady-state background flow level, like the water level drop discussed in Section 4.1.

As expected, the waves move with constant velocity through the system, which can be seen from the plot (Fig. 49b) as the points of constant height form straight lines in the diagram. The wavelength (horizontal distance between two points of equal height) does not change nor does the frequency (vertical distance between two points of equal height). The wave amplitude decays slightly as the

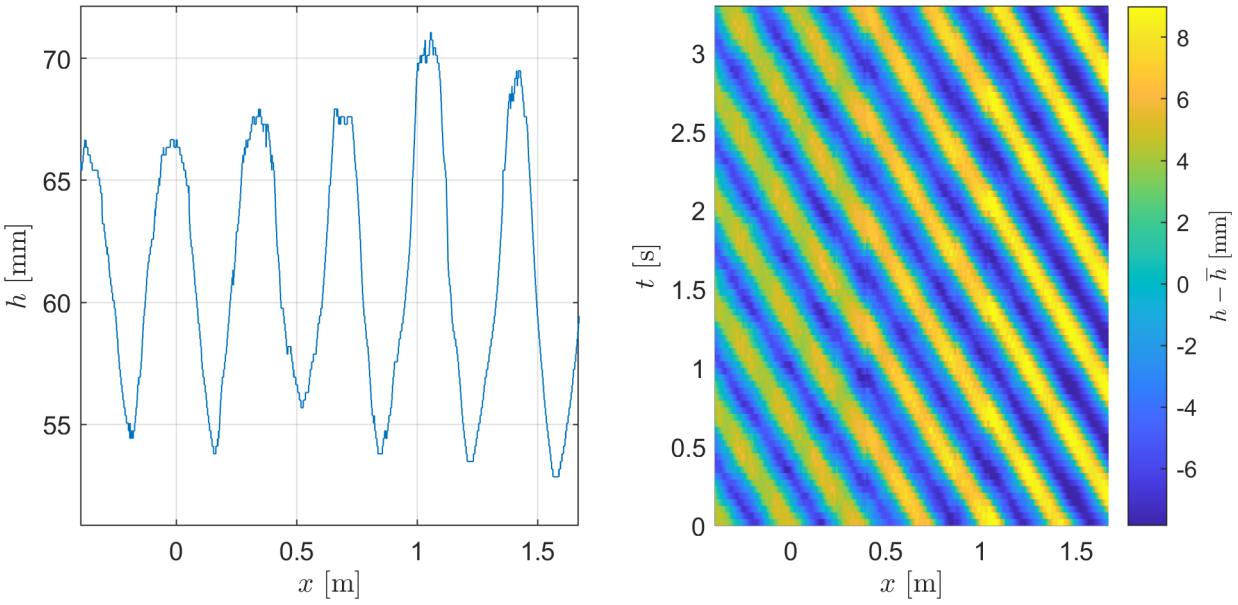

(a) Snapshot at $t = 0\,\mathrm{s}$ **(b)** Full recording

Figure 49: Recording of waves travelling upstream over a flat bottom. Experimental parameters were: $H = 60\,\mathrm{mm}$, $V = 0.12\,\mathrm{m\,s^{-1}}$, $\omega_{wg} = 9.4\,\mathrm{rad\,s^{-1}}$. **(a)**: Instantaneous height profile of the generated waves. The generated waves are periodic but show slight deviations from a perfect sinusoidal shape: the peaks of the waves are somewhat flattened, and the troughs are a bit too narrow. **(b)**: Entire recording of the waves travelling through the system. The colour gives the water height minus the time-averaged but space-dependent water level, to correct for the (small) slope in the background flow.

waves move upstream through the system. Small discontinuities are visible, which are a result of camera stitching.

The water profiles can be fitted using a sine function to obtain an accurate wavenumber and phase measurement. The fitting equation is

$$h(x) = a\sin(kx + \phi) + h_0\,, \tag{79}$$

where a is the wave amplitude, k is the wavenumber, ϕ is the phase and h_0 is the mean water height. Fitting the height profiles will reduce the random errors present in the water profiles. The fit is performed at every recording timestep, where the initial guess of the fit comes from the fitting results of the preceding timestep. In the end, the wavenumbers obtained for all timesteps are averaged, and the resulting wavenumbers are displayed in Fig. 50a, plotted for different wave generator frequencies and compared to the theoretical dispersion relation.

The phase velocity of the waves can be measured by computing the change in phase over time, which is done by performing a linear fit on the wave phases obtained from the sine fits. The phase velocity is then given by

$$c = \frac{1}{k}\frac{\mathrm{d}\phi}{\mathrm{d}t}\,, \tag{80}$$

and plotted in Fig. 50b compared with the theoretical phase velocity. The wavenumbers and phase velocities obtained from the fits show agreement with the theory, demonstrating that the setup, and in particular the water height acquisition methods, are correct up to finite accuracy.

Alternatively, we can use the spectral analysis tools (discussed in Section 3.8), to obtain the wavenum-

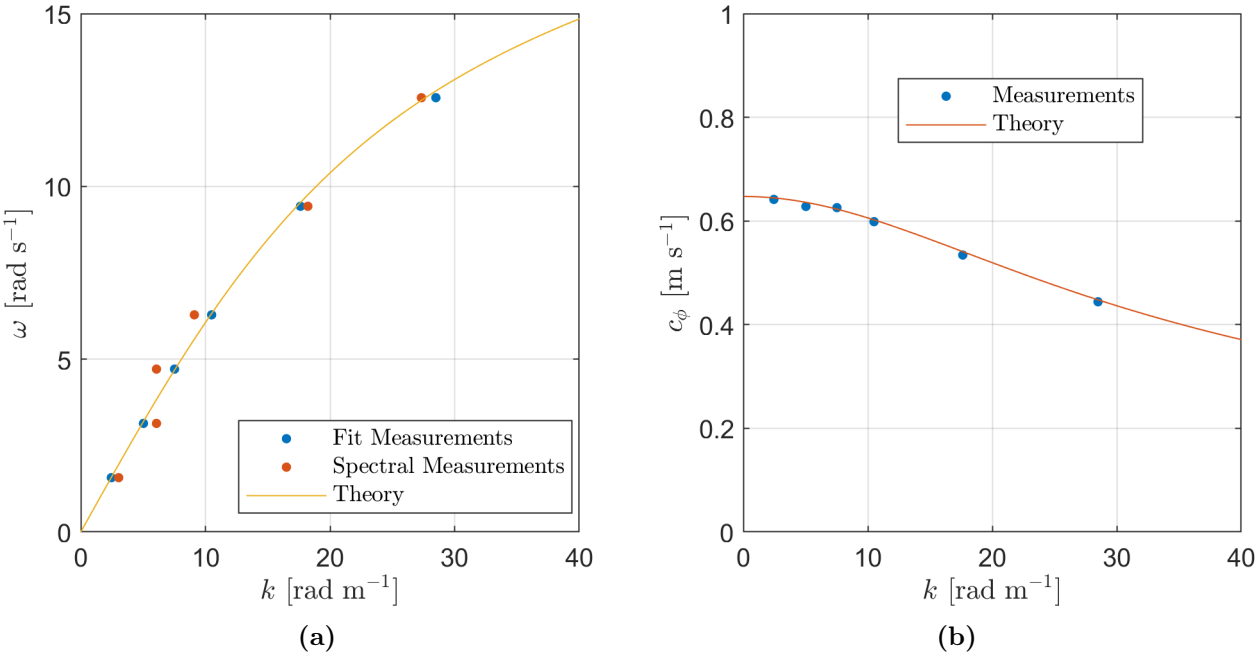

Figure 50: (a): Wavenumbers obtained by fitting a sine wave to the recorded water profiles of propagating waves, or obtained from the peaks in the spatial spectra, for different wave generator frequencies, compared to the theoretical dispersion relation Eq. (58). **(b)**: Measured phase velocity of recorded waves compared to the theoretical phase velocity Eq. (59).

ber of the generated waves. The temporal spectrum, plotted in Fig. 51a, peaks sharply at the frequency of wave generation, which should be the case. Additional peaks are present at multiples of the wave generator frequency. The spatial spectrum, plotted in Fig. 51b, is peaked at the wavenumber that is present the strongest. We can take the wavenumber where the peak occurs and plot the frequency-wavenumber pairs on the dispersion relation, which are included in Fig. 50a.

The spectral resolution is better for larger wavenumber and frequency since the waves repeat more times in the data. For this reason, we expect the measurement points from the spectra to be closer to the theoretical dispersion relation for larger wavenumbers.

In addition to the temporal and spatial Fourier transform, we can perform a 2D Fourier transform. The logarithm of the amplitudes resulting from such a 2D Fourier transform is plotted in Fig. 52. The most prominent peak (at $\omega = 9.4\,\mathrm{rad\,s^{-1}}$, $k = -18.2\,\mathrm{rad\,m^{-1}}$) corresponds to upstream waves ($c < 0$). Furthermore, the downstream branch of the general dispersion relation, caused by random water fluctuations, is faintly observable. Another peak at $\omega = 9.4\,\mathrm{rad\,s^{-1}}$ with the wavenumber corresponding to a downstream wave suggests the presence of a reflected wave. Higher harmonics are also visible at multiples of the wave generator frequency.

To conclude, the waves propagating upstream in the experiment and captured by the camera setup, after extracting the air-water interface profile and performing sinusoidal fitting to obtain the wavenumber, confirm that the waves adhere to the theoretical dispersion relation. This indicates that the setup is correctly constructed and calibrated. Furthermore, the wave profiles were analysed in the spectral domain, showing a pronounced peak at the wavenumber in the spatial spectrum, from which the wavenumber can be extracted. These wavenumbers also adhere to the theoretical dispersion relation, albeit with a lower spectral resolution at lower wavenumbers.

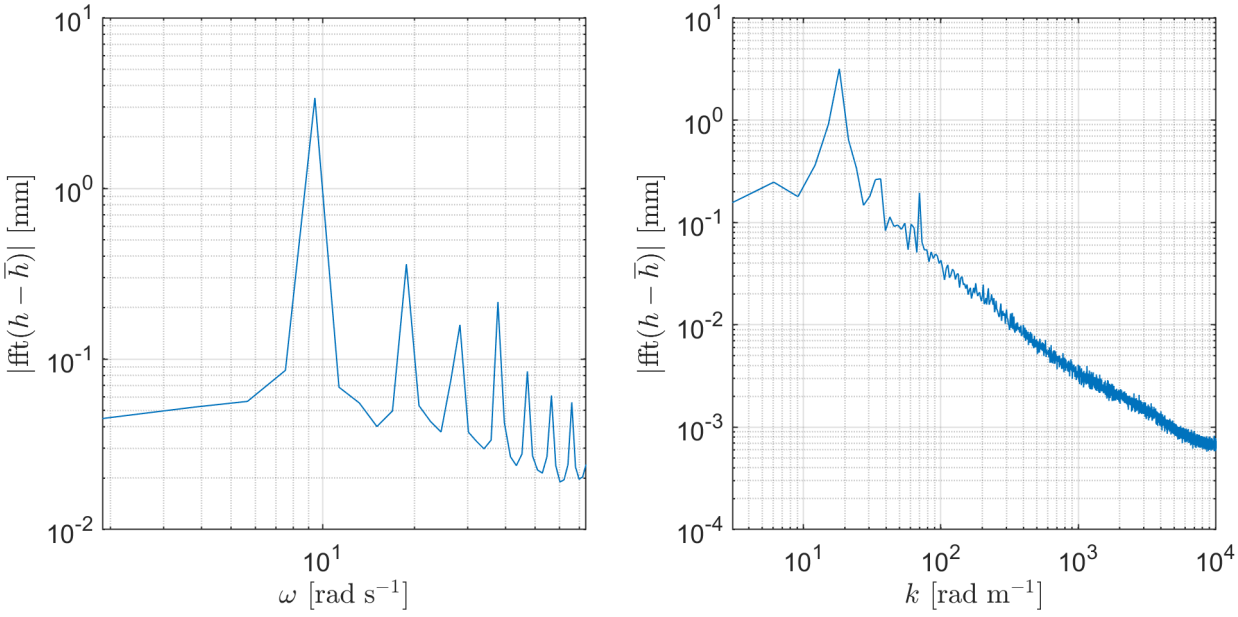

Figure 51: Spectra corresponding to the recording displayed in Fig. 49b. **(a)**: The temporal spectrum shows a strong peak at the frequency of wave generation, and extra peaks at multiples of the the wave generator frequencies. These extra peaks are knows as harmonics, and are present if the transformed signal is not a perfect sine. **(b)**: The spatial spectrum which peaks at the wavenumber of the waves present in the system.

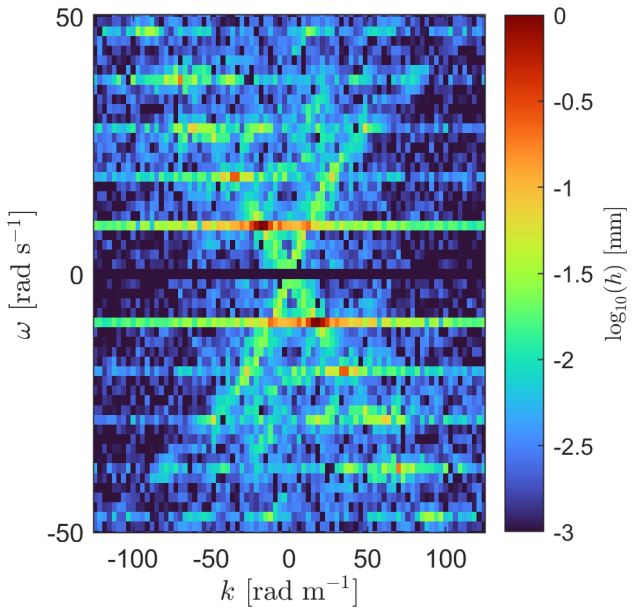

Figure 52: 2D spectrum of monochromatic waves travelling upstream over a flat bottom. The strongest peak (at $\omega = 9.4\,\mathrm{rad\,s^{-1}}$, $k = -18.2\,\mathrm{rad\,m^{-1}}$) corresponds to the upstream waves ($c < 0$). We can also faintly see the downstream branch of the general dispersion relation, which comes from random water fluctuations. There is another peak visible at $\omega = 9.4\,\mathrm{rad\,s^{-1}}$ with the wavenumber of a downstream wave, which could be a reflected wave. Also visible are the higher harmonics at multiples of the wave generator frequency.

4.4 Wave reflections

The waves that are propagating through the wave flume may reflect off obstacles. The reflection process can be understood using the dispersion relation. The dispersion relation in the laboratory frame,

$$(\omega - vk)^2 = gk \tanh(kh)\,, \tag{58}$$

describes both upstream and downstream wave propagation. In a reflection, the wave switches from the upstream curve to the downstream curve (or vice versa) in the dispersion relation, which is visualised in Fig. 53. The figure shows a wave travelling downstream with some wavenumber and frequency (yellow dot) that, when reflected, will switch to the other dispersion branch along the horizontal dotted line, to a wave (purple dot) with a lower wavenumber and opposite sign propagation velocity.

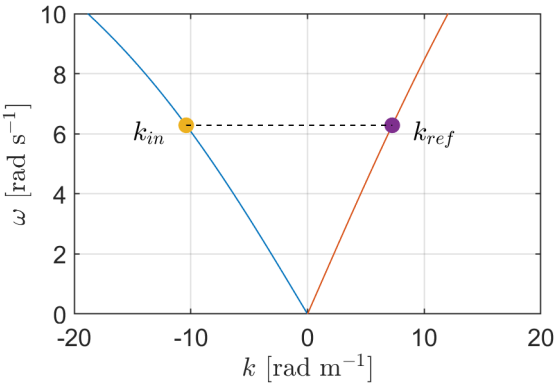

Figure 53: Schematic representation of a wave reflection. The red and blue curves show the downstream and upstream dispersion curves in the laboratory frame, respectively. A wave travelling downstream (yellow dot, k_{in}), when reflected, will switch to the other dispersion branch along the horizontal (equifrequent) dotted line, to a wave (purple dot, k_{ref}) with a lower wavenumber and opposite sign propagation velocity.

To confirm this behaviour, we can compare the theoretical prediction with a measurement. Fig. 54 shows a wave recording with the same flow parameters as those used in Fig. 53, namely $H = 60\,\mathrm{mm}$, $V = 0.12\,\mathrm{m\,s^{-1}}$, $\omega_{wg} = 6.28\,\mathrm{rad\,s^{-1}}$. The intersections of the wave generator and the frequency give the wavenumbers of the generated and reflected waves: $k_{in} = -10.4\,\mathrm{rad\,m^{-1}}$, $k_{ref} = 7.26\,\mathrm{rad\,m^{-1}}$ with propagation velocities $c_{in} = -0.604\,\mathrm{m\,s^{-1}}$, $c_{ref} = 0.866\,\mathrm{m\,s^{-1}}$.

The propagation velocities of the measured waves can be extracted from the measurement data and should align with the theoretical prediction. The measured propagation velocities for the generated and reflected waves are $c_{in} = -0.59\,\mathrm{m\,s^{-1}}$, $c_{ref} = 0.91\,\mathrm{m\,s^{-1}}$. Treating wave reflection as a jump to another branch on the dispersion relation correctly predicts the wavenumber (and therefore velocity) of the reflected wave.

In the experimental setup, measures have been taken to reduce wave reflections. In addition, any persistent wave reflections can be identified and filtered from the data, since their wavenumbers can be determined via the discussed method. In the context of measuring converted waves (the Hawking pair k_{out}, k_{out}^{-} discussed in Section 2.4.2), any wave reflections can be easily distinguished from converted waves, since the reflections have a much lower absolute wavenumber and a much larger downstream propagation velocity than the converted waves.

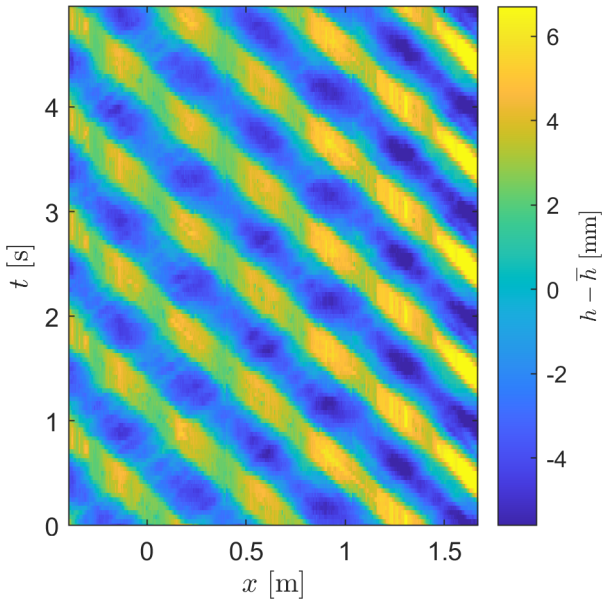

Figure 54: Water interface recording showing generated waves travelling upstream (negative x), and faint reflections travelling downstream. Experimental parameters were: $H = 60\,\mathrm{mm}$, $V = 0.12\,\mathrm{m\,s^{-1}}$, $\omega_{wg} = 6.28\,\mathrm{rad\,s^{-1}}$

4.5 Dispersion relation from background noise

As noted in the previous section, the 2D spectrum of monochromatic waves (Fig. 52) contains, outside of the strong peak corresponding to the generated wave, faint amplitudes at what looks like the dispersion curves, which is not a surprise. The flow contains random fluctuations; these can come from the pump, the water inflow, turbulence, etc., and these fluctuations can give rise to waves which lie on the dispersion relation. Therefore, a 2D spectrum of flowing water, without any generated waves, should show the dispersion curves, in a similar shape as shown in Fig. 15b. Recordings of the flowing water over a flat bottom were made. The recordings were 100 s long, with a camera sampling rate of 120 fps. Fig. 55 shows the extracted water profile of part of such a recording. Many diagonal lines, from bottom left to top right, are visible, corresponding to (small) fluctuations that travel downstream.

Fig. 56a shows the 2D spectrum of the water profile from Fig. 55. The temporal and spatial sampling rates are larger than necessary, as can be seen from the lack of signal at higher frequencies and wavenumbers. Fig. 56a shows an enlarged version of the same spectrum, plus the theoretical dispersion relation. The 2D spectrum of the background noise indeed follows the (downstream) dispersion relation. Only one branch of the dispersion relation is visible, namely the one for downstream propagating waves. The absence of the upstream dispersion branch indicates that the fluctuations present in the system originate mostly from the inflow. Also visible in Fig. 56, are additional curves at higher frequencies, possibly corresponding to waves which are not travelling purely in the along-channel ($\pm x$) direction.

Fig. 57 shows two additional 2D spectra for these no-wave flow measurements, for different background heights and flow speeds. Again, the 2D spectrum peaks exactly at the dispersion curves, still only the downstream dispersion branch is visible in the spectra. Extra curves outside of the main dispersion curves are again visible, and more numerous. Additionally, these curves only seem to exist for frequencies above some threshold, possibly dependent on the height and velocity of the flow.

The fact that random fluctuations follow the dispersion relation closely, for various flow speeds, indicates that the measuring setup and image processing methods are well-calibrated.

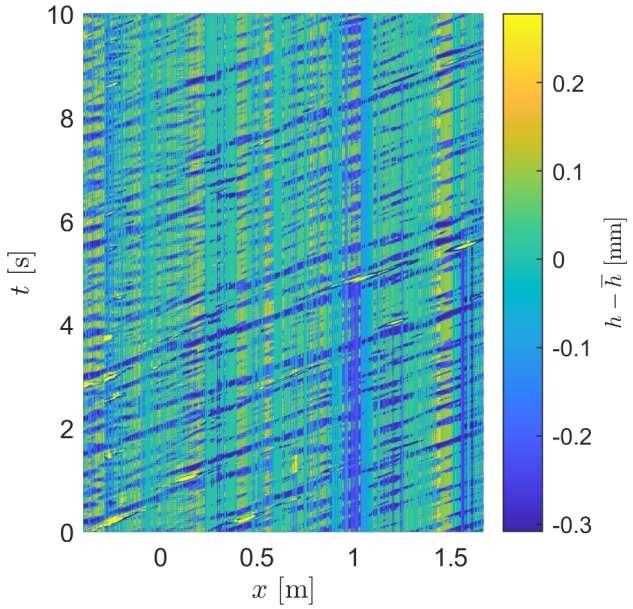

Figure 55: Steady flowing water profile recording without waves. The diagonal lines, from bottom left to top right, correspond to (small) fluctuations that travel downstream. The vertical lines throughout the figure are caused by space-dependent capillary effects, which are discussed further in Section 4.11. Experimental parameters were: $H = 73\,\mathrm{mm}$, $V = 0.16\,\mathrm{m\,s^{-1}}$

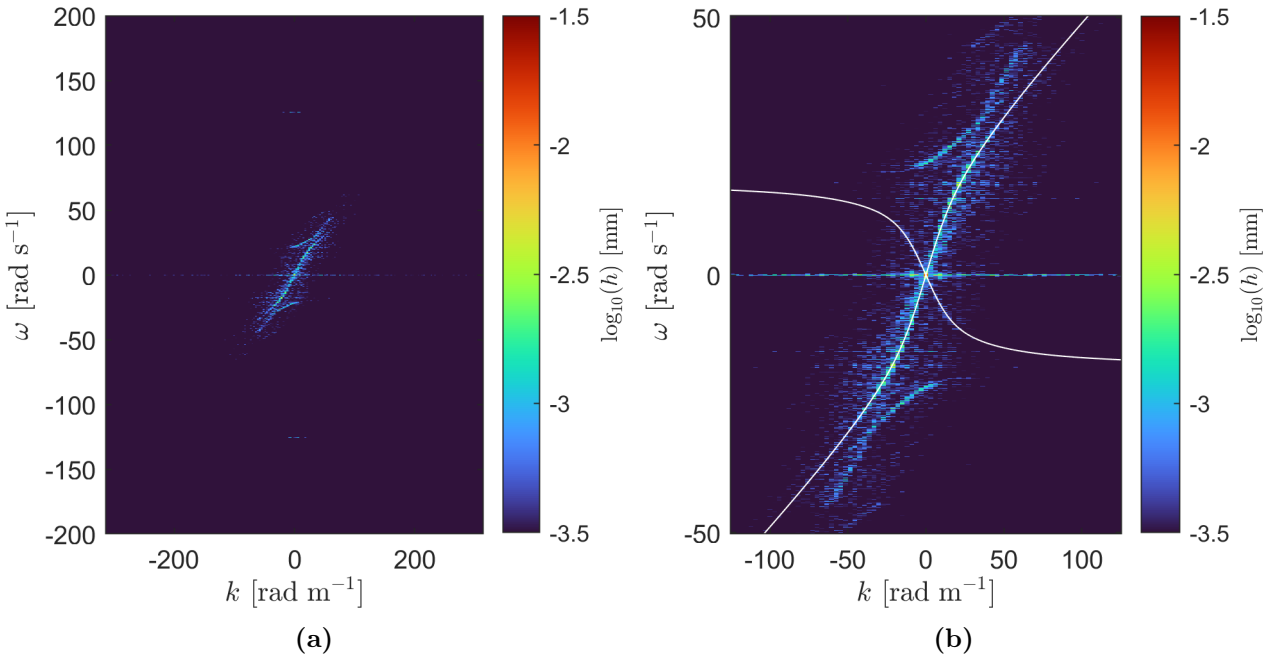

Figure 56: (a): 2D spectrum of steady flow over a flat bottom, corresponding to the measurement displayed in Fig. 55. Flow parameters: $H = 73\,\mathrm{mm}$, $V = 0.16\,\mathrm{m\,s^{-1}}$ **(b)**: Enlargement of spectrum displayed in (a), combined with the laboratory frame dispersion relation given by Eq. (61). The fluctuations present in the system lie on the dispersion relation curve, with an additional curve at larger frequencies, possibly corresponding to waves which are not travelling purely in the along-channel ($\pm x$) directions.

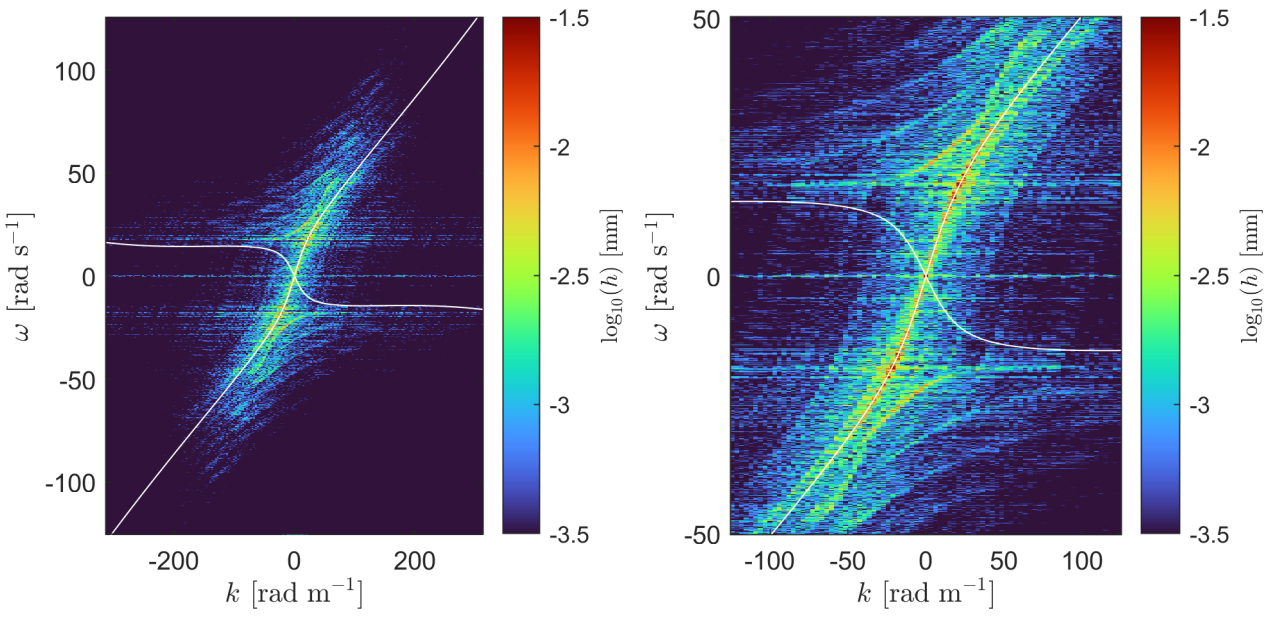

(a) $H = 67\,\mathrm{mm},\ V = 0.18\,\mathrm{m\,s^{-1}}$ **(b)** Zoom of (a)

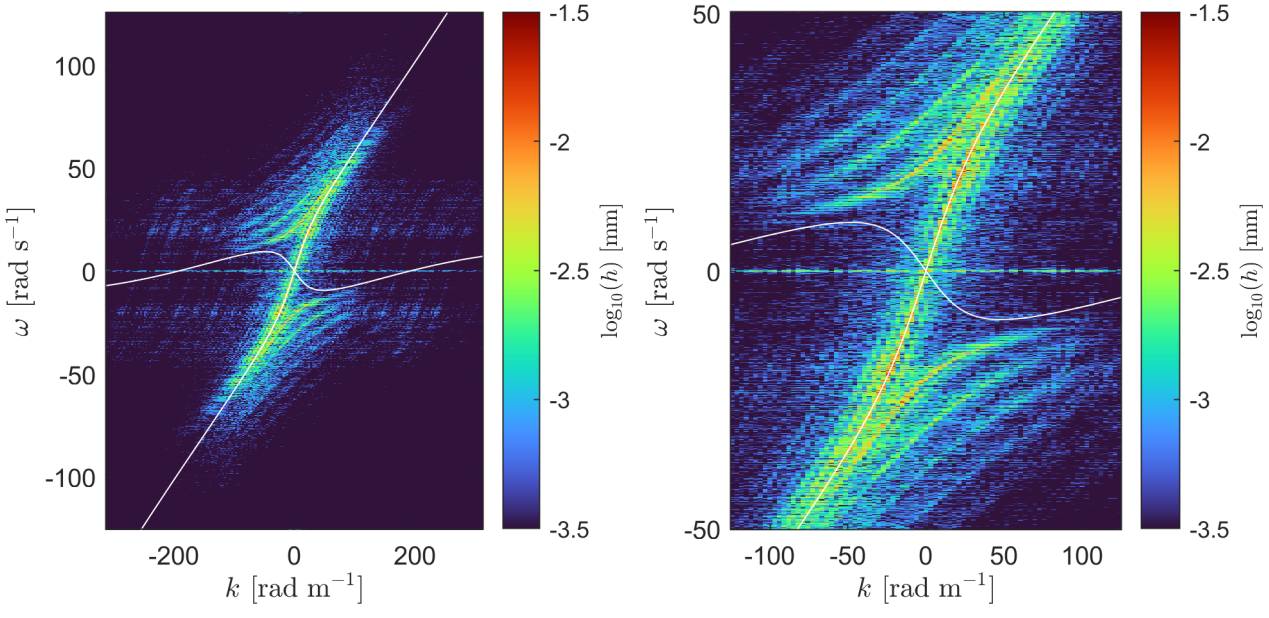

(c) $H = 47\,\mathrm{mm},\ V = 0.25\,\mathrm{m\,s^{-1}}$ **(d)** Zoom of (c)

Figure 57: 2D spectra of steady flow over a flat bottom, demonstrating that random fluctuations present in the system follow the dispersion relation given by Eq. (61). Extra curves are present outside the dispersion relation, which could correspond to waves which are not travelling purely in the along-channel ($\pm x$) direction; this effect was not researched more deeply.

4.6 Dispersion relation from air bubbles

In the previous section, it was shown that the random fluctuations present in the system follow the dispersion relation for surface gravity waves. However, most of these fluctuations seem to travel downstream as they are mostly generated at the inflow. To probe both branches of the dispersion relation, noise is added to the system using air bubbles; see Fig. 58.

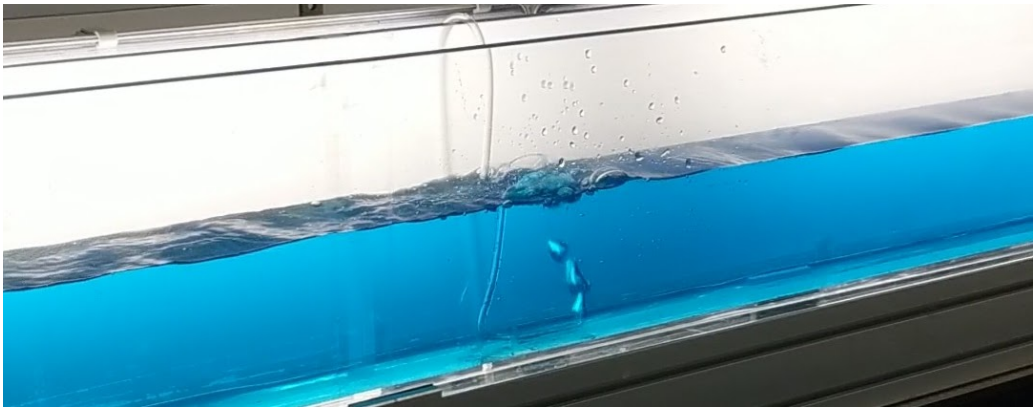

Figure 58: Air bubbles generating fluctuations. An air pump forces air through a narrow flexible tube into the wave flume. The air bubbles are released at the flume bottom, after which they rise to the surface and burst, leading to perturbations on the surface. These perturbations create waves in both streamwise directions, with the intention of probing the full dispersion relation.

An additional motivation for adding fluctuations to the system is that stimulating the system with a broadband noise source (consisting of a wide range of frequencies) could be an alternative way to produce the emission of waves at a horizon.

The water interface was recorded for 200 s at 60 frames per second. Visible in the temporal spectra, displayed in Fig. 59, the bubbles seem only to generate perturbations in a certain frequency range, and unfortunately, the lower frequency range is not generated. This is also evident from the lack of a strong signal in the region close to the origin in the 2D spectra shown in Fig. 60.

The strong peak in the temporal spectra (Fig. 59) at $\omega = 125.7\,\mathrm{rad\,s^{-1}}$ ($= 20\,\mathrm{Hz}$) is of unknown origin. The measurement was repeated without any flow and the peak was still present, ruling out the pump as the source of the anomalous frequency peak. Possibly, the air bubbles are released from the tube at exactly this frequency.

The measured 2D spectra (Fig. 60) contain the strongest Fourier amplitudes at the curves given by the dispersion relation, which was already confirmed from the previous section, but now both upstream and downstream waves are represented in the spectrum. However, the curves formed by the Fourier amplitudes in the 2D spectrum are less sharp for bubble-generated fluctuations compared to the case of background fluctuations discussed in the previous section.

The extra curves in the dispersion relation, noted in Section 4.5, are again present. Consider a single air bubble; after rising to the surface, the bubble bursts, generating a ring-shaped wave in all directions. Many waves may be present that move in cross-stream directions. The measurement method, which essentially records the shadow of the water surface, cannot distinguish wave directions in the width of the channel, this effect of projection could be responsible for the extra curves outside the dispersion relation in the 2D spectra.

In future experiments, it would be beneficial to attempt to produce the waves responsible for these

additional curves and to measure their spectra, which should then exclusively display the extra curves.

The air bubble generated fluctuations are, in the present state, not the best broadband noise source for the application of resonance finding near the horizon. As seen in Fig. 58, the bubbles are simply released from the tube and changing this tube diameter, or adding extra holes in the tube of various sizes, might generate a spectrum more akin to white noise. This was not further investigated.

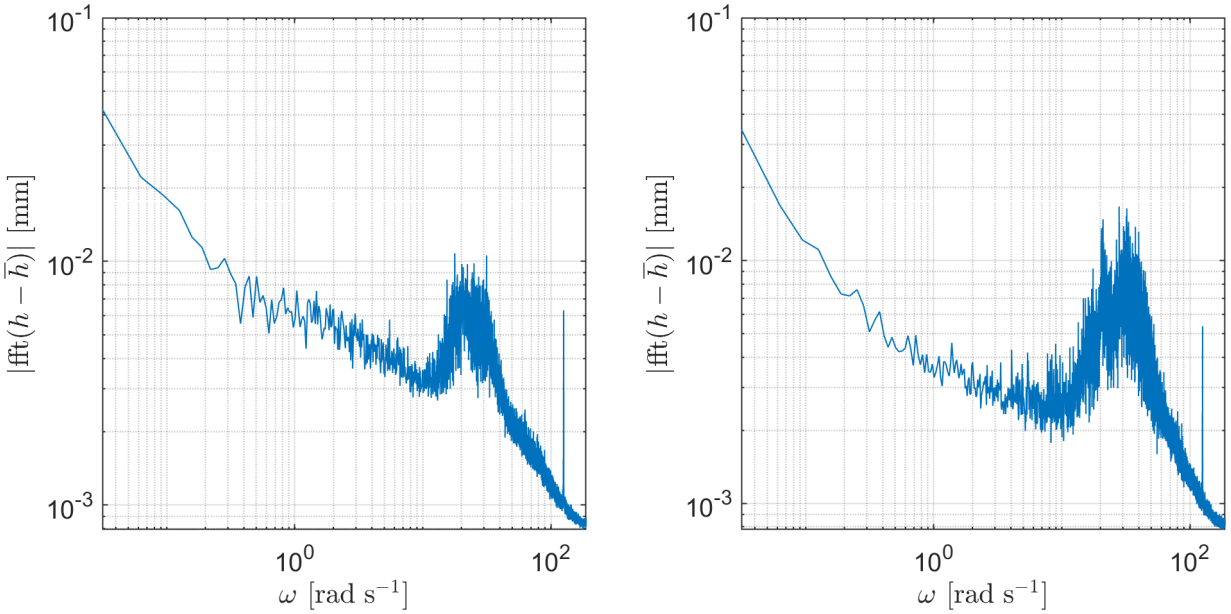

(a) $H = 119\,\mathrm{mm},\ V = 0.064\,\mathrm{m\,s^{-1}}$ **(b)** $H = 84\,\mathrm{mm},\ V = 0.090\,\mathrm{m\,s^{-1}}$

Figure 59: Temporal spectra of fluctuations generated by air bubbles. In both flow situations, the frequency distribution of fluctuations generated by the bubbles is not flat, unlike that of a white noise spectrum. Additionally, there is an anomalous peak at $\omega = 125.7\,\mathrm{rad\,s^{-1}}$ or 20 Hz, it is unclear what causes this peak.

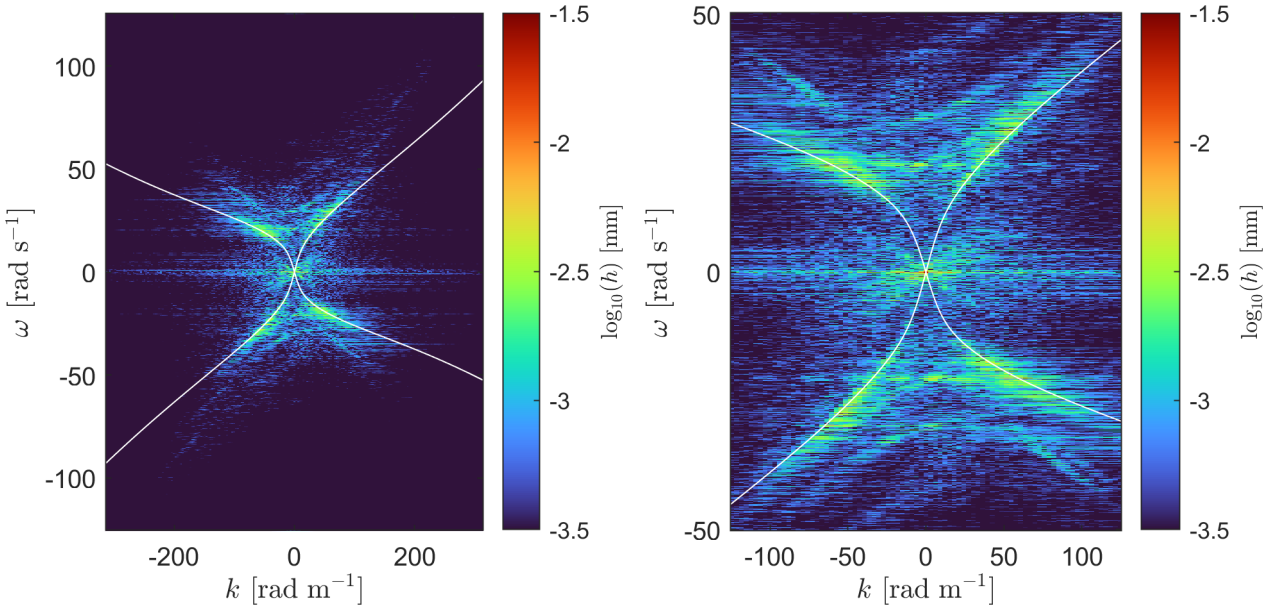

(a) $H = 119\,\mathrm{mm},\ V = 0.064\,\mathrm{m\,s^{-1}}$ **(b)** Zoom of (a)

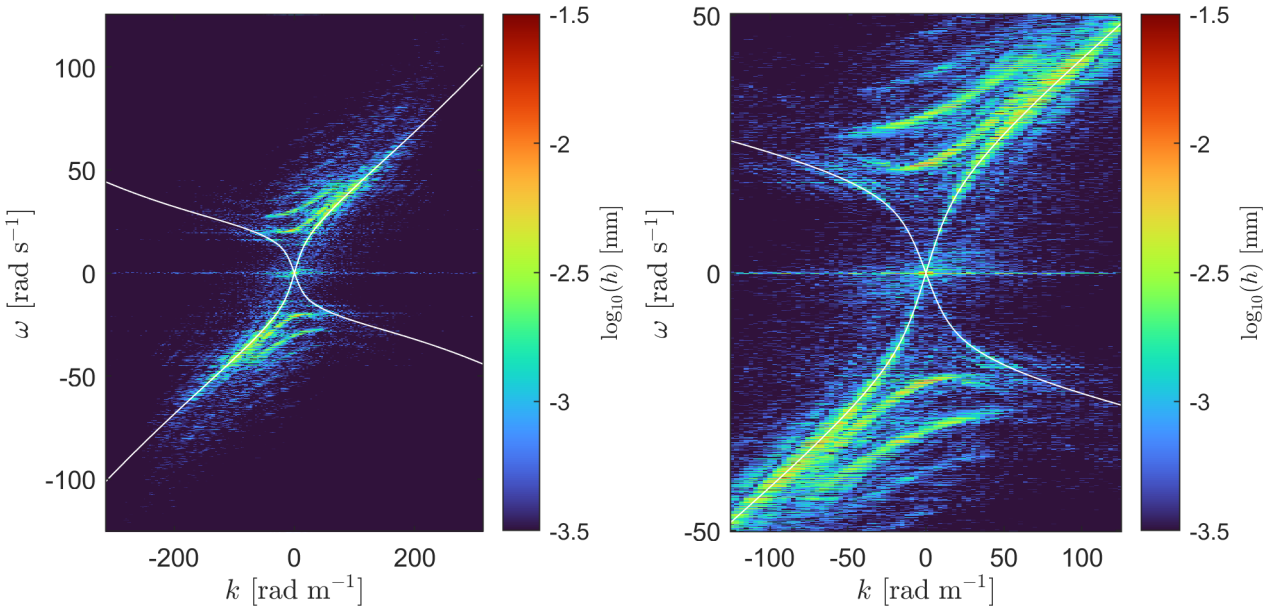

(c) $H = 84\,\mathrm{mm},\ V = 0.090\,\mathrm{m\,s^{-1}}$ **(d)** Zoom of (c)

Figure 60: 2D spectra of steady flow over a flat bottom, with the addition of air bubble generated fluctuations. The additional fluctuations lie on both the downstream and the upstream branches of the dispersion relation, Eq. (61), contrary to the background noise spectra from Fig. 57. The 2D spectra lack amplitudes at lower wavenumbers and frequencies, compared to Fig. 57. It can be seen in spectrum (c) that the increased flow speed biases the fluctuations to the downstream branch, even though the bubbles create perturbations in both flow directions. Extra curves are present outside the dispersion relation, which could correspond to waves which are not travelling purely in the along-channel, which indicates that flow in the system is not purely one-dimensional.

4.7 Steady flow over obstacle

To set up a space-dependent background flow, a linear slope is added to the bottom of the wave flume, see Fig. 61 for a diagram of the bottom profile, and Fig. 62 for a composite image of the setup that includes the obstacle.

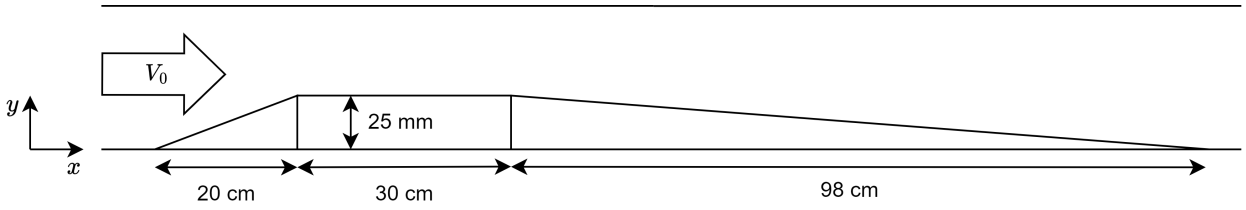

Figure 61: Schematic of the linear slope obstacle used to set up an inhomogeneous background flow. Note that the horizontal and vertical scales are different.

The linear slope was chosen since it is the simplest bottom shape without discontinuities. A discontinuity, or step, in the bottom height can lead to rotation cells and/or flow detachment. The slopes, and especially the downstream slope, are very mild, which allows for a smooth transition from high flow speed to low flow speed.

The obstacle is 3D-printed PLA. The usage of a 3D printer allows for great freedom and accuracy in the design of the obstacle, this allows the future investigation of specifically curved spacetimes.

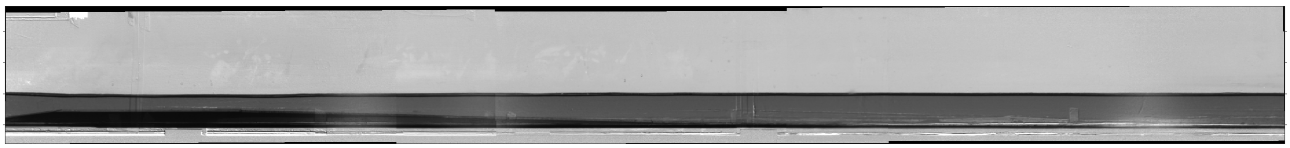

Figure 62: Composite image consisting of 3 stitches camera frames of the setup containing the linear slope. The darkest shade is the slope, the darker shade is the water and the lighter shade is the air.

The steady water surface (also referred to as the zero mode, since $\omega = 0$) is affected by submerged obstacles on the bottom of the flume. Theoretically, the shallow water equations discussed in Section 2.3.2 can predict the steady water surface for obstacles that are small with respect to the water height. The shallow water equations predict a drop in water height above an obstacle, as is visible in Fig. 8. In Fig. 62, a composite image is shown of a steady, left-to-right flow over the obstacle. It is difficult to see, but a small drop of water height for the flow region over the obstacle is indeed visible.

In Fig. 63, the extracted steady water profiles are shown for steady flow over the obstacle, for different weir heights at a constant flow rate $q = 0.0069\,\mathrm{m}^2\,\mathrm{s}^{-1}$. The reduction in the water level above the obstacle is severe for large flow speeds, which is followed by a sudden increase in water height. This behaviour is associated with the transition from a supercritical ($\mathrm{Fr} > 1$) to a subcritical ($\mathrm{Fr} < 1$) flow. With $\mathrm{Fr} = \frac{v}{\sqrt{gh}}$, the Froude number defined earlier. Fig. 64 shows an image of the supercritical to subcritical flow transition. The sudden rise in water level, known as the hydraulic jump, leads to a region of turbulence in the wake of the obstacle. The generation of turbulence is undesired and should be avoided, therefore care must be taken to create a smooth transition between supercritical and subcritical flow.

For a Froude number slightly larger than one above the obstacle, the hydraulic jump in the obstacle wake is characterised by a smooth rise in the water level, followed by a set of stationary waves. This complete structure is referred to as the undular hydraulic jump. [22] The undulations are not necessarily

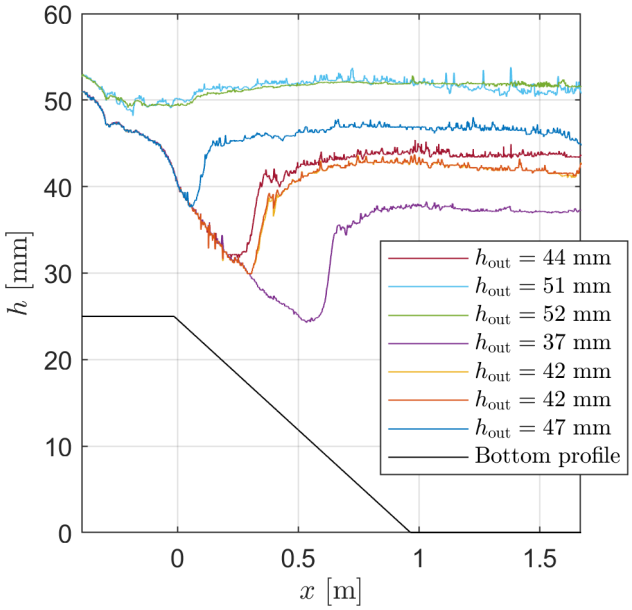

Figure 63: Time-averaged water profiles of a steady flow over the obstacle displayed in Fig. 61. The flow rate was kept constant at $q = 0.0069\,\mathrm{m}^2\,\mathrm{s}^{-1}$ and the outflow weir height was varied. The height of the water profile at the outflow is indicated. The black line shows the profile of the variable bottom. The water profiles show a transition to supercritical flow ($\mathrm{Fr} = \frac{v}{\sqrt{gh}} > 1$) and back. During the supercritical flow, the water profiles coincide, until the water transitions to subcritical flow with a hydraulic jump. The downstream distance of the critical point, where the flow transitions, varies.

uniform over the width of the channel and are therefore difficult to capture with the measurement setup, which records the water profile from the side.

The formation of the undulations is a dynamic process during which the undulations are not stationary. It is possible to place the setup in a situation where the undulations are not present, but upon sending a wave towards the obstacle, and therefore changing the instantaneous height and flow speeds over the obstacle, the undulations may start to form. This process can generate waves, which can look like the converted waves discussed in Section 2.4.2. It is unclear whether the undulation formation can act as the formation mechanism for the converted waves or whether it is a separate process and can actually be confused for, obscure, or override the wave conversion. Furthermore, if the undulations are already present, the position of these undulations can vary with changing flow conditions (for instance, by incoming waves) and can thus be perceived as propagating waves.

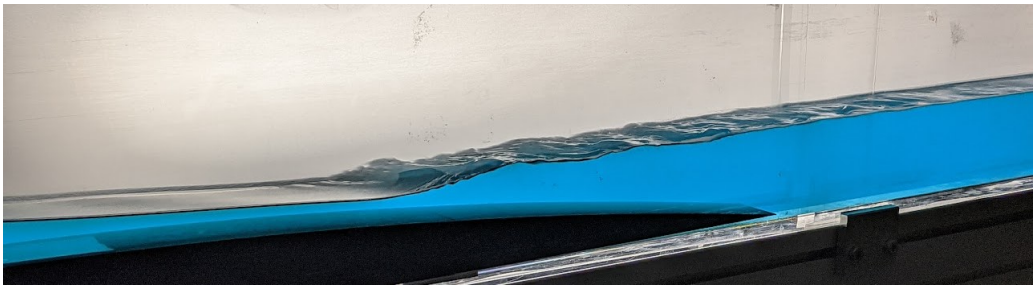

Figure 64: Supercritical (Fr>1) to subcritical (Fr<1) flow transition generating a hydraulic jump and resulting in turbulence in the obstacle wake.

Alternatively, the flow can be kept subcritical in the entire setup, avoiding the hydraulic jump effects altogether. However, this means that lower-frequency waves can no longer be used to study wave conversion since these waves will no longer be blocked by the flow over the obstacle.

4.8 Waves in a varying counterflow

Following the introduction of the obstacle (Fig. 61) to establish a spatially varying background flow (discussed in Section 4.7), waves were produced that propagated upstream to examine how they behave as they travel through this space-dependent background flow. Fig. 65 shows the evolution of the water interface.

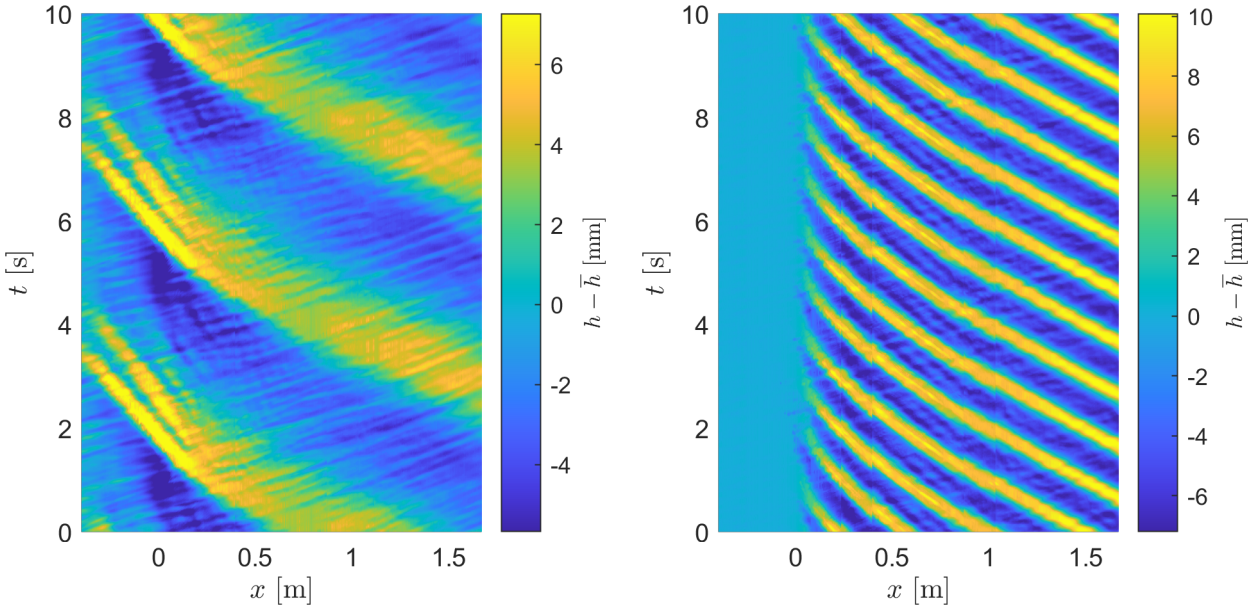

(a) $H = 63\,\mathrm{mm},\ V = 0.16\,\mathrm{m\,s^{-1}},\ \omega_{wg} = 1.6\,\mathrm{rad\,s^{-1}}$ **(b)** $H = 55\,\mathrm{mm},\ V = 0.19\,\mathrm{m\,s^{-1}},\ \omega_{wg} = 6.3\,\mathrm{rad\,s^{-1}}$

Figure 65: Extracted water profiles of upstream propagating waves on a steady background flow. The background flow is in positive x-direction, over the variable bottom introduced in Section 4.7. The upstream travelling waves encounter an increasingly strong counterflow, which slows down the waves (in the laboratory frame) and leads to curved trajectories. The wave splitting visible in (a) is discussed further in Section 4.9.2.

The lines of constant height (colour) as they move through time are lines of equal phase and are analogous to null curves. We can compare this with the typical null curves for a white hole geometry, visible in Fig. 5. In both cases, we see the steepening of the wave trajectories as the waves approach the region of increasing counterflow.

4.8.1 Numerical spacetime diagrams

As discussed in Section 2.2, the mathematical analogy is based on the idea of an effective spacetime metric. The theoretical effective spacetime diagram for a simple slope was calculated with Eq. (22), which led to the spacetime diagram shown in Fig. 5. For recordings, the expected null geodesics can be calculated from the measured background height and flow speed, and, if the analogy is accurate, these null geodesics should align with the recorded wave trajectories. To find the numerical null curves, Eq. (22) can be rewritten as

$$\frac{\mathrm{d}x}{v_B(x) - \sqrt{gh(x)}} = \mathrm{d}t\ , \tag{81}$$

where the background flow height $h(x)$ can be extracted directly from the data by time-averaging the height profiles, and the background flow velocity $v_B(x)$ can be calculated from $v_B(x) = \frac{q}{h(x)}$, where q is the flow rate, which is measured by a flow meter. Eq. (81) can be numerically integrated to obtain the null geodesics. Fig. 66 shows a wave recording including a calculated null curve. Note that Eq. (81) is derived for the case of a flat, but sloped bottom, where the curvature parameter is taken as $\eta = 1$, this is no longer correct at the beginning and starting points of the slope, or for any curved bottom profiles. Still, the calculated null curve and the trajectory of a wave propagating against the background flow visually coincide.

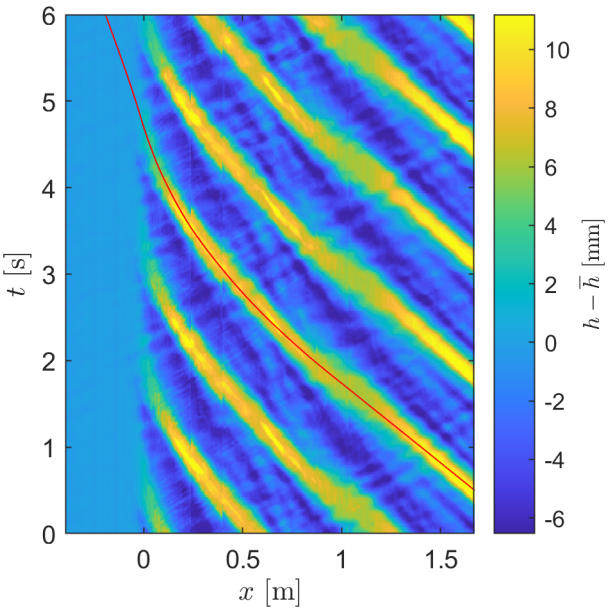

Figure 66: Extracted water profiles of waves propagating upstream on a steady background flow, including a bottom obstacle. The red curve is the predicted wave trajectory based on the effective metric, obtained by numerically integrating Eq. (81). Experimental parameters were: $H = 54\,\mathrm{mm},\ V = 0.19\,\mathrm{m\,s^{-1}},\ \omega_{wg} = 4.7\,\mathrm{rad\,s^{-1}}$.

4.9 Horizon effects

For a sufficiently large flow speed, the space-varying background flow can lead to an analogue white hole horizon. The following section investigates the behaviour of waves as they propagate towards this horizon.

4.9.1 Wave blocking

Intuitively, when the speed of the counterflow is equal to or larger than the propagation speed of the waves, the waves will be blocked. An obstacle in the tank decreases the height of the water, which influences the waves in (at least) two ways: Firstly, the decrease in water height decreases the propagation speed of the waves, as can be seen in the dispersion relation, Eq. (52). Secondly, the reduction in water height leads to a larger flow speed. Both effects decrease the propagation speed of upstream-travelling waves for an observer in the laboratory frame.

In Section 2.4.4, the theory behind wave blocking is discussed and a blocking condition, Eq. (62), is derived and plotted in Fig. 25. To measure the effect of wave frequency on blocking, waves were created at various frequencies by the wave generator and propagated upstream. The flow rate was kept constant at $q = 0.010\,\mathrm{m^2\,s^{-1}}$, and the weir height was varied until the waves were just blocked by the

obstacle. Recordings were made from which the Froude number, defined in Eq. (37), at the blocking point can be extracted. The results are plotted in Fig. 67, and compared to the theoretical prediction made in Section 2.4.4. The measurements align quite well with the theoretical prediction.

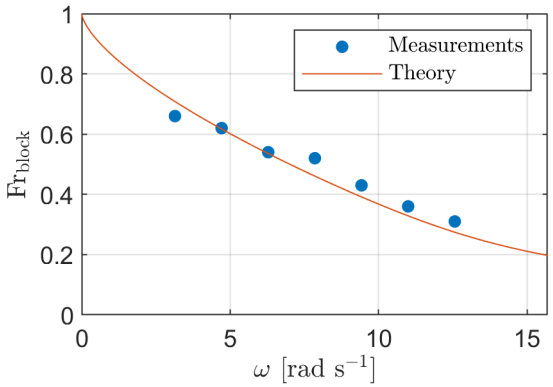

Figure 67: Froude number ($\mathrm{Fr} = \frac{v}{\sqrt{gh}}$) of the background flow at the blocking point for different wave frequencies, compared to the theoretical prediction given by Eq. (62). The flow rate was $q = 0.010\,\mathrm{m}^2\,\mathrm{s}^{-1}$

4.9.2 Wave splitting

As visible in Fig. 65a, a wave can split up into two or more waves. This wave splitting has not been observed in our setup for flows without an obstacle. A possible explanation for this behaviour is as follows: as the wave propagates towards the obstacle, and thus experiences an increasing counterflow, the absolute wavenumber increases. In other words, the wavelength of the waves decreases. However, the amplitude of the waves does not seem to decrease, as a result, the amplitude to height ratio and amplitude to wavelength ratio both increase as a wave propagates into the region of increasing counterflow, which pushes the waves into a non-linear regime, leading to undesired effects such as wave breaking, wave-wave interaction, and the observed wave splitting.

The described phenomena can be mitigated by generating smaller amplitude waves, but due to the decay of the generated waves en route to the horizon and the small amplitude of the converted waves, the reduction in generated wave amplitude makes it more challenging to resolve the waves in the setup.

4.9.3 Converted waves

In Section 2.4.2, the theory behind waves propagating against a counterflow is discussed, and it was found that, in particular flow settings, additional (large wavenumber) waves are supported in the system. However, these converted waves are not visible in the recordings (e.g. Fig. 65).

There are (at least) four ingredients needed to observe the converted waves in the laboratory:

1. The flow setup needs to be in a situation where there are three intersection points between the dispersion relation and the wave generator frequency.

2. A conversion mechanism must be present that can dynamically transform the incoming, small wavenumber wave into the large wavenumber waves. The existence of dispersion relation solutions does not mean that these waves may appear. For example, in the flow over a flat bottom, the 3 intersection points may exist, but there is no mechanism present to convert the waves.

3. The converted waves must persist. As discussed in Section 2.4.5, viscosity causes amplitude decay, which affects the lifetimes of large wavenumber waves. On top of that, turbulent effects, incoming

waves, and other influences may destroy the converted waves.

4. The recording setup must be able to resolve the converted waves. For example, if the wavenumber of the converted waves is too large, i.e., the wavelength is too short, it will be challenging to observe the waves. Shorter wavelengths lead to smaller amplitudes, which make the converted waves increasingly difficult to observe.

The obstacle at the bottom of the tank, shown in Fig. 61, was replaced by a more streamlined obstacle, with double the height, shown in Fig. 68. The obstacle was doubled in height to increase the overall scale of the experiments, in an attempt to make the ratio of capillary effects smaller. The bottom shape was chosen to minimise the hydraulic jump effects. The long downstream tail should prevent flow separation.

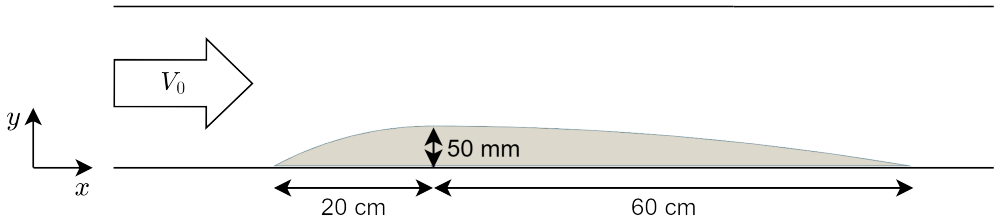

Figure 68: Streamlined obstacle schematic.

Recordings were made for incoming waves of frequencies from $1.6\,\mathrm{rad\,s^{-1}}$ to $12.6\,\mathrm{rad\,s^{-1}}$. However, the converted waves were never observed, until sending a short wave packet towards the obstacle was tried, which resulted in wave behaviour above the obstacle that could be the converted waves. Fig. 69 shows the extracted height profile of such a wave packet recording.

The wave train travels upstream towards the obstacle, where it decelerates and the wavenumber rises. A portion of the incoming wave continues upstream, while another part appears to form a wave group that moves downstream, with the individual waves still travelling upstream at a much higher wavenumber, these waves might be the transformed waves. However, when a solitary wave accompanied by a tail of higher wavenumber waves approaches the obstacle, the waves with increasing wavenumber have slightly slower propagation speeds and are thus blocked further downstream from the obstacle. This might be mistakenly interpreted as a wave packet moving backwards. The converted waves should originate from the horizon, not from the wave generator.

A problem that occurred was that these converted wave candidates were of small amplitude and that the waves were not uniform across the width of the flume. The water-wall interactions, discussed further in Section 4.11, obscured some of the waves. In an attempt to record these candidate waves, another camera was used, which looked at the setup from another angle to get around the water-wall effects. This camera is, of course, not calibrated, so the length and velocity estimates will be very rough. Fig. 70 shows stills from a movie containing converted wave candidates.

From the video, a rough estimate of the flow characteristics is made: $\omega_{wg} = 8\,\mathrm{rad\,s^{-1}}$. The flow rate was $q = 0.010\,\mathrm{m^2\,s^{-1}}$. The height above the obstacle is approximately 4 cm. For the given flow rate, water height and wave frequency, the expected wavenumber of the converted waves can be calculated from Eq. (61), which gives $k_{out} = 100\,\mathrm{rad\,m^{-1}}$ and $k_{out}^{-} = 430\,\mathrm{rad\,m^{-1}}$. The expected group velocity can be calculated from $c_g = \frac{\omega}{k}$, where the frequency is given by Eq. (61), which predicts $c_g = 0.06\,\mathrm{m\,s^{-1}}$.

The wave packet moving downstream in the video has an approximate wavenumber $k_{out} = 150\,\mathrm{rad\,m^{-1}}$ and is moving downstream with $c_g = 0.1\,\mathrm{m\,s^{-1}}$. These measurements are very imprecise, but they at least show that the wave properties of the converted wave candidates are approximately what would be

expected from the theory. Obviously, a more accurate measurement of the converted wave candidates is needed to draw any proper conclusions.

The potential observation of these waves in wave packet form raises the question: why were the converted waves not created by periodic incoming waves? Possibly, the incoming waves continually destroy any converted waves. This must be a nonlinear effect, otherwise the incoming and converted waves would simply exist in superposition. As mentioned at the beginning of this section, a dynamic mechanism of wave conversion must be present, but the investigation into such a mechanism fell outside the time constraint of this work.

Lastly, the physical analogy was developed in the shallow water limit. This limit, however, is necessarily broken in the creation of large wavenumber waves. In Ref. [12], it is argued that the breaking of assumptions and the persistence of predicted behaviour indicates a certain robustness of the analogy and generality of the effects. Still, to properly translate the results found in an analogue gravity experiment to the original system, namely general relativity, one must keep note of the (in)validity of assumptions made along the way.

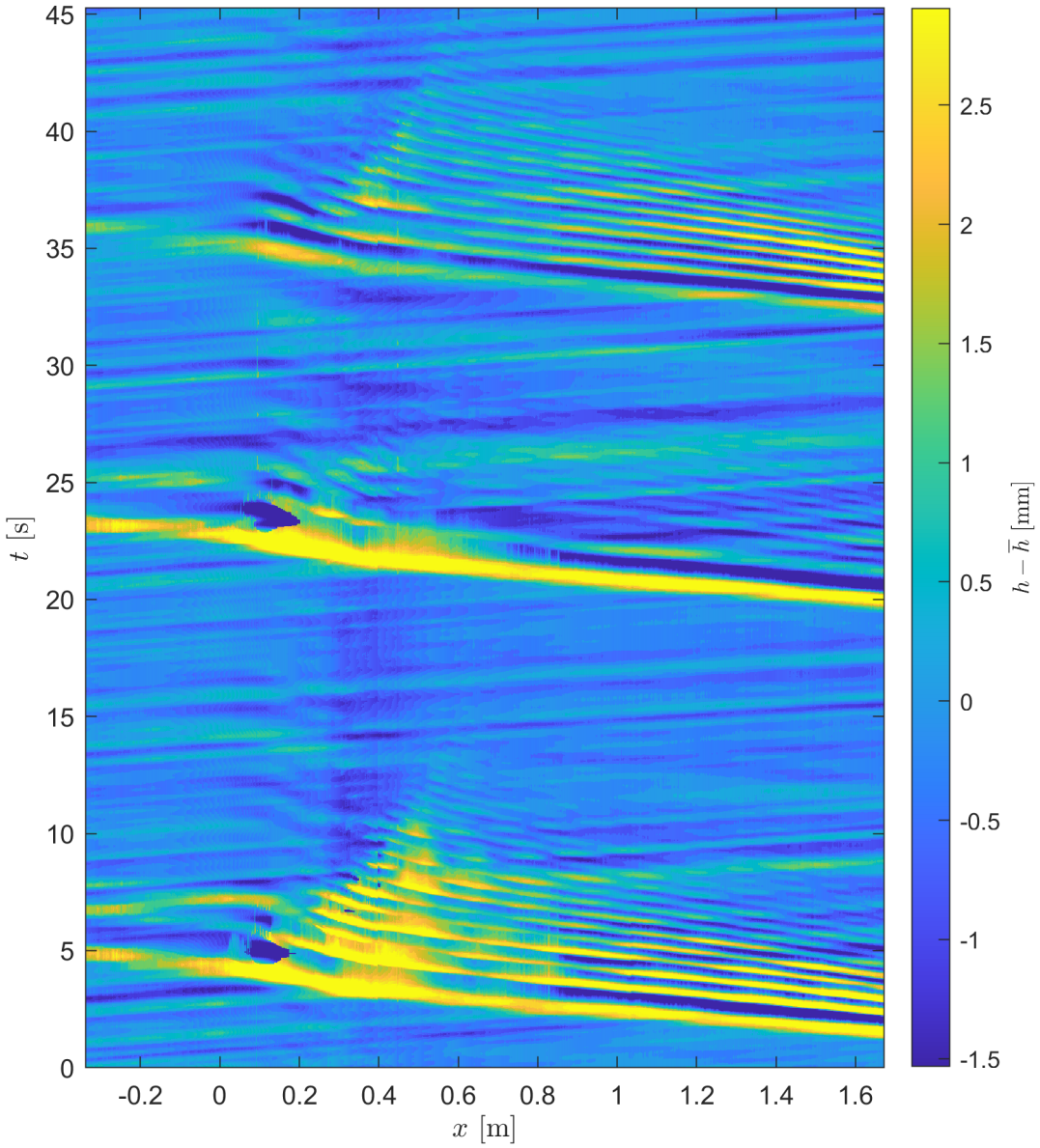

Figure 69: The wave train propagates upstream (to the left) towards the obstacle, where it is slowed down and the wavenumber increases. Part of the incident wave is not blocked and moves further upstream, but another part of the wave seems the form a wave group that moves downstream (to the right), in which the individual waves still move upstream, at significantly higher wavenumber. However, when a solitary wave with a tail of larger wavenumber waves is sent to the obstacle, the waves of increasing wavenumber have slightly lower propagation speeds and are therefore blocked further downstream from the obstacle. This could be wrongly perceived as a wave packet moving backwards. The converted waves should originate from the horizon, not from the wave generator. Experimental parameters were: $H = 88.5\,\mathrm{mm},\ V = 0.12\,\mathrm{m\,s^{-1}}$.

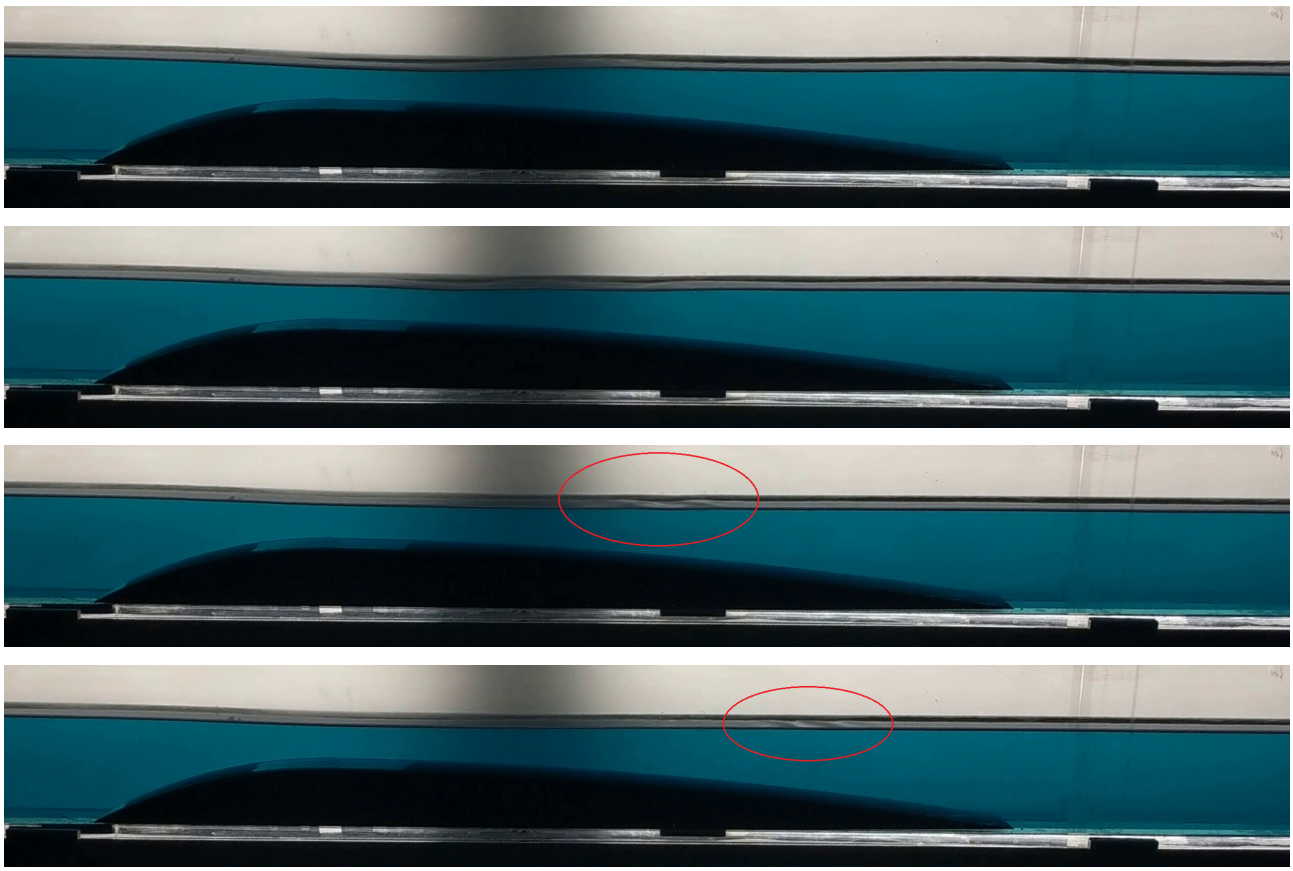

Figure 70: Movie frames from recording containing converted wave candidates. A packet of low wavenumber waves travels upstream (to the left) towards the wing-shaped obstacle, where the wavenumber of the waves in the packet is increased, and a much shorter wavepacket (encircled) is formed which can be seen travelling downstream (to the right).

4.10 Surfactant

As discussed in Section 2.4.3, the surface tension of the water and subsequent capillary effects could reduce the parameter window where extra intersections of the dispersion relation and the wave generator frequency appear. The surface tension of the medium can be reduced with the addition of a surfactant. Surfactants are a group of molecules that distribute themselves at the interfacial surface, where the mutual attractions between water molecules become interrupted.

The surfactant Triton X-45 was added to the water in the wave flume, at 0.01 wt%. This is a non-ionic surfactant which, according to the supplier, disperses well in water and leads to minimal foaming. However, problems with foam still appeared. Foam, created by air entrapment, appeared where the water flows from the wave flume into the pumping reservoir. The pump sucks water from the bottom of the reservoir, while the foam sits at the surface. However, the waterfall leads to strong stirring in the entire reservoir and foam can find its way to the pump, and to the rest of the setup. In the pump, through cavitation, foam might be generated as well. Where the water enters the wave flume, referred to as the inflow, some turbulence is present, and foam is generated as well. The foam collects on the sides of the wave flume and obfuscates the air-water interface. In the end, no measurements were possible with the surfactant in the setup due to the formation of foam.

4.11 Water-sidewall interaction

In the recorded frames, a dark line is often present at the top of the water layer; see Figs. 43 and 71. This dark line is caused by the capillary rise of the water near the flume sidewalls. The (static) capillary rise height for water on clean glass is approximately 4 mm. [13] We can compare this with the darker line of a recorded frame, which is measured to be 4 mm, for stationary and steady-flowing water. When waves are present in the system, the thickness of the dark line is no longer constant, as can be seen in Fig. 71. The dark line resulting from the water's capillary rise at the flume sidewall disappears at the wave peaks, suggesting that the dynamic interactions between the water and wall are significant and warrant further investigation.

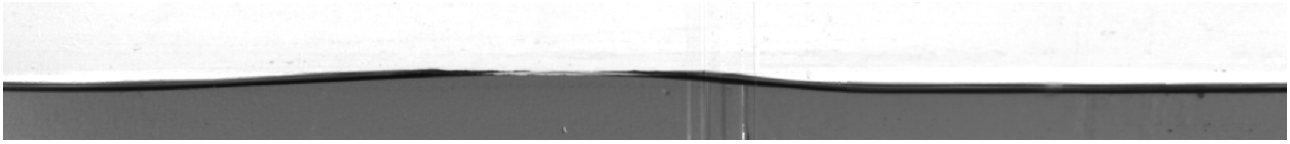

Figure 71: Part of a recorded frame of a propagating wave. The dark line, caused by the capillary rise of the water at the flume sidewall, is absent at the wave peaks, indicating that the dynamic behaviour of the water-wall interaction plays a role, which should be looked into in more detail.

The interface extraction method records the backlit water from the side, where essentially the shadow of the water is recorded. If the water profile is not uniform over the width of the channel, effectively the maximum height is measured. Therefore, if the height of the capillary rise is larger than the amplitude of propagating waves, they will be obscured. See Fig. 72 for an illustration of this effect.

Inhomogeneities in the sidewall surface, such as residues, minerals, and dust, could lead to space-dependent wetting and de-wetting properties, potentially causing persistent artefacts in the obtained water profiles. If the capillary rise remains constant throughout the system, and effectively adds a constant value to the 'true' water level, this would not be difficult to correct for. However, it might be important to consider the wetting and de-wetting dynamics of the sidewalls. Does the behaviour of the water interface differ when it ascends compared to when it descends? Do capillary forces induce a kind of hysteresis in the water profile? Additionally, could there be pinning effects that diminish the

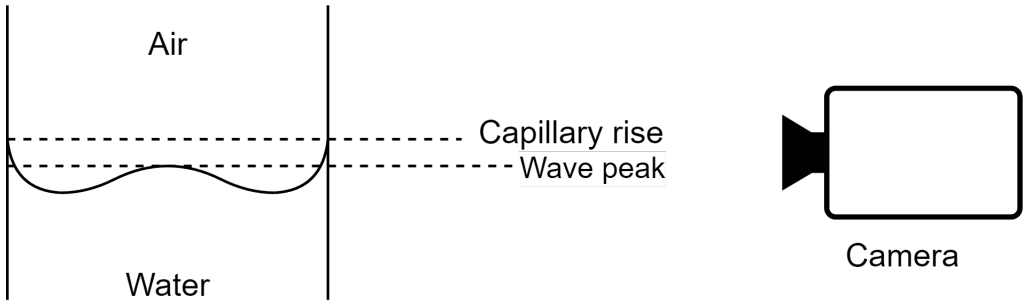

Figure 72: Schematic channel cross-section showing how capillary rise of the water near the channel sidewalls can obscure waves that are mostly located near the centre of the channel, with amplitudes lower than the capillary rise.

mobility of the water interface along the walls? These questions should be answered to understand the effect of the water-sidewall interaction on the recorded water profiles.

Another effect of the sidewalls is the formation of flow vortices near the walls, which grow in size and then detach into the domain. This vortex generation is caused by the stickiness of the wall and the resulting shear in the transverse direction. Related to this is the observation of transverse, diagonal waves in the system; see Fig. 73 for an image of these diagonal waves, forming wave patterns which resemble fish scales. These 'fish-scale' wave patterns could contribute to the Fourier amplitudes outside the dispersion curves in the 2D spectra (Figs. 56, 57 and 60).

Figure 73: Diagonal waves forming a 'fish-scale' wave pattern, possibly contributing to the curves in the 2D Fourier transforms (Figs. 56, 57 and 60) outside of the dispersion relation curves.

The relative region of influence at the sidewall, be it through interface effects or flow boundary layers, can be reduced by increasing the width of the wave flume. However, flow rates and length scales will increase, so additional flow conditioning challenges may arise. Alternatively, a measurement method that records the water surface from above might offer a solution, such as the synthetic free-surface Schlieren method. [23]

5 Conclusions

The goal of this work was to construct a laboratory setup in which surface gravity waves in flowing water act as a physical analogy to scalar field propagation in curved spacetime. The theory behind the physical analogy is discussed, and it is outlined how one may obtain an effective spacetime metric for surface gravity waves as if they are scalar fields propagating through curved spacetime.

An experimental setup is created, in which surface waves propagate upstream in an open-channel flow with space-varying water height and flow speed due to a submerged obstacle on the flume bottom. The setup includes precise control of wave generation by a vertically oscillating plunger, background water heights by a sliding weir, and flow rate by a variable pump. The water entering the setup is passed through a flow conditioner to reduce fluctuations, eddies, and inhomogeneities in the flow profile. An optical measurement setup consisting of three cameras record the water interface at a high sampling rate in space and time. A transformation from pixel coordinates in a recorded frame to real-world coordinates in the laboratory is established. The setup is designed with versatility in mind, such that future experiments can be carried out with minimal changes to the setup.

The behaviour of plunger-type wave generation is investigated, and it is found that the amplitude of the generated waves depends on many factors, and that the impact of wave generation on the mean water height in the system is important, especially when low-frequency, large-amplitude waves are desired. The interdependence of wave generation and background flow makes it challenging to perform a measurement series in which only one wave or flow parameter is varied. Furthermore, every time any wave or flow parameters are changed, the system must be given ample time to re-equilibrate.

To test the accuracy of the measurement setup and processing methods, as well as to confirm the correctness of the theoretical background, theoretical predictions are compared with the measurement results. First, the fluid mechanics of open channel flow over a flat bottom is discussed, and the theoretical prediction, namely that of a small drop in water level, is confirmed by measurements. Furthermore, the friction coefficient is found to be constant for different water heights and flow speeds.

The wavenumbers obtained from both sinusoidal fitting and the spatial spectrum of the wave profiles, for different wave generator frequencies, align with the theoretically predicted dispersion relation from linear wave theory, as do the measured phase velocities. The spectra of steady flows under different flow parameters have been measured (without waves), and the Fourier amplitudes in the 2D spectra follow the theoretical dispersion relation closely.

The behaviour of the background flow with the addition of bottom obstacles is measured. In the wake of the obstacle, a hydraulic jump can lead to turbulence, or, for milder flow transitions, stationary waves are formed, referred to as the undular hydraulic jump.

The interaction of upstream propagating waves and the background flow resulting from the submerged obstacle was studied. Both the increasing counterflow and decreasing water height over the obstacle reduce the propagation speed of the waves and eventually block the waves. The exact blocking point for different wave frequencies is predicted and measured. The white hole horizon acts as a low-pass filter: wave frequencies lower than the cut-off frequency are transmitted, and wave frequencies higher than the cut-off frequency are blocked, creating an analogue white hole. In addition, wave splitting can be observed after a wave passes the region above the obstacle, hinting at the presence of non-linear effects.

The theoretical behaviour of surface gravity waves in flowing water is discussed, and it is shown that, for some specific situations, three different wavenumber waves may exist for a given (laboratory frame) frequency. A low wavenumber wave, which is created by the wave generator, propagates towards the white hole horizon and can be converted to two large wavenumber waves, labelled as the converted

waves, one with the opposite sign wavenumber to the incoming wave. This process is analogous to the time-reverse Hawking radiation.

The converted waves are observed, but only in the case of sending wave packets to the horizon, instead of continuous periodic waves. The amplitude of the converted waves is small, and increasing the amplitude of the incoming waves is counterproductive. The capillary rise of the water at the sidewalls obscures these small amplitude waves, so a recording is made under an angle. With a different interface measurement technique that can measure the height at the centre of the channel, it should be possible to record these converted waves.

There are two other mechanisms identified which could be wrongly perceived as converted waves: the undulations in the wake of a hydraulic jump, which move around as a wave passes by, and the tail of a wave packet, which is blocked at different locations downstream of the white hole horizon.

6 Outlook

Analogue gravity is a relatively young and fascinating research field, with many topics still open, both in theory and in experiments. Since the start of the project, a research group has been formed that has grown exponentially. Joining forces with researchers and students from the Department of Mathematics and Computer Science allows us to dig deeper into the underlying mathematics of the analogy, to scrutinise its validity, and to extend the analogy where necessary.

6.1 Setup improvements

In this section, some suggestions are given to improve the created laboratory setup.

To reduce the turbulence that is generated at the wave flume inflow, a flow conditioner consisting of stacked plates is placed in the channel. As noted in Section 3.2, a flow conditioner with a larger number of channels could be installed, to further reduce the fluctuations originating from the inflow. Another common method to reduce swirls and flow profile inhomogeneities is the use of a convergent chamber. The width reduction accelerates the flow, stretching any remaining small-scale vortices. The increased rotational speed as a result of angular momentum conservation enhances the viscous dissipation of the vortices. [24]

To circumvent the effects of surface tension on the dispersion relation, a surfactant was added to the setup. As discussed in Section 4.10, the addition of surfactant led to the formation of foam in the setup, causing problems with the extraction of the water profile. In the future, other types of surfactants can be tried, or more measures against foam formation should be added to the setup.

A deeper look should be taken at wave generation. More particularly, the exact shape of the plunger and the resulting shape of the generated waves. Furthermore, in Section 4.2 it is noted that the wave generator and the background flow are interrelated. It would be good to develop some predictions for the equilibrium water level of the setup, given the flow rate, weir height, wave generator frequency, and stroke length. Alternatively, a diagnostic measurement system can be installed, which gives a real-time measurement of the water height. Currently, the water height is obtained from the processed camera recordings, which cannot be done in real-time.

Waves propagating through the flume may reflect off its end. A sponge slope was placed to reduce wave reflections, but a more sophisticated wave absorber can be considered.

The interaction of water with the flume sidewalls, discussed in Section 4.11, leads to capillary rise and shear. A wall coating, which changes the adhesive properties of the sidewalls, could lead to a more desirable behaviour of the water-wall interface. An option to reduce the relative influence of the sidewalls is to increase the width of the wave flume. However, this will lead to increased flow rates and length scales, presenting further challenges in flow conditioning. As an alternative, employing a measurement technique that captures the water surface from above, such as the synthetic free-surface Schlieren method, might provide a solution. [23] Additionally, extracting the height profile of the water from above will give us insight into the 2D behaviour of the waves in the wave flume.

Incorporating flow visualisation methods like Particle Image Velocimetry would enable us to examine the flow patterns around the submerged obstacle, assess the level of turbulence of the flow, verify the irrotationality of the flow, and investigate the interaction between the flow and the oscillating plunger.

6.2 Further research

An obvious follow-up of this research will be to measure the wavenumbers and the amplitudes of the converted waves that appear at the white hole horizon. An extension of the white hole horizon experiments could be the addition of locally generated fluctuations as an energy source, mentioned in

Section 4.6. How does the addition of noise (from air bubbles) influence the horizon effects? Can the added noise lead to an amplification of wave conversion?

Apart from that, one can consider effective spacetime metrics with time-dependent components. In the analogy, such a dynamical metric could correspond to black/white hole formation. Furthermore, the mathematical analogy between scalar waves and shallow water waves gives a kinematic description of wave propagation, i.e., the waves are influenced by the background flow, but not vice versa. In the setup, it is quite straightforward to create waves that influence the metric (such as large amplitude waves). The dynamic modification of the metric feeds back on the propagating waves, creating a coupling between the waves and the effective metric. This is referred to as backreaction, which is an exciting research avenue.

The extra curves visible in the 2D spectra, which could correspond to waves that are not travelling purely in along-channel directions, should be investigated further. Is it, for instance, possible to make a theoretical prediction based on the width of the channel? Furthermore, can the setup be adjusted such that these transverse waves disappear, so the setup behaves more (1+1) dimensional?

As mentioned repeatedly, the created experimental setup is intended to serve as a versatile platform for conducting wave experiments. The setup has already been used in the study of solitary wave (soliton) propagation, described by the Korteweg-De Vries equations. More specifically, the propagation of these solitons over variable bottoms and soliton-soliton scattering.

Another possible research avenue entirely is the study of analogue Casimir or other resonant cavity effects by installing (oscillating) meshes that partially reflect waves.

Finally, it would be great to add another horizontal dimension to the setup, which would allow us to study the effect of a rotating spacetime, like that described by the Kerr spacetime. An effect that has been measured in the physical analogy is superrotation, a process in which waves incident on a rotating black hole can extract energy from it. [25, 26] In the design of such a setup, it would be wise to create a digital twin to the setup, such that, through computational fluid dynamics, a better understanding can be obtained beforehand about how the flow in the setup will behave.

Acknowledgements

I would like to thank Federico for the many insightful and pleasant discussions. His constant stream of ideas will keep any project exciting and moving forward. I would like to thank Matias and Ziqi for their advice on experimental methods. Of course, the experimental setup could not have been constructed without the support of the technicians from the Fluids and Flows group, Gerald and Jørgen.

Lastly, I wish the TU/e analogue gravity group the best of luck with the continuation of the project.

References

[1] S. W. HAWKING. "Black hole explosions?" In: *Nature* 248.5443 (Mar. 1974), pp. 30–31. ISSN: 0028-0836. DOI: 10.1038/248030a0. URL: https://www.nature.com/articles/248030a0.

[2] W. G. Unruh. "Experimental Black-Hole Evaporation?" In: *Physical Review Letters* 46.21 (May 1981), pp. 1351–1353. ISSN: 0031-9007. DOI: 10.1103/PhysRevLett.46.1351. URL: https://link.aps.org/doi/10.1103/PhysRevLett.46.1351.

[3] Ralf Schützhold and William G. Unruh. "Gravity wave analogs of black holes". In: *Physical Review D* 66.4 (May 2002), p. 044019. DOI: 10.1103/PhysRevD.66.044019. URL: http://arxiv.org/abs/gr-qc/0205099%20http://dx.doi.org/10.1103/PhysRevD.66.044019.

[4] Silke Weinfurtner et al. "Measurement of stimulated hawking emission in an analogue system". In: *Physical Review Letters* 106.2 (2011). ISSN: 00319007. DOI: 10.1103/PhysRevLett.106.021302.

[5] S W Hawking. *Particle Creation by Black Holes*. Tech. rep. 1975, pp. 199–220.

[6] Adam D Helfer. "Do black holes radiate?" In: *Reports on Progress in Physics* 66.6 (June 2003), pp. 943–1008. ISSN: 0034-4885. DOI: 10.1088/0034-4885/66/6/202. URL: https://iopscience.iop.org/article/10.1088/0034-4885/66/6/202.

[7] W. G. Unruh. "Has Hawking Radiation Been Measured?" In: *Foundations of Physics* 44.5 (May 2014), pp. 532–545. ISSN: 0015-9018. DOI: 10.1007/s10701-014-9778-0. URL: http://link.springer.com/10.1007/s10701-014-9778-0.

[8] Germain Rousseaux et al. "Observation of negative-frequency waves in a water tank: A classical analogue to the Hawking effect?" In: (Nov. 2007). DOI: 10.1088/1367-2630/10/5/053015. URL: http://arxiv.org/abs/0711.4767%20http://dx.doi.org/10.1088/1367-2630/10/5/053015.

[9] Benoit Cushman-Roisin. "ENVIRONMENTAL FLUID MECHANICS". In: (2022).

[10] M J Lighthill. "Waves in fluids". In: (1978), p. 504.

[11] Kraaiennest. *CC BY-SA 3.0*. URL: https://commons.wikimedia.org/w/index.php?curid=4612291.

[12] Silke Weinfurtner et al. "Classical Aspects of Hawking Radiation Verified in Analogue Gravity Experiment". In: *Lecture Notes in Physics*. Vol. 870. 2013, pp. 167–180. DOI: 10.1007/978-3-319-00266-8{_}8. URL: https://link.springer.com/10.1007/978-3-319-00266-8_8.

[13] Pierre-Gilles de Gennes, Françoise Brochard-Wyart, and David Quéré. *Capillarity and Wetting Phenomena*. New York, NY: Springer New York, 2004. ISBN: 978-1-4419-1833-8. DOI: 10.1007/978-0-387-21656-0. URL: http://link.springer.com/10.1007/978-0-387-21656-0.

[14] L M Milne-Thomson. *Theoretical Hydrodynamics*. 4th. London: MACMILLAN & CO LTD, 1962.

[15] Bruce Roy Munson, Donald F. Young, and T. H. (Theodore Hisao) Okiishi. *Fundamentals of fluid mechanics*. J. Wiley, 1998. ISBN: 9780471355021.

[16] Ronald L Panton. *Incompressible Flow*. Wiley, June 2013. ISBN: 9781118013434. DOI: 10.1002/9781118713075. URL: https://onlinelibrary.wiley.com/doi/book/10.1002/9781118713075.

[17] Stephanie Lowell and Rishad A. Irani. "Sensitivity analysis of plunger-type wavemakers with water current". In: *2020 Global Oceans 2020: Singapore - U.S. Gulf Coast* (Oct. 2020). DOI: 10.1109/IEEECONF38699.2020.9389447.

[18] Stephanie Lowell, Johanna McPhee, and Rishad A. Irani. "Plunger-type wavemakers with flow: Sensitivity analysis and experimental validation". In: *Applied Ocean Research* 121 (Apr. 2022), p. 103065. ISSN: 01411187. DOI: 10.1016/j.apor.2022.103065. URL: https://linkinghub.elsevier.com/retrieve/pii/S0141118722000207.

[19] Peter Sturm. "Pinhole Camera Model". In: *Computer Vision*. Boston, MA: Springer US, 2014, pp. 610–613. DOI: 10.1007/978-0-387-31439-6{_}472.

[20] Zhengyou Zhang. "A flexible new technique for camera calibration". In: *IEEE Transactions on Pattern Analysis and Machine Intelligence* 22.11 (June 2000), pp. 1330–1334. ISSN: 01628828. DOI: 10.1109/34.888718.

[21] J.-Y. Bouguet. "Camera Calibration Toolbox for Matlab". In: *CaltechDATA* (2022). DOI: 10.22002/D1.20164. URL: https://data.caltech.edu/records/jx9cx-fdh55.

[22] Hubert Chanson. "Current knowledge in hydraulic jumps and related phenomena. A survey of experimental results". In: *European Journal of Mechanics - B/Fluids* 28.2 (Mar. 2009), pp. 191–210. ISSN: 09977546. DOI: 10.1016/j.euromechflu.2008.06.004. URL: https://linkinghub.elsevier.com/retrieve/pii/S0997754608000678.

[23] Frédéric Moisy, Marc Rabaud, and Kévin Salsac. "A synthetic Schlieren method for the measurement of the topography of a liquid interface". In: *Experiments in Fluids* 46.6 (June 2009), pp. 1021–1036. ISSN: 07234864. DOI: 10.1007/s00348-008-0608-z.

[24] Azar Eslam Panah and Amir Barakati. "Design and build a water channel for a fluid dynamics lab". In: *ASEE Annual Conference and Exposition, Conference Proceedings* 2017-June (June 2017). URL: https://pure.psu.edu/en/publications/design-and-build-a-water-channel-for-a-fluid-dynamics-lab.

[25] Theo Torres et al. "Rotational superradiant scattering in a vortex flow". In: *Nature Physics* 13.9 (Sept. 2017), pp. 833–836. ISSN: 1745-2473. DOI: 10.1038/nphys4151. URL: https://www.nature.com/articles/nphys4151.

[26] Theo Torres. "Hydrodynamic simulations of rotating black holes". In: (Nov. 2021). URL: http://arxiv.org/abs/2111.02282.